2016

Experimental Investigation of Nonlinear Eects in Multi-mode Optical Fibers

Mina Esmaeelpour
Lehigh University

Experimental Investigation of Nonlinear Effects in Multi-mode Optical Fibers

by

Mina Esmaeelpour

A Dissertation
Presented to the Graduate Committee
of Lehigh University
in Candidacy for the Degree of
Doctor of Philosophy
in
Department of Physics

Lehigh University
May 2016

Approved and recommended for acceptance as a dissertation in partial fulfillment of the requirements for the degree of Doctor of Philosophy.

Mina Esmaeelpour
Experimental Investigation of Nonlinear Effects in Multi-mode Optical Fibers

Date

Jean Toulouse, Dissertation Director, Chair

Accepted Date

Committee Members

Ivan Biaggio

Volkmar Dierolf

Sushil Kumar

Slava Rotkin

Roland Ryf

For my beloved mother.

Acknowledgement

I thank my advisor, professor Jean Toulouse, for his consideration and acceptance in his research group and for his constant support and training not only for me to be a better scientist but also a better person. His constant and honest feedback on my work has made my scientific and personal advancement possible. I would like to acknowledge Dr. Roland Ryf and Dr. René-Jean Essiambre from Bell Labs in Holmdel, NJ. I thank Dr. Ryf for accepting me as an intern in his group and training me in the lab and giving me the valuable opportunity to work at Bell Labs during my PhD. I am extremely grateful for his patience, immeasurable support and training all the time. I also gratefully acknowledge Dr. Essiambre for his guidance, support and endless training. Their mentorship, continual assistance and patience have made this thesis and my advancement possible. I deeply thank professor Ivan Biaggio for being in my committee and for his continuous support, encouragement, and motivation. I must thank professor Volkmar Dierolf for his continuous support during my PhD, for his help and encouragement all the time. I thank my committee members, professor Slava Rotkin, and professor Sushil Kumar for their time, guidance and support. I thank Dr. Nicolas Fontaine, for his continuous training in the lab and his help beyond the lab. I thank Mihaela Dinu, Allan Gnauk, Greg Raybon, and Haoshuo Chen who helped me with my experiments at Bell Labs. Last but not least, I would like to send my deepest gratitude to my family for their continuous support and encouragement, and specially for my mother who continues to help me be a better person, encourages me to follow my dreams and gave me the gift of books as a child. I also would like to thank my high school physics teacher Mr. Farshbaf who triggered my interest in becoming a scientist.

Contents

List of Figures

List of Tables

List of Abbreviations

ASE	Amplified Spontaneous Emission
DEMUX	Demultiplexer
DGD	Differential Group Delay
DMDG	Differential Mode-Dependent Gain
ECL	External Cavity Laser
EDFA	Erbium-Doped Fiber Amplifier
FMF	Few-Mode Fiber
FWHM	Full Width at Half Maximum
FWM	Four-Wave Mixing
GPIB	General Purpose Interface Bus
IM-FWM	Intermodal Four-Wave Mixing
LG	Laguerre-Gaussian
LP	Linearly Polarized
MCF	Multi-Core Fiber
MMF	Multi-Mode Fiber
MS-PL	Mode-Selective Photonic Lantern
MUX	Multiplexer
MZM	Mach-Zehnder modulator

OSA	Optical Spectrum Analyzer
OTDR	Optical Time-Domain Reflectometer
PBS	Polarization Beam Splitter
PPG	Pulse Pattern Generator
QPSK	Quaternary-Phase-Shift Keying
SBS	Stimulated Brillouin Scattering
SDM	Space-Division Multiplexing
SE	Spectral Efficiency
SMF	Single-Mode Fiber
SPM	Slef-Phase Modulation
SRS	Stimulated Raman Scattering
VCO	Voltage-Controlled Oscillator
WDM	Wavelength-Division Multiplexing
WS	Waveshaper
WSS	Wavelength Selective Switch
XPM	Cross-Phase Modulation

Abstract

In the present work, we investigate possible solutions to the capacity limits of optical communication systems. Just as wavelength division multiplexing (WDM) has been used in the past twenty years, spatial division multiplexing (SDM) is now being explored to further increase the transmission capacity of fibers. In SDM, the spatial dimension of the fiber is the degree of freedom that is being exploited. SDM makes use of several spatial modes propagating in a single core multi-mode fiber or in a multi-core fiber in which the cores are coupled with each others. However for SDM to become a reality in transmission systems, the problem of amplification must be addressed. If the power is increased in these fibers, nonlinear effects will emerge within and between different modes of the multi-mode or multi-core fibers which can degrade the transmission performance. On the other hand, nonlinear effects such as stimulated Raman Scattering can be utilized to build optical amplifiers for multi-mode and multi-core fibers.

In this thesis, we study theoretically and experimentally the inter-modal nonlinear effects of four-wave mixing (FWM) and Raman scattering in a graded-index few-mode fiber which supports 6 spatial and polarization modes. The efficiency of the four-wave mixing processes between the fundamental and higher order modes is experimentally measured for the non-degenerate four-wave mixing configuration with two pumps and one signal. The effect of the relative polarizations of the three waves involved in the four-wave mixing process is also studied to understand the fluctuations in the idler powers generated through the nonlinear intermodal process. Finally, experiments are performed in a 70 km graded-index few-mode fiber with 3 spatial modes to understand the effect of different pumping schemes in a distributed Raman amplifier. We demonstrate experimentally that equalized gain in all three spatial modes is achieved by coupling the pump source into the higher order modes instead of the fundamental mode of a few-mode fiber. Distributed Raman amplification is then used in recirculating the signal through the fiber span and data transmission is successfully achieved over 1050 km.

Chapter 1

Introduction

1.1 Literature Review

The number of devices that connect to the internet is increasing everyday and that requires an increase in the bandwidth and capacity of optical communication systems. The capacity of optical fiber communication links is determined by the spectral efficiency of the optical fiber itself limited by nonlinear effects in fibers, the total bandwidth determined by the current gain bandwidth of the Erbium-doped fiber amplifiers (C-band: 1530-1565 nm), and the number of spatial channels in the fibers, i.e. the fiber two modes in single-mode optical fibers (one for each polarization). Therefore, to increase the amount of data that can be transmitted through fibers we must look at different solutions, all based on the three limiting factors of fiber capacity mentioned above. One solution is parallelism: more single mode fiber cables are used in parallel, but the increasing the number of fibers requires lower powers per fiber to avoid increase in cost and energy consumption. This requires silicon photonics integration along with architectural innovations such as software defined networking. Increasing the bandwidth by utilizing L-band (1568-1605 nm) Erbium-doped fiber amplifiers in addition to the C-band can also help to increase the bandwidth. Moving to 2 μm wavelength, where amplifiers with bandwidth larger than Erbium-doped fiber amplifiers exist, is also an option.

In recent years, Space-Division Multiplexing (SDM) has been proposed as another solution to overcome the Single-Mode Fiber (SMF) capacity limit imposed by a combination of Shannon's information theory and the nonlinearities in optical

fibers [6, 7]. This limit can be exceeded with SDM by making use of few-mode (FMFs), multi-mode (MMFs), or multi-core fibers (MCFs). These fibers offer significant advantages for SDM, because the spatial modes used for transmission are tightly packed and can be processed together. This is particularly advantageous for building optical components like optical amplifiers that are essential in SDM transmission systems. Raman amplification in particular is very appealing as it does not require any special active fiber since the transmission fiber is itself the distributed gain medium. Raman amplification has been extensively studied and has become an established technology in SMF systems [8, 9]. Developing cost-effective MMF devices such as inline amplifiers is a necessity for SDM to be successful. Raman amplification in MMFs has been studied to understand the gain in different modes as well as the mode evolution [10, 11]. It has also been studied theoretically in MMFs by Antonelli and colleagues [12]. In order to design a Raman amplifier in MMFs with equal gain in all modes is important and the intensity overlap integral of different modes is a crucial element to realize suitable pump configuration for a specific MMF with different refractive index profile. The conditions for gain equalization in MMFs has been studied in [13] for step index MMF and distributed Raman amplification with counter pumping has been demonstrated in [14] to reach equal amplification in all the modes of a graded-index FMF by coupling the pump in the higher order mode instead of the fundamental mode.

Kerr nonlinear effects in fibers have also been studied extensively in SMFs and MMFs [15, 16, 17, 18]. In MMFs four-wave mixing (FWM) between waves in the same mode is called Intra-modal FMF and FWM between waves in different guided modes of the fiber called Inter-modal four-wave mixing. Inter-modal four-wave mixing (IM-FWM) has been observed in FMFs as early as 1974 [19] by Stolen and colleagues in the form of partially-degenerate IM-FWM in FMFs, taking advantage of the different group velocity dispersions of various spatial modes to achieve phase-matching. Observations of various intermodal nonlinearities, including IM-FWM, have been reported in photonic crystal fibers [20, 21, 22, 23] and MMFs [24]. These observations have been made using relatively short lengths of fibers, up to a few tens of meters. However, fibers of several kilometers are required for SDM applications. Numerical investigations have been published on intermodal nonlinear

effects in very long fibers that support multiple spatial modes [25] but few experimental studies exist on this topic [5, 26, 27]. Yet, a detailed characterization of IM-FWM occurring in real communication-length FMFs remains of great interest to correctly account for nonlinear interactions and ascertain their impact on SDM systems. IM-FWM in graded-index FMFs is of particular interest because of its implications on the capacity of space-division multiplexed systems [6, 7], as well as its applications to wavelength conversion and parametric amplification. IM-FWM was recently reported for the *multiple-mode pumps configuration*, explained later in the text, in a graded-index FMF that only supported LP_{01} and LP_{11} modes [26], and the phase-matching bandwidth was also calculated numerically [28]. LP modes are the linearly polarized modes of the fibers under study: LP_{01} is the fundamental mode and LP_{11a} and LP_{11b} are the degenerate higher order modes.

In this chapter, the modes of MMFs are studied, and nonlinear effects in fibers are discussed. In particular, FWM and Raman scattering effects are studied in detail and the governing equations solved analytically.

1.2 Background

This section describes the modes in MMFs, the wave equation for the real modes of the fiber, and the wave equation solutions in the undepleted pump approximation, introducing linearly polarized modes. The different nonlinear processes in optical fibers are briefly described, including the Kerr and scattering processes such as self- and cross-phase modulation, four-wave mixing as well as the Brillouin and Raman scattering processes. Since Four-wave Mixing and Raman scattering are experimentally investigated in the next chapters, a more detailed presentation of the equations leading to these two processes are made in the following sections with particular focus on their gain efficiency.

1.2.1 Modes of MMFs

The optical fibers used in telecommunication systems are based on silica (SiO_2). These fibers have low loss in the 1550 nm wavelength range which makes them suitable for data transmission. They usually have germanium doped cores and/or pure silica cores with depressed cladding. The refractive index of these fibers can be engineered, the simplest case being step-index fibers [29]. Here, the modes of a

silica-based MMF with step-index profile will be discussed and the results extended to graded-index fibers with a few well-defined modes. The exact solution of the wave equation for MMFs yields the true modes of the fiber which are TE, TM, HE and EH modes. These modes are orthogonal to each other, non-degenerate and each travels with a different speed in the fiber. They can combine with each other due to imperfections introduced in the fiber during the fiber drawing, to generate different intensity profiles along the fiber . TE and TM stand for the transverse electric ($H_z = 0$) and transverse magnetic ($E_z = 0$), respectively while EH and HE modes are hybrid modes and have non-zero E and H field z-components. If the fiber is weakly-guiding, as a result of a very small refractive index difference between the core and cladding, these modes can be approximated by linearly-polarized,LP modes [30, 31, 32]. LP modes can be written as a linear combination of the real modes of the fiber as discussed later in this chapter. The propagation of electromagnetic waves in fibers is governed by Maxwell's equations shown below:

$$\nabla \times \overrightarrow{E}(\overrightarrow{r}, t) = \frac{\partial \overrightarrow{B}}{\partial t} \tag{1.1}$$

$$\nabla \times \overrightarrow{H} = \overrightarrow{J} + \frac{\partial \overrightarrow{D}}{\partial t} \tag{1.2}$$

$$\nabla . \overrightarrow{D} = \rho_f \tag{1.3}$$

$$\nabla . \overrightarrow{B} = 0, \tag{1.4}$$

where $\overrightarrow{E}$ and $\overrightarrow{H}$ are the electric and magnetic field vectors,$\overrightarrow{D}$ and $\overrightarrow{B}$ the electric and magnetic flux densities, and $\overrightarrow{J}$ and ρ_f the current density vector and charge density respectively [33]. The quantity $\overrightarrow{D} = \epsilon_0 \overrightarrow{E} + \overrightarrow{P}$ where ϵ_0 and $\overrightarrow{P}$ are the vacuum permittivity and induced electric polarization respectively. The quantity $\overrightarrow{P}$ can be written in the form of $\overrightarrow{P_L} + \overrightarrow{P_{NL}}$, where $\overrightarrow{P_L}$ is the linear part and $\overrightarrow{P_{NL}}$ the nonlinear part due to nonlinear effects in the fiber. In order to study the modes of optical fibers, we assume a linear regime and only the linear part of the induced polarization is therefore in the wave vector calculation:

$$\nabla^2 \overrightarrow{E} - \frac{1}{c^2} \frac{\partial^2 \overrightarrow{E}}{\partial t^2} = \mu_0 \frac{\partial^2 \overrightarrow{P_L}}{\partial t^2}. \tag{1.5}$$

From Eq. 1.5 and neglecting birefringence, we obtain the Helmholtz equation in the frequency domain also known as the wave equation (WE):

$$\nabla^2 \widetilde{E}(\overrightarrow{r},\omega) + n^2(\omega)\frac{\omega^2}{c^2}\widetilde{E}(\overrightarrow{r},\omega) = 0, \tag{1.6}$$

where c is the speed of light in vacuum, and $\widetilde{E}(\overrightarrow{r},\omega)$ the Fourier transform of the electric field, $\overrightarrow{E}(\overrightarrow{r},t)$. The solution of Eq. 1.6 yields the fiber modes. If $\widetilde{E}(\overrightarrow{r},\omega)$ is written in cylindrical coordinates as $\overrightarrow{E} = E_\rho(\rho,\phi,z)\hat{\rho} + E_\phi(\rho,\phi,z)\hat{\phi} + E_z(\rho,\phi,z)\hat{z}$, Eq. 1.6 is then scalar for E_z because it does not couple to the radial and azimuthal components of the E-field. In cylindrical coordinates it can be written as:

$$\frac{1}{\rho}\frac{\partial}{\partial\rho}(\rho\frac{\partial E_z}{\partial\rho}) + \frac{1}{\rho^2}\frac{\partial^2 E_z^2}{\partial\phi^2} + \frac{\partial^2 E_z^2}{\partial z^2} + n^2 k_0^2 E_z = 0, \tag{1.7}$$

where $k_0 = \omega/c = 2\pi/\lambda$. Note that the same wave equation can be written for the z-component of the magnetic field (H-field). The other components of the E and H-fields can be calculated from the E_z and H_z components.

$$E_\rho = \frac{-i}{k^2 n^2(\rho) - \beta^2}(\frac{\omega\mu_0}{\rho}\frac{\partial H_z}{\partial\phi} + \beta\frac{\partial E_z}{\partial\rho}), \tag{1.8}$$

$$E_\phi = \frac{-i}{k^2 n^2(\rho) - \beta^2}(\frac{\beta}{\rho}\frac{\partial E_z}{\partial\phi} - \omega\mu_0\frac{\partial H_z}{\partial\rho}), \tag{1.9}$$

$$H_\rho = \frac{-i}{k^2 n^2(\rho) - \beta^2}(\beta\frac{\partial H_z}{\partial\rho} - \frac{\omega\varepsilon_i\varepsilon_0}{\rho}\frac{\partial E_z}{\partial\phi}). \tag{1.10}$$

$$H_\phi = \frac{-i}{k^2 n^2(\rho) - \beta^2}(\omega\varepsilon_i\varepsilon_0\frac{\partial E_z}{\partial\rho} + \frac{\beta}{\rho}\frac{\partial H_z}{\partial\phi}) \tag{1.11}$$

Separating the variables of the E-field such as $E_z(\rho,\phi,z) = R(\rho)\Phi(\phi)Z(z)$ where $Z(z) = exp(-i\beta z)$, the wave equation can be divided into two parts responding depending on ρ and ϕ only:

$$\frac{1}{R}\Big[\rho^2\frac{d^2R}{d\rho^2} + r\frac{dR}{d\rho}\Big] + (k_0^2 - \beta^2)\rho^2 = -\frac{1}{\Phi}\frac{d^2\Phi}{d\phi^2} = \nu^2. \tag{1.12}$$

The quantity β is the propagation constant of the wave [4]. From Eq. 1.12, E_z can be calculated. The other two components of the E-field and H-field, E_ρ, E_ϕ, H_ρ, and

H_ϕ can be calculated the same way using Eqs. 1.8 to 1.10 in a step-index profile. The general solution for E_z and H_z are:

$$E_z(\rho,\phi,z) = \begin{cases} AJ_n(\frac{u}{a}\rho)e^{in\phi}e^{-i\beta z}, & \rho < a, \\ A\frac{J_n(u)}{K_n(w)}K_n(\frac{w}{a}\rho)e^{in\phi}e^{-i\beta z}, & \rho > a, \end{cases} \tag{1.13}$$

$$H_z(\rho,\phi,z) = \begin{cases} CJ_n(\frac{u}{a}\rho)e^{in\phi}e^{-i\beta z}, & \rho < a, \\ C\frac{J_n(u)}{K_n(w)}K_\nu(\alpha_r\rho)e^{in\phi}e^{-i\beta z}, & \rho > a, \end{cases} \tag{1.14}$$

where J_n is the Bessel function of the first kind and K_n is the modified Bessel function of the second kind with $n = 0, 1, 2, ...$ representing the order of the Bessel functions. The quantities $u = a\sqrt{k^2 n_{core}^2 - \beta^2}$, $u = a\sqrt{\beta^2 - k^2 n_{clad}^2}$, and $u^2 + w^2 = k^2(n_{core}^2 - n_{clad}^2)a^2$ with a the core radius. The variables A, C, and β can be found using four boundary conditions satisfying continuity conditions on E_z, E_ϕ, H_z, and H_ϕ and the total mode amplitude. The boundary conditions result in the dispersion equations for each mode groups which are listed in Tab. 1.1. Three different sets of real modes can be found using the above equations, TE ($E_z = 0$), TM ($H_z = 0$), and HE and EH ($E_z \neq 0$ & $H_z \neq 0$). Figure 1.1 show the intensity profile of the real vector modes of a MMF with 6 modes, designated as a few-mode fiber (FMF). These modes are TE_{01}, TM_{01}, HE_{11x}, HE_{11y}, HE_{21a}, and HE_{21b}.

Table 1.1: Dispersion equations for the real modes of the fiber, TE, TM, and hybrid modes [4].

modes	**Dispersion Equation**
TE	$\frac{J_1(u)}{uJ_0(u)} = -\frac{K_1(w)}{wK_0(w)}$
TM	$\frac{J_1(u)}{uJ_0(u)} = -\left(\frac{n_{clad}}{n_{core}}\right)^2 \frac{K_1(w)}{wK_0(w)}$
Hybrid	$[\frac{J_n'(u)}{uJ_n(u)} + \frac{K_n'(w)}{wK_n(w)}][\frac{J_n'(u)}{uJ_n(u)} + (\frac{n_{clad}}{n_{core}})^2 \frac{K_n'(w)}{wK_n(w)}] = n^2(\frac{1}{u^2} + \frac{1}{w^2})[\frac{1}{u^2} + (\frac{n_{clad}}{n_{core}})^2 \frac{1}{w^2}]$

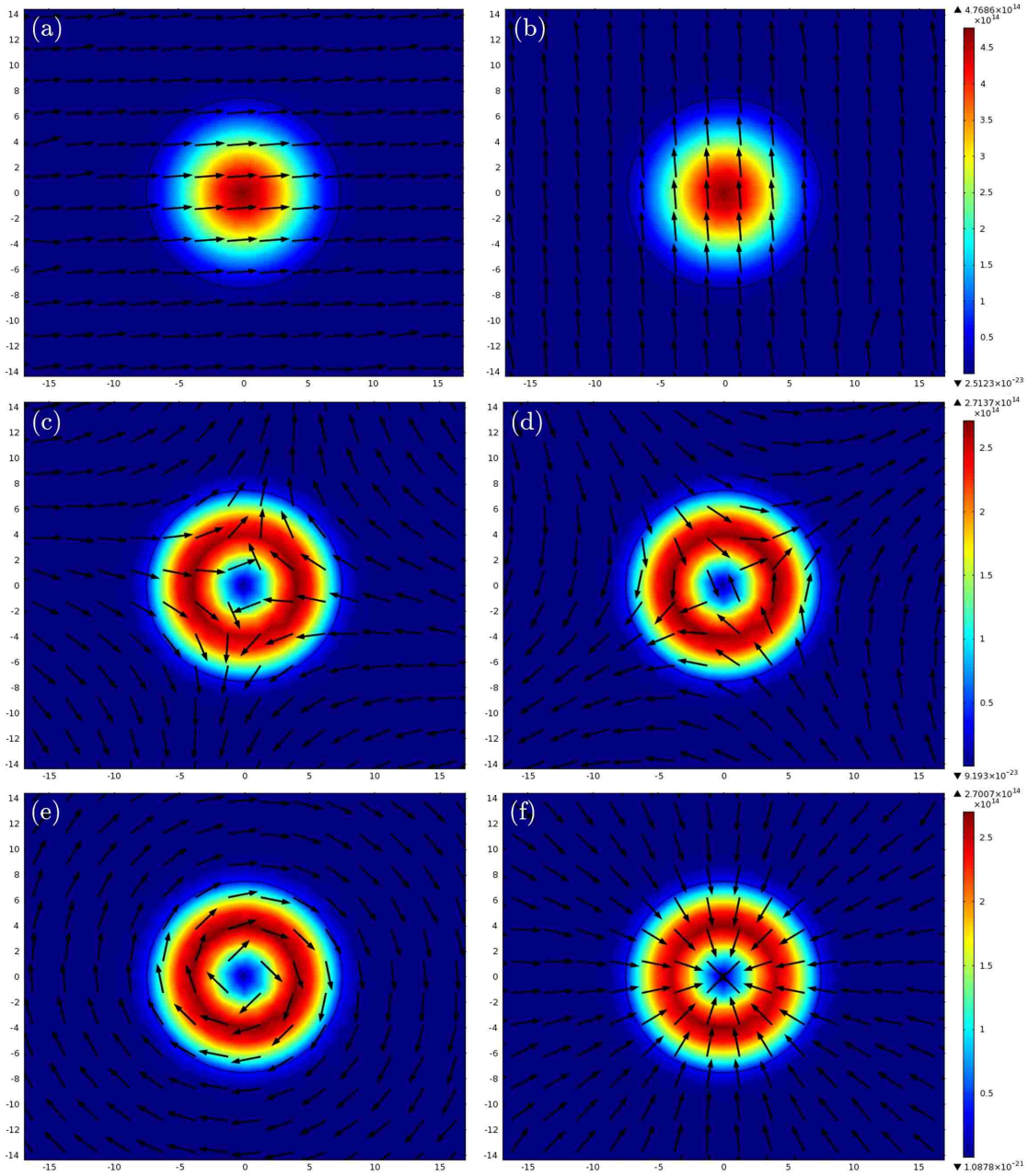

Figure 1.1: Mode profiles of (a) HE_{11x},(b) HE_{11y}, (c) HE_{21a}, (d) HE_{21b}, (e) TE_{01}, (f) TM_{01} modes of a FMF with 6 modes. The colors represent the intensity of the electric field and the arrows represent the polarization which is the direction of the electric field in the xy-plane.

As mentioned before, if the difference between cladding and core refractive indices is very small, of the order of 1%, then we can assume $n_{core} \cong n_{clad}$ in the equation of Tab. 1.1 where n_{core} and n_{clad} are the refractive indices of core and cladding respectively. Since in this approximation modes are not tightly confined in the core, it is called the weakly-guiding approximation and the fiber modes in this limit are the linearly polarized (LP) modes [30, 31, 32]. In the limit of weakly-guiding approximation, some of the real modes of the fiber that are non-degenerate, will have the same effective indices and can therefore linearly combine to generate the LP modes. The resulting LP modes have two degenerate polarizations in the x and y directions. To calculate the LP mode profiles, the wave equation can be rewritten for the scalar case, where E_z is negligible and therefore the WE only needs to be solved for E_x, E_y, H_x, and H_y [29]. Rewritten in the $n_{core} \cong n_{clad}$ approximation, the dispersion equations for the LP modes are shown in Tab. 1.2. Based on this approximation, each LP_{lm} mode can be constructed as a combination of two real modes of the fiber when they become degenerate. LP_{0m} modes are HE_{1m} modes LP_{1m} modes are a superposition of TE_{0m}, TM_{0m} and HE_{2m} modes and LP_{lm} modes are a combination of $\mathrm{HE}_{l+1,m}$ and $\mathrm{EH}_{l-1,m}$ modes. Figure 1.2 shows an example of how a superposition of TE_{01} and HE_{21} results in the LP_{11ax} mode [1, 34].

Table 1.2: Dispersion equations for the LP modes of the fiber [4].

modes	**Dispersion Equation**	**Corresponding Real Modes**
$LP_{0,m}$	$\frac{J_0(u)}{uJ_1(u)} = \frac{K_0(w)}{wK_1(w)}$	$HE_{1,m}$ and $TE_{0,m}$
$LP_{1,m}$	$\frac{J_1(u)}{uJ_0(u)} = -\frac{K_1(w)}{wK_0(w)}$	$HE_{2,m}$ and $TM_{0,m}$
$LP_{l,m}$	$\frac{J_l(u)}{uJ_{l-1}(u)} = -\frac{K_l(w)}{wK_{l-1}(w)}$	$HE_{l+1,m}$ and $EH_{l-1,m}$

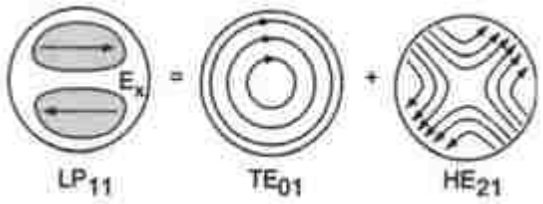

Figure 1.2: The LP_{11} mode is a superposition of the TE_{01} and HE_{21} modes. Note that the LP mode is linearly polarized, in contrast to the electric fields of the two constituent modes. E_x polarization is shown, although with appropriate superposition, an E_y polarized mode could been created [1].

1.2.2 Nonlinear Effects in Optical Fibers

Although the nonlinear coefficient (γ) of silica-based fibers is small compared to that of other fibers (such as doped and non-silica fibers), when the optical fiber is long enough and the power injected is high enough, nonlinear effects can occur along the fiber and become significant enough to affect the propagation of light in silica fibers. Some of these nonlinear effects are due to the fiber material, the fiber acting as the active nonlinear medium to generate effects such as Brillouin scattering and Raman scattering. The latter will be explained in greater details in Sec. 1.2.2. These scattering nonlinearities involve the vibrational modes of the glass material called phonons. The phonons involved in Raman scattering are optical phonons and those involved in Brillouin scattering are acoustic phonons. Optical phonons are out-of-phase vibrations of neighboring atoms in a unit cell and acoustic phonons are in phase vibrations between neighboring atoms within the unit cell. The new waves generated through the emission of a phonon are called Stokes waves and their frequencies are downshifted from the incident wave. In Brillouin scattering, the Stokes waves are generated at $\sim$10 GHz lower frequencies or $\sim$0.2 nm higher wavelengths as shown in Fig. 1.3(a). Anti-Stokes waves that are upshifted in frequency from the incident wave are also allowed by absorption of a phonon of the right energy and momentum. In Raman scattering in silica, the Stokes waves are generated at $\sim$13.2 THz lower frequencies relative to the incident light or $\sim$90 nm higher wavelengths as shown in Fig. 1.3(b). The Stokes waves generated in a Raman scattering process offer a very large gain bandwidth, which makes Raman attractive for amplification. If the fiber is seeded with a signal at the Stokes wavelength, the effects will

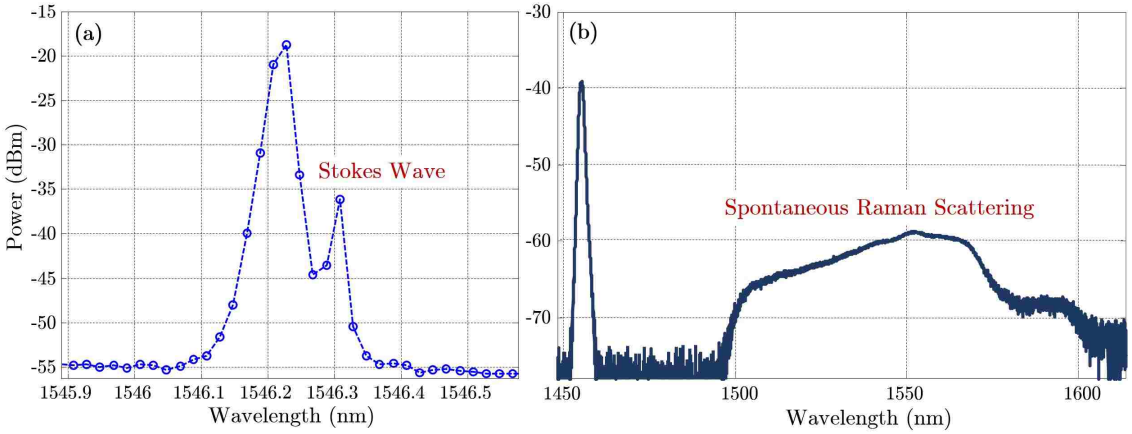

Figure 1.3: (a) The generated Stokes Wave due to the Brillouin scattering in a fiber with a single wavelength pump in the fiber at ∼1546.2 nm, (b) the generated Stokes Wave due to the spontaneous Raman scattering in a fiber with a single pump in the fiber at ∼1545 nm.

be stimulated resulting in stimulated Brillouin scattering (SBS) and stimulated Raman scattering (SRS) gain. Backward SBS in fiber transmission systems is mostly undesirable. It can be avoided by using different methods, e.g. by broadening the pump spectral bandwidth to increase the threshold for Stokes-wave generation as discussed in Sec. 3.3.

Other nonlinear effects such as four-wave mixing (FWM), self- (SPM) and cross- (XPM) phase modulations are due to the interaction between different optical waves in the fiber. These nonlinear effects, known as Kerr nonlinearities, are due to a light induced change in refractive index of the fiber. This change occurs due to the deformation of the electron orbits by the strong electric field of the optical wave ($|E|^2$) [4, 33, 35]. The refractive index then changes to $n = n_0 + n_2|E|^2$, where n_0 is the linear refractive index and n_2 is the Kerr coefficient which is of the order of 10^{-20} m^2/W for silica fibers. The quantity n_2 is related to the third-order susceptibility, $\chi^{(3)}$, of the glass material through $n_2 = \frac{3}{8*n_0} Re\big(\chi^{(3)}\big)$ equation. The Kerr and scattering nonlinear effects have been extensively studied in single-mode fibers (SMFs) [36, 37, 38, 39, 40].

In this thesis, I will focus on studying intermodal nonlinear effects such as FWM and SRS in FMFs to understand these effects in the presence of more than one spatial

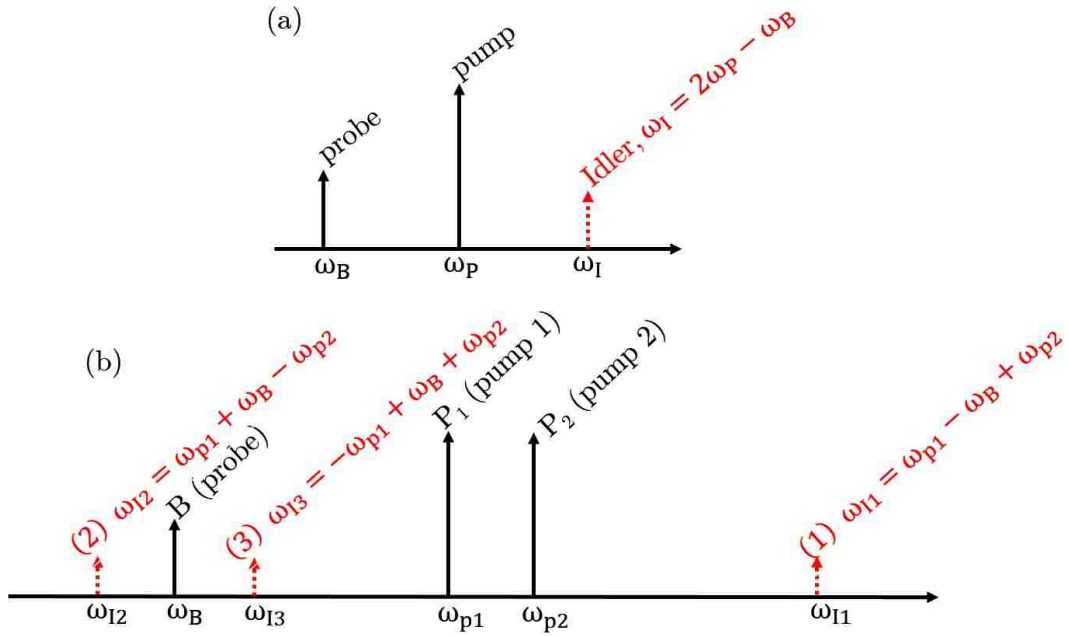

Figure 1.4: (a) Partially degenerate and (b) non-degenerate FWM pump-probe configurations.

mode. In the following, the theory of FWM and SRS is presented for the general case of a MMF when different waves included in these processes can be in different modes of the fiber. In the following, first the partially degenerate and non-degenerate FWM cases will be introduced along with their conservation laws, including energy and momentum conservation laws. Then, the coupled wave equations for the more general case of non-degenerate FWM in a MMF will be theoretically solved. At the end, the SRS will be discussed in more detail and the time-averaged equations for dual pumping of a MMF will be theoretically solved and the results will be interpreted.

Four-Wave Mixing

Four-wave mixing (FWM) is one of the Kerr nonlinear effects in fibers in which three waves combine to generate a fourth one, such that the total energy is conserved and phase-matching is satisfied. Energy conservation determines the frequency of the idler and the phase-matching condition determines whether the FWM effect will be

coherently added to itself as the wave propagates along the fiber. This effect can be observed in a SMF or a MMF with all the waves in the same mode, a single high power pump and a low power signal. A fourth wave is then generated with frequency ω_I where $\omega_I = 2\omega_p - \omega_B$, and ω_p and ω_B are the frequencies of pump and signal (or probe), respectively. This effect is called partially degenerate FWM. In the case of non-degenerate FWM with two high power pumps and a low-power signal all in the same mode, three combinations of the frequencies of these three waves are possible. The schematics of these effects are shown in Figs. 1.4(a) and (b). In the following, the general case of the non-degenerate FWM in a MMF is studied theoretically and the equation for the FWM efficiency is derived [41, 42]. In the presence of high-power pumps in the fiber, the induced polarization ($\overrightarrow{P}$) will have a nonlinear term in addition to the linear term used to derive Eq. 1.6 ($\overrightarrow{P} = \overrightarrow{P_L} + \overrightarrow{P_{NL}}$). The linear part was used previously along with Eq. 1.1 to find the modes of the MMFs. To study nonlinear effects, the nonlinear part of the polarization ($\overrightarrow{P_{NL}}$) must also be taken into account to include the effect of Kerr nonlinearities in the wave equation:

$$\nabla^2 \overrightarrow{E} - \frac{1}{c^2}\frac{\partial^2 \overrightarrow{E}}{\partial t^2} = \mu_0 \frac{\partial^2 \overrightarrow{P_L}}{\partial t^2} + \mu_0 \frac{\partial^2 \overrightarrow{P_{NL}}}{\partial t^2}. \tag{1.15}$$

For the general case of a MMF, if the electric fields of all the waves involved in the FWM are co-polarized, the total electric field can be written as a linear superposition of the individual fields (pumps, probe and idler) as in Eq. 1.16:

$$\overrightarrow{E} = \frac{1}{2}\hat{x}\sum_{j=1}^{4} E_j exp[i(\beta_j z - \omega_j t)] + c.c. \tag{1.16}$$

The resulting induced nonlinear polarization written in Eq. 1.17 has many terms including the ones related to Kerr effects such as SPM ($|E_i|^2 E_i$), XPM ($|E_i|^2 E_j$), sum frequency combination ($E_i\ E_j\ E_k\ exp[i(\beta_i+\beta_j+\beta_k-\beta_l)z - i(\omega_i+\omega_j+\omega_k-\omega_l)t]$) and FWM ($E_i\ E_j\ E_k^*\ exp[i(\beta_i+\beta_j-\beta_k-\beta_l)z - i(\omega_i+\omega_j-\omega_k-\omega_l)t]$).

$$\begin{aligned} \overrightarrow{P_{NL}} &= \epsilon_0 \chi^{(3)} \vdots \overrightarrow{E}\,\overrightarrow{E}\,\overrightarrow{E} \\ &= \epsilon_0 \chi^{(3)} [\frac{1}{2}\hat{x}\sum_{j=1}^{4} E_j exp[i(\beta_j z - \omega_j t)] + c.c.]^3. \end{aligned} \tag{1.17}$$

If we then substitute Eqs. 1.16 and 1.17 into Eq. 1.15 and use $E_j(\overrightarrow{r}) = F_j(x,y)A_j(z)$, a set of four coupled equations for the electric field amplitudes of the four waves will be derived that can then be studied numerically or theoretically. The resulted four equations for the field amplitudes $A_j(z)$ are [33, 41]:

$$\frac{dA_1}{dz} = \frac{in_2\omega_1}{c}\left[\left(f_{1111}|A_1|^2 + 2\sum_{k\neq 1} f_{11kk}|A_k|^2\right)A_1 + 2f_{1234}A_2^*A_3A_4e^{i\Delta\beta z}\right], \quad (1.18)$$

$$\frac{dA_2}{dz} = \frac{in_2\omega_2}{c}\left[\left(f_{2222}|A_2|^2 + 2\sum_{k\neq 2} f_{22kk}|A_k|^2\right)A_2 + 2f_{2134}A_1^*A_3A_4e^{i\Delta\beta z}\right], \quad (1.19)$$

$$\frac{dA_3}{dz} = \frac{in_2\omega_3}{c}\left[\left(f_{3333}|A_3|^2 + 2\sum_{k\neq 3} f_{33kk}|A_k|^2\right)A_3 + 2f_{3412}A_1A_2A_4^*e^{-i\Delta\beta z}\right], \quad (1.20)$$

$$\frac{dA_4}{dz} = \frac{in_2\omega_4}{c}\left[\left(f_{4444}|A_4|^2 + 2\sum_{k\neq 4} f_{44kk}|A_k|^2\right)A_4 + 2f_{4312}A_1A_2A_3^*e^{-i\Delta\beta z}\right], \quad (1.21)$$

where $\Delta\beta$ is the phase mismatch, the difference between the propagation constants of the four waves involved in the FWM process ($\Delta\beta = \beta_4 - \beta_1 - \beta_2 + \beta_3$) corresponding to the energy conservation law of $\omega_4 = \omega_1 + \omega_2 - \omega_3$. In these equations, ω_1, β_1, ω_2, and β_2 are the frequencies and propagation constants of the two pumps with amplitudes A_1 and A_2 along the z-axis, ω_3 and β_3 correspond to the probe or signal (A_3) and ω_4 and β_4 correspond to the idler (A_4). The quantity f_{ijkl} is defined as:

$$f_{ijkl} = \frac{\int\int_{\infty}^{-\infty} F_i^*(x,y)F_j^*(x,y)F_k(x,y)F_l(x,y)dxdy}{[I_iI_jI_kI_l]^{1/2}}, \quad (1.22)$$

where for $m = \{i,j,k,l\}$, $I_m = \int\int_{\infty}^{-\infty} |F_m(x,y)|^2 dxdy$ and $F_m(x,y)$ is the transverse electric field profile. It represents the degree overlap of the transverse electric field profiles of the four waves involved in the process. In Eqs. 1.18 to 1.21, the first terms in the parenthesis correspond to SPM for each wave, the second term to XPM between the four waves included in the process and the third term to FWM. In the case of two strong pumps, the first two terms will be important but they can be neglected for the signal and the idler in the undepleted pump approximation because of their low powers. In the undepleted pump approximation, Eqs. 1.18, 1.19, 1.20, and 1.21 can be simplified and the solution to the first two equations, Eqs. 1.18

and 1.19 are $A_1(z) = A_1(0)\ e^{i\delta k_1\ z}$, and $A_2(z) = A_2(0)\ e^{i\delta k_2\ z}$. The quantities δk_1 and δk_2 are written below:

$$\delta k_1 = \frac{n_2\omega_1}{c}\Big(f_{1111}P_1 + 2f_{1122}P_2\Big), \tag{1.23}$$

$$\delta k_2 = \frac{n_2\omega_2}{c}\Big(f_{2222}P_2 + 2f_{2211}P_1\Big), \tag{1.24}$$

where $P_1 = |A_1(0)|^2$ and $P_2 = |A_2(0)|^2$ are the input powers of the two waves. Substituting the solution for $A_1(z)$ and $A_2(z)$ into Eqs. 1.20 and 1.21 leads to these two equations:

$$\frac{dA_3}{dz} \simeq i\delta k_3 A_3 + iC_3 A_4^* e^{-i(\Delta\beta - \delta k_1 - \delta k_2)z}, \tag{1.25}$$

$$\frac{dA_4^*}{dz} \simeq -i\delta k_4 A_4^* - iC_4 A_3 e^{i(\Delta\beta - \delta k_1 - \delta k_2)z}, \tag{1.26}$$

where $P = P_1 + P_2$ is the total input pump power and

$$\delta k_3 = \frac{2n_2\omega_3}{c}(f_{3311}P_1 + f_{3322}P_2), \tag{1.27}$$

$$\delta k_4 = \frac{2n_2\omega_4}{c}(f_{4411}P_1 + f_{4422}P_2), \tag{1.28}$$

$$C_3 = \frac{2n_2\omega_3}{c} f_{3412}\sqrt{P_1P_2}, \tag{1.29}$$

$$C_4 = \frac{2n_2\omega_4}{c} f_{4312}\sqrt{P_1P_2}. \tag{1.30}$$

Using $A_3 = B_3 e^{i\delta k_3 z}$ and $A_4 = B_4 e^{i\delta k_4 z}$, Eqs. 1.20 and 1.21 become:

$$\frac{dB_3}{dz} = iC_3 B_4^* e^{-i\kappa z} \tag{1.31}$$

$$\frac{dB_4^*}{dz} = -iC_4 B_3 e^{i\kappa z}, \tag{1.32}$$

where $\kappa = \Delta\beta - \delta k_1 - \delta k_2 + \delta k_3 + \delta k_4$. The solutions to Eqs. 1.31 and 1.32 are

$$B_3 = \big[ae^{gz} + be^{-gz}\big]e^{-i\kappa z/2} \tag{1.33}$$

$$B_4^* = \big[ce^{gz} + de^{-gz}\big]e^{i\kappa z/2}, \tag{1.34}$$

where g is called the gain parameter defined as

$$g = \sqrt{C_3 C_4 - \left(\frac{\kappa}{2}\right)^2}. \tag{1.35}$$

It can be shown that the ratio of the generated idler to the input signal power is:

$$\frac{P_4}{P_3} \propto \frac{\sinh^2(gL)}{(gL)^2} \tag{1.36}$$

which can be approximated to Eq. 1.37 when $P_4 \ll P_3 \ll P$:

$$\frac{P_4}{P_3} \propto \frac{\sin^2(\kappa L/2)}{(\kappa L/2)^2}. \tag{1.37}$$

This expression determines the efficiency of the idler generated in the FWM process of $\omega_4 = \omega_1 + \omega_2 - \omega_3$. It is the ratio of the idler power to the signal (or probe) power in the FWM process and shows that the FWM efficiency changes as a function of the phase-mismatch. The efficiency of the FWM in a FMF is measured experimentally in Sec. 3.2 and Eq. 1.37 is then used to fit the experimental data as will be discussed later.

Stimulated Raman Scattering

As mentioned earlier in this chapter, the Raman scattering effect in fibers is a result of the interaction of light (photons) with the vibrational dynamics of the glass material (phonons). A pump photon can excite a vibrational transition in the glass material as a result of which a photon with a lower frequency is emitted, as illustrated in Fig. 1.5. Raman scattering can be stimulated by seeding the fiber with a signal at the Stokes wave frequency resulting in stimulated Raman scattering (SRS). Through SRS, the signal will be amplified by coherently coupling to the Raman pump. Therefore, the fiber itself acts as an amplifier. The Raman gain only depends on the wavelength separation between the pump and the signal, $\sim$13.2 THz in silica. The advantage of SRS is that it does not depend on the exact frequencies of the pump and signal but only on their difference. In addition, Raman amplification does not only occur in one direction inside the fiber, so that the signal and pump do not have to be propagating in the same direction. If the signal wave

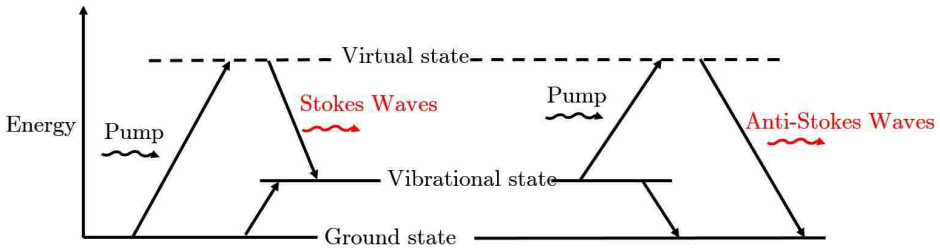

Figure 1.5: Stokes and Anti-Stokes waves generation in a spontaneous Raman scattering process.

propagates in the opposite direction of the pump wave, it will be amplified through the Raman process as well as if the signal wave propagates in the same direction as the pump wave. For both forward and backward Raman, the momentum is conserved through $\overrightarrow{k_{sw}} = \overrightarrow{k_p} - \overrightarrow{k_s}$, where $\overrightarrow{k_{sw}}$ is the wave vector of the phonons, and $\overrightarrow{k_p}$ and $\overrightarrow{k_s}$ are the wave vectors of the pump and signal, respectively [8, 43]. It should be noted that Raman gain is polarization dependent, therefore if the signal and pump are co-polarized, the gain will be maximum and itwill be minimum when they are orthogonally polarized with respect to each other. In silica fibers the Raman gain coefficient $g_R \sim 1 \times 10^{-13} m/W$ is much smaller than the SBS gain coefficient of $g_B \sim 5 \times 10^{-11} m/W$. Therefore, SRS in fibers requires much higher pump powers than SBS but it offers a much broader gain spectrum as shown in Fig. 1.3(b). The Stokes peak is a very wide peak of 100 nm so that a flat spectral gain can be achieved in a wavelength-division multiplexed (WDM) channel by combining several Raman pumps at nearby wavelengths. Raman amplifiers are also interesting since they can provide a larger bandwidth for amplification than Erbium-doped fiber amplifiers. Increasing the gain bandwidth is a solution to the capacity problem of SMFs as mentioned before. Figure 1.6 shows the schematics of a Raman fiber amplifier with forward and backward Raman pumps.

If two Raman pumps at the same frequency are launched into the same mode of a MMF, respectively in the forward and backward directions, along with a signal wave in a specific mode, the total electric fields in the fiber can be written as a superposition of the electric fields of the signal and pumps in different modes as written in Eq. 1.16. Assuming that all waves have the same polarization and that this polarization does not change as the waves propagate, the wave equation,

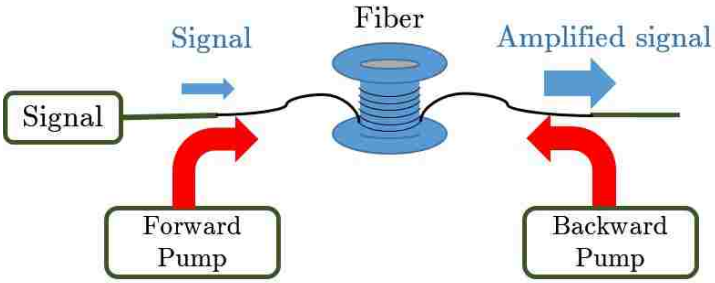

Figure 1.6: Schematic of a Raman amplifier using a fiber that is pumped in both backward and forward directions.

Eq. 1.15, including P_{NL} corresponding to Raman scattering will lead to the following time-averaged equations for the powers of the pumps and signal (or Stokes waves)[8, 12, 13, 42, 44, 45, 46]:

$$\frac{dP_j^s}{dz} = -\alpha_s P_j^s + \gamma_R \Big(\sum_i f_{ij} (P_i^{p+} + P_i^{p-}) \Big) P_j^s, \tag{1.38}$$

$$\frac{dP_i^{p+}}{dz} = -\alpha_p P_i^{p+} - \frac{\omega_p}{\omega_s} \gamma_R \Big(\sum_i f_{ij} P_j^s P_i^{p+} \Big), \tag{1.39}$$

$$\frac{dP_i^{p-}}{dz} = +\alpha_p P_i^{p-} + \frac{\omega_p}{\omega_s} \gamma_R \Big(\sum_i f_{ij} P_j^s P_i^{p-} \Big), \tag{1.40}$$

where P_j^s is the signal power in mode j, P_i^{p+} is the pump power in mode i in the forward direction, and P_i^{p-} is the pump power in mode i in the backward direction. ω_s and ω_p are the frequencies of the signal and pumps, respectively. We assume that both pumps have the same frequency. γ_R is related to the cross section for spontaneous Raman scattering and α_s and α_p are the absorption or loss coefficients of the fiber at the signal and pump frequencies, respectively. The coefficient f_{ij} is a simplified form of Eq. 1.22 for the case of two modes. The intensity overlap integrals, f_{ij}, are defined as:

$$f_{ij} = \frac{\int_0^{2\pi} \int_0^{+\infty} |F_i(r,\phi)|^2 |F_j(r,\phi)|^2 r \, dr \, d\phi}{\int_0^{2\pi} \int_0^{+\infty} |F_i(r,\phi)|^2 r \, dr \, d\phi \int_0^{2\pi} \int_0^{+\infty} |F_j(r,\phi)|^2 r \, dr \, d\phi}, \tag{1.41}$$

where F_i and F_j are the transverse electric field profiles of two waves in the ith mode and jth mode, respectively, written in cylindrical rather than cartesian coordinates [11]. The solutions to Eqs 1.39 and 1.40 in the undepleted pump approximation are

$$P_i^{p+} = P_0^{p+}\ e^{-\alpha_p z} \tag{1.42}$$

$$P_i^{p-} = P_L^{p-}\ e^{-\alpha_p (L-z)}, \tag{1.43}$$

where P_0^{p+} is the initial input power for the forward pump and P_L^{p-} for the backward pump. Substituting them in Eq. 1.38 and solving it analytically results in:

$$P_j^s(z) = P_j^s(0)\ \exp\Bigg[-\alpha_s z + \frac{\gamma_R}{\alpha_p} e^{-\alpha_p (L+z)} \big(e^{\alpha_p z} - 1\big) \big(e^{\alpha_p L} \sum_i P_0^{p+} + e^{\alpha_p z} \sum_i P_L^{p-}\big) \Bigg], \tag{1.44}$$

in which L is the length of the fiber. The $G_{\text{on-off}}$ is defined as [8]:

$$G_{\text{on-off}} = \frac{P_s^{\text{on}}(L)}{P_s^{\text{off}}(L)} \tag{1.45}$$

where $P_s^{\text{on}}(L)$ and $P_s^{\text{off}}(L)$ are the signal power at the fiber output when the pumps are on and off, respectively. In a MMF with negligible mode coupling, and assuming the small signal approximation, the signal power in a particular mode j will grow exponentially with a Raman gain of

$$G_{\text{on}-\text{off}} = \exp\left[\frac{\gamma_R}{\alpha_p} e^{-2\alpha_p L} \big(e^{\alpha_p L} - 1\big) \left(e^{\alpha_p L} \sum_i P_0^{p+} + e^{\alpha_p L} \sum_i P_L^{p-} \right) \right] \tag{1.46}$$

$$= \exp\left(g_R L_{\text{eff}} \left[\sum_i f_{ij} P_i^{p+} + \sum_i f_{ij} P_i^{p-} \right] \right), \tag{1.47}$$

where g_R is the Raman gain coefficient, L_{eff} the effective fiber length defined as $L_{\text{eff}} = (1 - e^{-\alpha_p L})/\alpha_p$ [8, 11], and P_i^{p+} the co-propagating pump power coupled into mode i, and P_i^{p-} the counter-propagating pump power in mode i. Equation 1.47 shows that the gain of each mode in a multi-mode Raman amplifier depends on its spatial overlap with the pump modes, f_{ij}. This will be discussed further in Sec. 4.2 when the gain of the signal in different modes is measured in both backward,

forward, and bi-directional pumping configurations in FMFs. In multi-mode Raman amplifiers, gain equalization is an important factor in selecting a certain pump configuration and has been studied in [10, 11, 47]. Ryf et al. have shown that it is possible to achieve equal amplification in MMFs by launching the pumps in the higher order modes [13]. The pumping scheme for equalized gain in all modes may change based on the refractive index profile of the fiber which changes the mode profiles and therefore the overlap integrals.

In the following chapters the nonlinear effects of FWM and SRS are characterized and studied experimentally in a MMF with only 3 spatial modes called FMF. In chapter 2, the FMF used in the experiments is characterized and its dispersion and transfer function are presented. The experimental free-space multiplexer setup is presented and the mode evolution inside the fiber is discussed. In chapter 3, the IM-FWM is studied in the graded-index FMF characterized in chapter 2 and the experimental results for FWM efficiency measurements are presented. The full FWM efficiency bandwidth measurement is presented for pump and probe detuning in the case of non-degenerate FWM with pumps in the higher order mode and the signal or probe in the fundamental mode. The impact of the relative polarization states of pumps and probe is also characterized. In chapter 4, Raman amplification in a 70-km FMF is measured for three different pump configurations in order to achieve equal amplification in all modes and a transmission experiment is performed in a loop of up to 1050 km of the same fiber and the results are discussed in Appendix A.

Chapter 2

Linear Properties of Few-Mode Fibers

2.1 Introduction

In this chapter, we report on the characterization of the FMF we have used to carry out our experiments. This fiber supports 3 spatial modes known as LP_{01}, LP_{11a} and LP_{11b} and two polarization states in the x and y directions for each one of them, resulting in a total number of 6 modes labeled as: LP_{01x}, LP_{01y}, LP_{11ax}, LP_{11ay}, LP_{11bx} and LP_{11by}. The LP_{11a} and LP_{11b} modes are degenerate modes that couple linearly to each other along the fiber and have the same propagation constant and group velocity. In the text we simply refer to these modes as LP_{11} modes or mode group. One advantage of the FMF used in our experiments is the limited number of modes, which enables a fundamental study of nonlinear effects without having to include complex effects due to the presence of higher order modes such as LP_{02} or LP_{12}. The results of this study of the linear and nonlinear effects between LP_{01} and LP_{11} modes can nonetheless be straightforwardly extended to MMFs with additional higher order modes.

In the following, we first characterize the linear properties of the fiber such as group velocity and the chromatic dispersion through a time-of-flight measurement using a 100 picosecond pulse generated with a continuous wave (CW) laser, a pulse pattern and an intensity modulator. Next, the transfer matrices that characterize

the mutual energy exchange between all 6 modes of the FMF are presented. The 6×6 transfer matrix reveals the linear coupling between different modes in the fiber-under-test. It has been measured using a heterodyne measurement setup.

2.2 Fiber parameters

One of the most important quantities characterizing FMFs and MMFs is the intensity overlap integral between two different modes, f_{ij}, defined in Eq. 1.41 because it determines the magnitude of the energy exchange between modes. The f_{ij} coefficients are calculated for a graded-index FMF with 3 spatial modes as is the case of the FMFs used in this work [5]. The inverse of the intensity overlap integral $1/f_{ii}$ is the effective area A^i_{eff} of the ith mode. The results are shown in Tab. 2.1 for the LP_{01}, $\text{LP}_{11\text{a}}$, and $\text{LP}_{11\text{b}}$ modes. For the degenerate LP_{11} mode group, we can use the complex notation $\text{LP}_{11\pm} = \text{LP}_{11\text{a}} \pm i\text{LP}_{11\text{b}}$ which results in a ring shaped intensity profile that is representative of the average intensity produced by the beating of the real vector modes TE_{01}, TM_{01}, and the two-fold degenerate HE_{21} modes that compose the $\text{LP}_{11\text{a}}$ and $\text{LP}_{11\text{b}}$ modes. This will later be explained in detail. In order to generate the higher order LP_{11} mode group in the fiber, the approximate mode profile of $\text{LP}_{11\text{a}}$ and $\text{LP}_{11\text{b}}$ modes are generated using $0/\pi$ phase plates. The coupling of these beam profiles into the fiber will generate a linear superposition of the real modes of the fiber that makes up the LP_{11} mode group. These real modes of the fiber include TE_{01}, TM_{01}, and the two-fold degenerate HE_{21} modes and all have a ring-shaped profile but different group velocities resulting in beating along the fiber [13]. Figure. 2.1 shows how the LP modes are generated from the real modes of the 6-mode FMF under study in this work. Fiber imperfections can also cause coupling between the degenerate modes in the LP_{11} mode group [46, 48, 49]. The results for f_{ij} are shown in Tab. 2.2 for the LP_{01}, LP_{11+}, and $\text{LP}_{11\text{-}}$ modes.

In order to characterize the linear properties of the fiber for the LP_{01} and degenerate LP_{11} modes, a time-of-flight measurement of the chromatic dispersion was conducted for the two modes. The results of an intensity transfer measurement between different modes is also presented in order to determine the transfer matrix components, as explained later in Sec. 2.5.

2.3 Fiber Chromatic Dispersion

In MMFs, each mode travels with a different propagation constant, $\beta(\omega)$, which is wavelength or frequency dependent. The propagation constant can be expanded in a Taylor series around an arbitrary frequency, ω_0 as:

$$\begin{aligned}\beta(\omega) &= \beta_0 + \beta_1(\omega-\omega_0) + \frac{\beta_2}{2}(\omega-\omega_0)^2 + \frac{\beta_3}{6}(\omega-\omega_0)^3 + ... \\ &= \beta(\omega_0) + \frac{(\omega-\omega_0)}{v_g(\omega_0)} - \frac{(\omega-\omega_0)^2}{\omega_0^2}\pi c D(\omega_0) \\ &\qquad + \frac{(\omega-\omega_0)^3}{\omega_0^3}\frac{\pi c\lambda_0}{3}\left(\frac{2D(\omega_0)}{\lambda_0} + S(\omega_0)\right) + ...,\end{aligned} \tag{2.1}$$

where

$$\beta_1 = (d\beta/d\omega)|_{\omega=\omega_0} = (1/v_g)|_{\omega=\omega_0}, \tag{2.2}$$

$$\beta_2 = (d^2\beta/d\omega^2)|_{\omega=\omega_0} = -\frac{2\pi c}{\omega_0^2}D(\omega_0), \tag{2.3}$$

$$\beta_3 = (d^3\beta/d\omega^3)|_{\omega=\omega_0} = \frac{2\pi c\lambda_0}{\omega_0^3}(\frac{2D(\omega_0)}{\lambda_0} + S(\omega_0)). \tag{2.4}$$

The quantity v_g is the group velocity of the wave at frequency ω_0 with $\lambda_0 = 2\pi c/\omega_0$. The parameters $D(\omega_0)$ and $S(\omega_0)$ respectively designate the dispersion and dispersion slope at ω_0, where $S = dD/d\lambda$. In order to study intermodal effects in a FMF, we need to know the group velocity $v_g(\lambda)$ or $v_g(\omega)$ of the fiber for wavelengths in the C-band for both modes in the FMF. The group velocity dispersion can then be calculated as:

$$D = \frac{-2\pi c}{\lambda^2}\frac{d\beta_1}{d\omega}, \tag{2.5}$$

where c is the speed of light in vacuum and λ is its wavelength and β_1 as in Eq. 2.2. The relative group velocities of the LP_{01} and LP_{11} modes are measured using the time-of-flight method. The experimental setup for this measurement is shown in Fig. 2.2. In this experiment, a 100 picosecond pulse is generated and coupled into the LP_{01} and LP_{11} modes of the fiber using the free-space multiplexer setup described later in this chapter in Sec. 2.4. Since the two modes travel at different group velocities, two separate pulses are observed at the fiber output, related to the two

different modes as shown in Fig. 2.3. The differential group delay (DGD) which is the difference between the propagation times between these two pulses, is measured to be 11 ns for this 4.7 km long fiber. Sweeping the carrier wavelength of the pulse in the C-band (1530-1565 nm), we can measure the wavelength dependence of the group velocity and calculate the chromatic dispersion of the fiber using Eq. 2.5.

Table 2.1: $1/f_{ij}$ (μm^2) for LP_{01}, LP_{11a}, and LP_{11b} modes of a graded-index FMF with six spatial and polarization modes [5].

modes	$\mathbf{LP}_{01}$	$\mathbf{LP}_{11a}$	$\mathbf{LP}_{11b}$
$\mathbf{LP}_{01}$	59.6	120.2	120.2
$\mathbf{LP}_{11a}$	120.2	79.8	239.4
$\mathbf{LP}_{11b}$	120.2	239.4	79.8

Table 2.2: $1/f_{ij}$ (μm^2) for LP_{01}, LP_{11+}, and LP_{11-} modes of a graded-index FMF with six spatial and polarization modes [5].

modes	$\mathbf{LP}_{01}$	$\mathbf{LP}_{11-}/\mathbf{LP}_{11+}$
$\mathbf{LP}_{01}$	56.9	120.2
$\mathbf{LP}_{11-}/\mathbf{LP}_{11+}$	120.2	119.7

In order to generate a 100 picosecond pulse, a tunable External Cavity Laser (ECL) is intensity modulated using a Mach-Zehnder modulator (MZM). The MZM is driven by a train of 100 picosecond electrical pulses generated by a Pulse Pattern Generator (PPG) and a 9-volt bias voltage. The bias voltage enables the adjustment of the intensity modulation on the transfer curve of the MZM at the Quadrature bias point which is the 50% transmission point or the region between the maximum and minimum of the transfer curve to transform the digital electric signal to a digital optical signal. Since intensity modulators based on $LiNbO_3$ are polarization

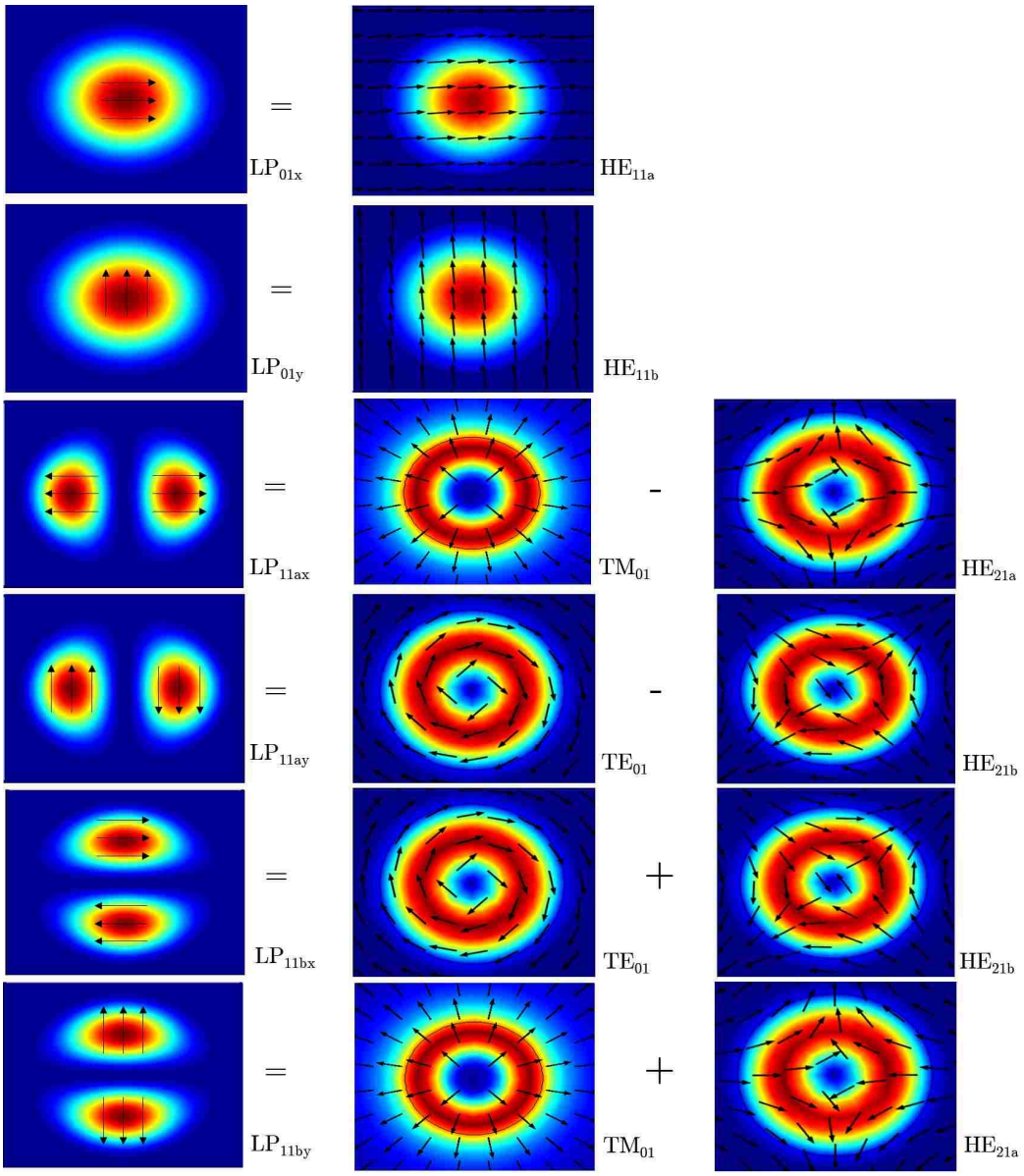

Figure 2.1: The different combinations of the real modes of the FMF under study, degenerate HE_{11a} and HE_{11b}, HE_{21a} and HE_{21b}, TM_{01} and TE_{01}, that generate the LP modes: the degenerate LP_{01x} and LP_{01y}, and degenerate LP_{11ax}, LP_{11ay}, LP_{11bx} and LP_{11by}. The x and y symbols in the subscripts represent the polarization direction of the modes in the xy-plane.

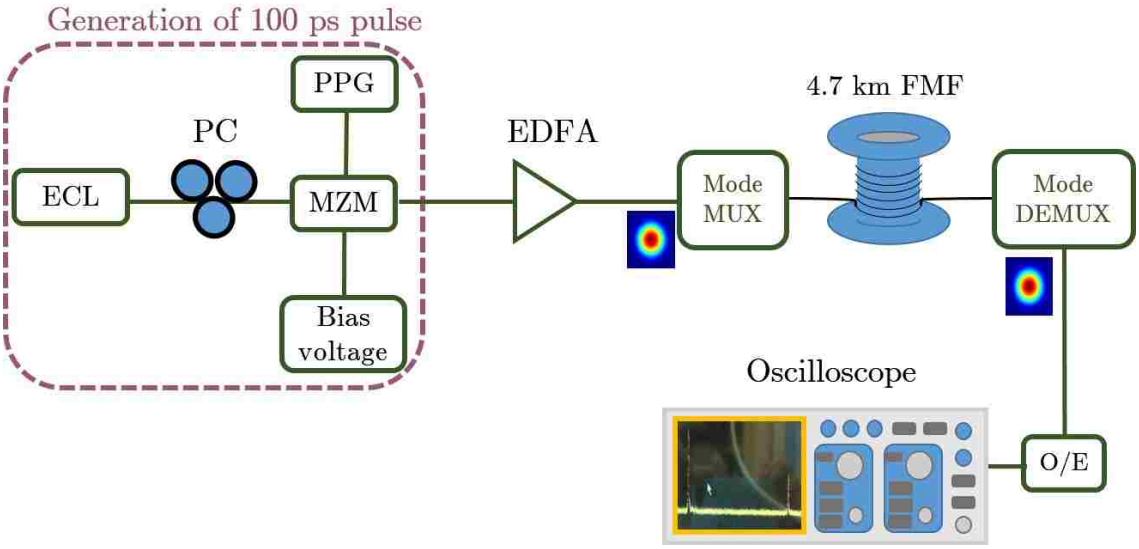

Figure 2.2: Experimental setup to measure the inverse of group velocities, $1/v_g$, for both LP_{01} and LP_{11} modes.

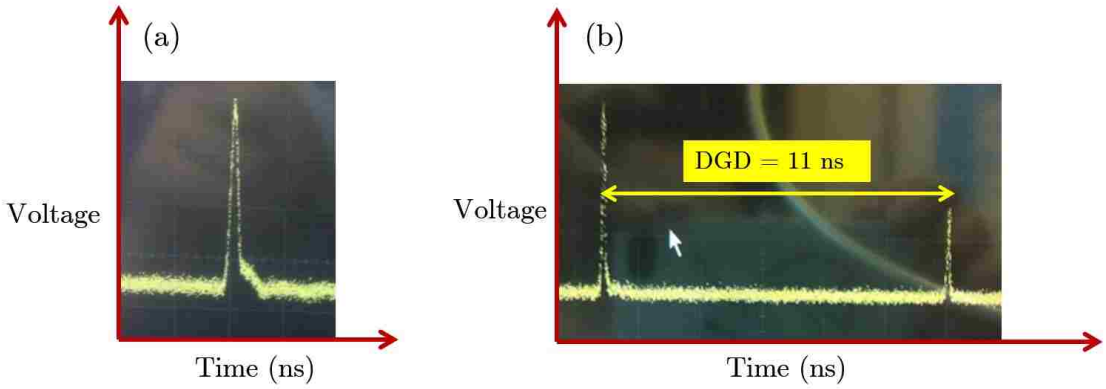

Figure 2.3: (a) Input and (b) output pulses of the 4.5-km-long FMF under study as measured using an oscilloscope. The DGD of the fiber at 1550 nm is measured to be 11 ns. The smaller peak corresponds to the LP_{11} mode group and the larger one to the LP_{01} mode; the LP_{11} mode group has a smaller v_g than the LP_{01} mode.

sensitive, a polarization controller (PC) is placed before the modulator to obtain the desired polarization orientation at the input of the modulator chip. The generated pulse is then amplified by an Erbium-doped fiber amplifier (EDFA) and coupled into the fiber using the LP_{01} port of the free-space mode multiplexer (Mode-MUX). The output of the fiber through the same LP_{01} port of the mode demultiplexer (Mode-DEMUX) is detected and converted to an electrical signal through an optical-to-electrical converter (O/E) and detected on an oscilloscope as shown in Fig. 2.3(b). The ECL wavelength is swept from 1530 nm to 1565 nm (C-band). The relative group delays between the two pulses is measured for each wavelength and the relative $1/v_g$ (ps/km) is calculated. Figure 2.4(a) shows the relative $1/v_g$ (ps/km) versus laser wavelength. It is fitted by a Taylor expansion as in Eq. 2.1 up to the β_3 term in the C-band for both modes. These dispersion curves show that the LP_{01} mode should be generated at a $\sim$16 nm longer wavelength than the LP_{11} modes for both to have the same group velocity. The calculated chromatic dispersion (D) is shown in Fig. 2.4(b). β_2 and β_3 can be calculated from the measurement of Figs. 2.4(a) and 2.4(b) using Eqs. 2.3 and 2.4. Based on the data of Fig. 2.4(a) and Eqs. 2.3 and 2.4, β_2 and β_3 of the two modes are calculated for a wavelength of 1550 nm and presented in Tab. 2.3.

Table 2.3: β_2 and β_3 values at 1550 nm for LP_{01}, LP_{11a}, and LP_{11b} modes of a graded-index FMF with six spatial and polarization modes.

modes	$\beta_2[ps^2/km]$	$\beta_3[ps^3/km]$
$\mathbf{LP_{01}}$	-22.8561	0.1674
$\mathbf{LP_{11a}/LP_{11b}}$	-23.9055	0.1658

2.4 Free-Space Mode-Multiplexer Setup

As mentioned in Sec. 2.3, in order to study intermodal effects between LP_{01} and LP_{11} mode group, we need to couple in and detect each mode separately in the

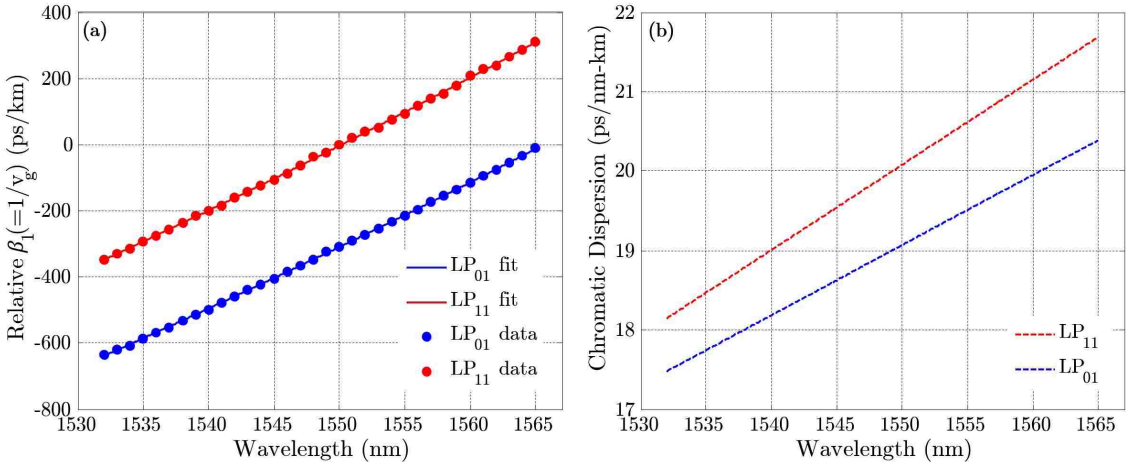

Figure 2.4: (a) Measured relative average inverse group velocities of the LP_{01} and LP_{11} modes as a function of wavelength for the 4.7-km FMF, (b) Chromatic dispersion curves for the two modes, LP_{01} (blue) and LP_{11} (red), calculated from the relative delay measurement between the modes.

fiber. The fiber we are using is a graded-index FMF in which, due to its radial symmetry, the true modes are of the Laguerre-Gaussian (LG) form, including LG_{00}, LG_{01} and LG_{10} [50, 51]. LG modes are approximation for infinite parabolic profile, but the graded-index FMF under study has a trench between the two claddings of the fiber and therefore its exact modes have to be calculated numerically. However, these modes can be approximated by the LP modes of a step-index fiber including LP_{01}, LP_{11a}, and LP_{11b} modes [50, 52]. Because both the collimated laser beam and the LP_{01} fiber mode have a Gaussian intensity profile, we only need to reduce the laser beam waist in order to couple it in to the fiber and excite its fundamental mode. As mentioned before, since LP modes are a superposition of the true modes of the fiber, the input beam propagates as a superposition of the true modes of the fiber (Fig. 2.1). However, these true modes of the fiber are non-degenerate and travel with different propagation constants (β). This results in the beating between them along the fiber, generating the LP mode profiles at beat length interval of the true modes. The beating between TE_{01} and twofold degenerate HE_{21} generates LP_{11ay} and LP_{11bx} modes and the beating of TM_{01} and HE_{21} generates LP_{11ax} and

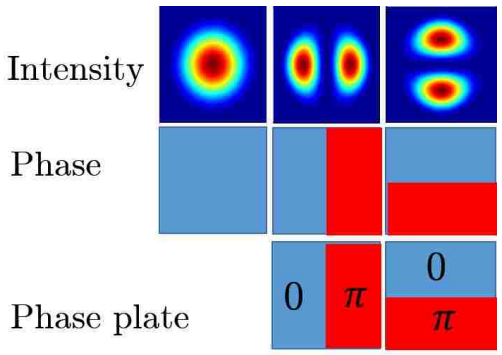

Figure 2.5: Mode profiles and phases for three spatial modes of a FMF.

LP_{11by} modes. To generate higher order modes LP_{11a} and LP_{11b} in this FMF, $0/\pi$ phase plates can be used as shown in Fig. 2.5 [53]. No phase plate is needed for the LP_{01} mode which corresponds to a true mode of the fiber, HE_{11}. We note that when using the phase plate the beam profile at the output is a superposition of the TE_{01} or TM_{01} and HE_{21} as shown in Fig. 2.1. Therefore, a ring shape profile is more appropriate to represent the spatial intensity profile of the LP_{11} mode group along the fiber [13]. Figure 2.6(a) shows the measured beam profile of the LP_{01} mode at the fiber output and Figs. 2.6(b) and 2.6(c) the beam profile of the LP_{11a} mode after the phase plate at the input and right at the fiber output, respectively. For the LP_{11b}, the phase plate is rotated by 90°, but the output beam profiles is found to be similar to the ring-shaped profile shown in Fig. 2.6(c). This is another indication that a ring shape profile ($LP_{11\pm} = LP_{11a} \pm iLP_{11b}$) is more suitable to represent the higher order LP_{11} mode group profiles in this fiber than LP_{11a} and LP_{11b} modes alone.

Figure 2.7 shows the free-space Mode-MUX setup used in our experiments. The Galilean telescope system used to reduce the beam diameter before launching into the fiber core is shown in Fig. 2.8. The focal lengths of the lenses are 75 mm and 1.49 mm. The beam waist of the GRIN lenses used as the collimators at the output of the SMFs is 0.5 mm. Therefore, the diameter of the beam (d) is found by D × f2 / f1 = 5 mm × 1.49 mm / 75 mm = 9.9 μm which is comparable to the core diameter of the graded index fiber ($\sim 15\mu m$) required for efficient launching. Two

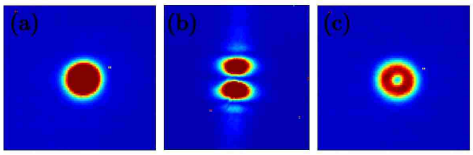

Figure 2.6: (a) LP_{01} mode profile of the fiber, (b) beam profile after the phase plate that couples into the fiber to excite the LP_{11a} mode, (c) mode profile of the LP_{11a} mode taken by an Infrared (IR) camera.

50:50 beam couplers are used to align the LP_{11a} and LP_{01} beams and a mirror is used for bending the LP_{11b} through a 50:50 coupler and therefore aligning all three beams together before going through the Galilean telescope system. The mirror and the couplers cause a loss in each path, thus reducing the maximum power that can be launched into the fiber. For LP_{01} this loss is 8 dB, for LP_{11a} path without the phase plate 7 dB and for the LP_{11b} path without the phase plate 6 dB. With the phase plates the losses in the LP_{11a} and LP_{11b} paths will increase by 2-4 dB. If more power needed to be launched into the fiber through either one of the LP_{11} modes, the Mode-MUX setup can be slightly modified by removing the mirror and replacing the two 50:50 beam splitters by one 30:70 beam splitter, sending 70% of the LP_{11a} beam into the fiber which reduces the loss in this arm by at least 3 dB. This modification helps launch more pump power into the fiber in the LP_{11} modes as will be discussed in Chap. 3. The same setup is used as Mode-DEMUX; the fiber output travels through the Galilean telescope system and 50:50 beam splitters to measure the power in each mode.

2.5 Linear Transfer Matrix Measurement

To understand the coupling between different modes in the fiber, a measurement was performed using an interferometric technique. The result of this measurement is a complex amplitude transfer matrix in which each element of the matrix indicates the strength of the coupling between two particular modes. The 6×6 transfer matrix, $\mathbf{T}(\omega)$, of the FMF was measured using the swept-wavelength interferometry

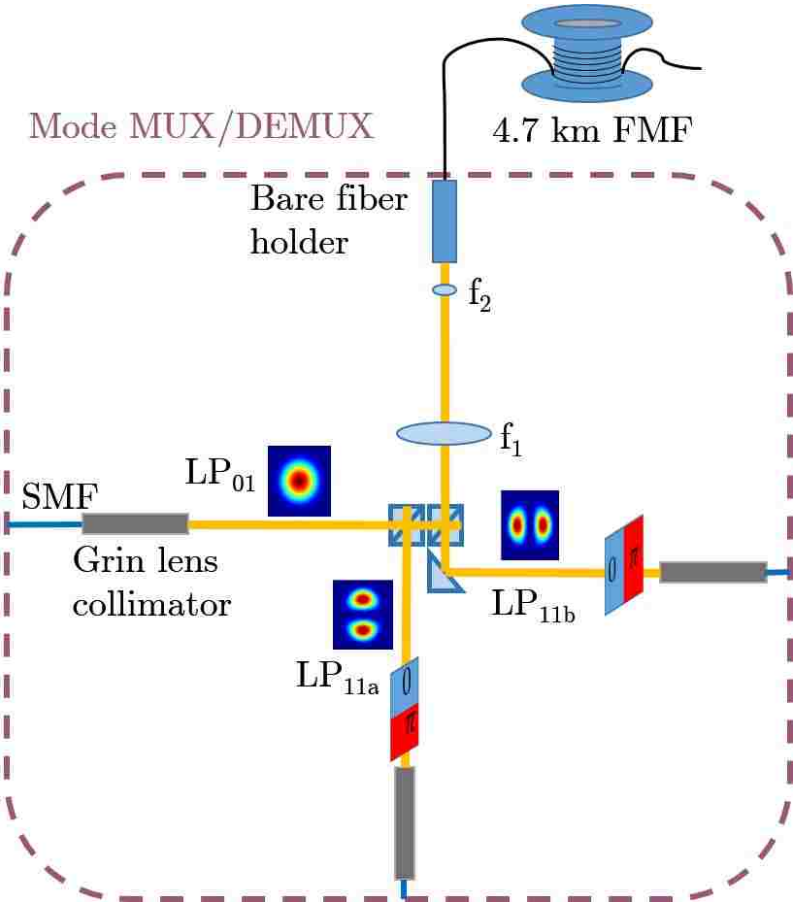

Figure 2.7: Experimental setup for Mode-MUX and mode-DEMUX for a FMF with three spatial modes.

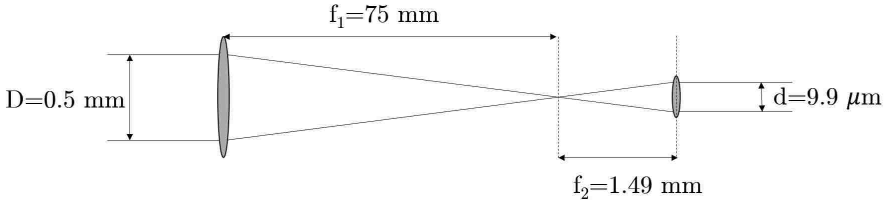

Figure 2.8: The Galilean telescope system used to reduce the beam diameter before launching into the fiber core.

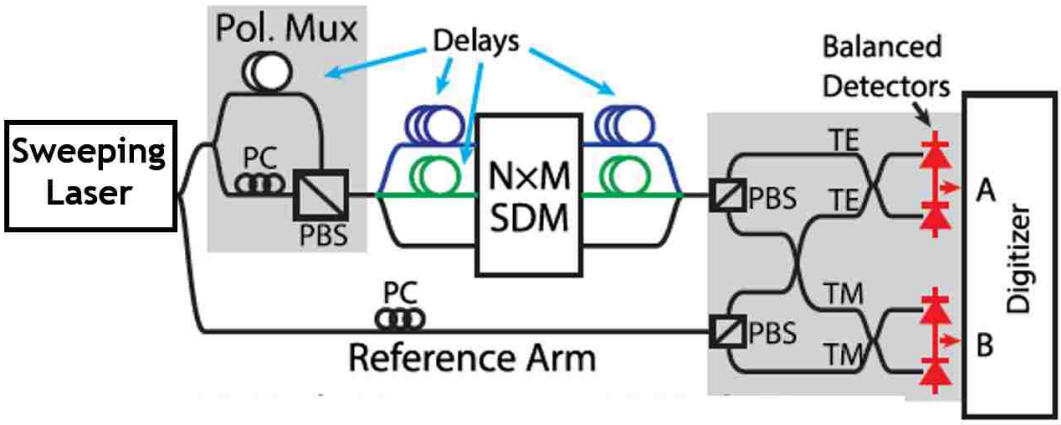

Figure 2.9: Experimental setup for the SDM-OVNA for a FMF [2].

technique in the linear regime where $\overrightarrow{E}_{out} = \mathbf{T}(\omega)\overrightarrow{E}_{in}$. The measurement was done using an optical vector network analyzer with a spatial division multiplexer (SDM-OVNA), allowing a complete characterization of the 6×6 transfer matrix of the system in a single scan, including the 6 modes, LP_{01x}, LP_{01y}, LP_{11ax}, LP_{11ay}, LP_{11bx} and LP_{11by} [2]. This method is based on swept wavelength interferometry (SWI) used for measuring the 2×2 Jones matrix in single mode systems. In single mode systems, the low power output from a tunable laser is coupled into the fiber and the transfer to all possible modes and polarizations is characterized at the output [54, 55]. The experimental setup for this measurement is shown in Fig. 2.9 where PBS stands for polarization beam splitter. The output of the tunable laser source is divided into two paths, one is the reference path to a PBS and two detectors and the other path is through a polarization multiplexer (Pol.MUX) after which the orthogonally polarized beams are separately coupled into different modes and propagated through the FMF. The transmitted beams at the Mode-DEMUX are then recombined and split between two orthogonal polarizations by another PBS, with each polarization going to a different detector where it interferes with one arm of the reference beam. Through this interferometric heterodyne detection technique, the coupling between different modes and polarizations is detected by measuring phase and amplitude.

Figures 2.10, 2.11, and 2.12 show a subset of 24 of the 36 transfer functions versus wavelength for all possible linear couplings between the 6 linearly polarized

fiber modes. Figure 2.10(a) shows transmission versus wavelength for all four input-output combinations between LP_{01x} and LP_{01y}. A small wavelength dependence of the transfer functions is observed over 4-nm wavelength sweep. Figure 2.10(b) shows the transfer function for the case in which the input is in the LP_{01x} or LP_{01y} and the transmission is measured in the LP_{11ax} and LP_{11ay} modes. These measurements reveal the very weak coupling that exists between LP_{01x} or LP_{01y} on the one hand and all the LP_{11} modes on the other.

In contrast, Fig. 2.11(a) shows the transfer matrix elements for the case in which the input wave is coupled into the LP_{11ax} mode and output is measured in the LP_{11ax}, LP_{11ay}, LP_{11bx}, and LP_{11by} modes, while Fig. 2.11(b) shows the transfer matrix elements for the case when the input is in LP_{11ay}: a definite wavelength dependent power transfer is observed between these LP_{11} modes. Figures 2.12(a) and 2.12(b) illustrate a similar power transfer between LP_{11bx} or LP_{11by} and other LP_{11} modes. One observes a very strong linear coupling between these modes as well as a pronounced wavelength dependence of the transfer. These measurements are consistent with calculations of the linear transfer between higher order LP modes in an ideal FMF that does not possess the random birefringence of the FMF under study. As mentioned earlier, the LP_{11a} and LP_{11b} modes are not the real modes of the fiber but a superposition of the non-degenerate real modes. Non-degenerate real modes have different group velocities, which results in beating between them. The difference in the group velocities of the real modes is the cause of the wavelength dependence of the transfer coefficients between higher order LP modes. Such sharp wavelength dependence results in very different evolutions of waves that are closely spaced in wavelength, independent of their relative polarization states. Based on the strong wavelength dependence of the linear transfer function between LP_{11a} and LP_{11b} modes, one should expect a strong wavelength dependence of FWM involving these modes. In addition, for any specific wavelength and input polarization of the LP_{11a} and LP_{11b} modes, there also exists a linear coupling between the various polarizations of the same mode. Therefore, as will be discussed in Chapter 3, although the relative polarization states of two waves in the FWM experiment can be set in the Mode-MUX, there will be a strong coupling between all the polarization states of the mode, a coupling that may affect the FWM efficiency.

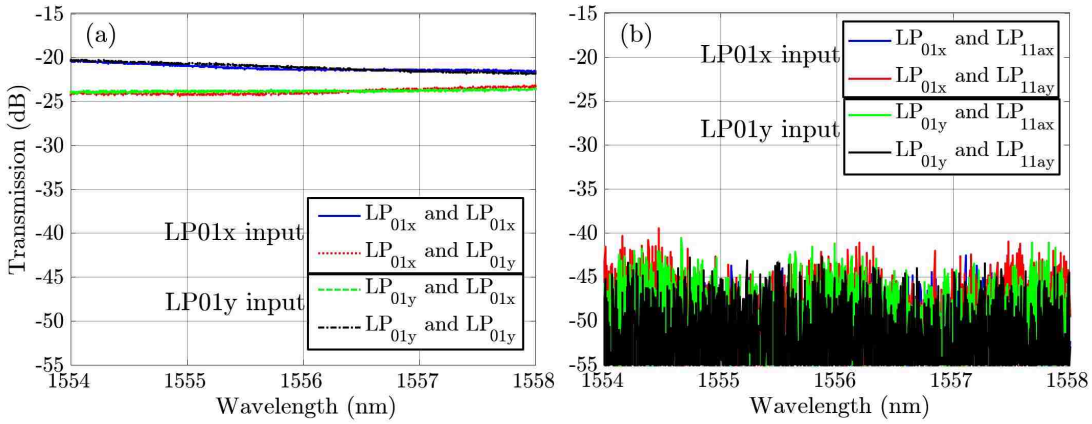

Figure 2.10: Measured amplitude transfer functions between various modes of the 6-mode FMF as a function of wavelength: (a) Four coupling combinations between LP_{01x} and LP_{01y}; (b) Four coupling combinations between LP_{01x} and LP_{01y} with LP_{11ax}, and LP_{11ay} modes.

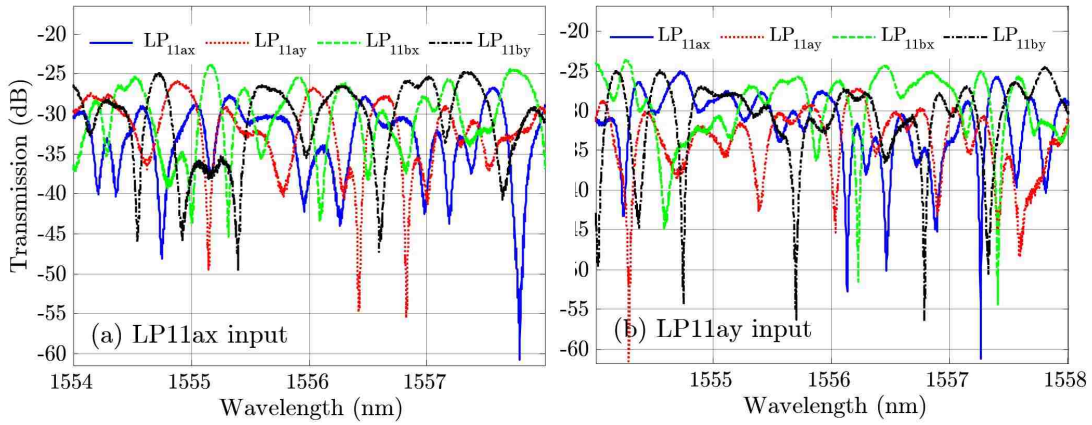

Figure 2.11: Measured amplitude transfer functions between various modes of the 6-mode FMF as a function of wavelength: (a) Four coupling combinations for coupling from (a) LP_{11ax} and (b) LP_{11ay} to all four modes of LP_{11ax}, LP_{11ay}, LP_{11bx}, and LP_{11by}.

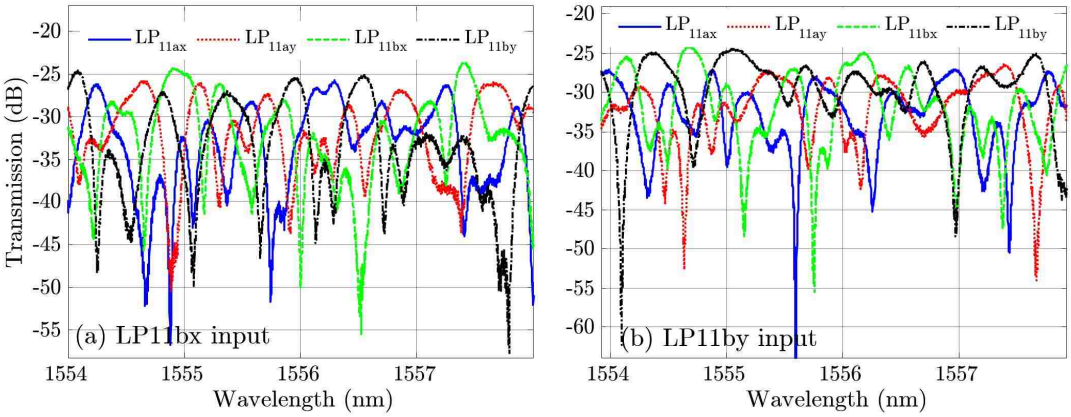

Figure 2.12: Measured amplitude transfer functions between various modes of the 6-mode FMF as a function of wavelength: (a) Four coupling combinations for coupling from (a) LP_{11bx} and (b) LP_{11by} to all four modes of LP_{11ax}, LP_{11ay}, LP_{11bx}, and LP_{11by}.

2.6 Conclusion

In this chapter we have characterized the linear properties of the FMF under study, including group delay, dispersion and dispersion slope. Characterizing these properties is necessary in order to determine the phase mismatch between LP modes, as is discussed in Chapter 3, and find the perfect phase-matched condition for intermodal FWM. We also presented the results of a transfer function measurement that represent the coupling between different modes of the fiber at different polarizations and wavelengths. The LP_{01} mode doesn't exhibit significant wavelength dependent transmission but the modes in the LP_{11} mode group do show considerable wavelength dependent transmission. The transmission matrix measurement is in the linear regime for laser power less than 0 dBm but the results are also important to understand the mode behavior in the nonlinear regime. In Chapter 3, the intermodal FWM effect is studied in the same FMF that was characterized in this chapter.

Chapter 3

Four-Wave Mixing in Few-Mode Fibers

3.1 Introduction

In this chapter, first a theoretical study of the Inter-modal Four-Wave Mixing (IM-FWM) efficiency bandwidth is presented for the non-degenerate FWM pump-probe configuration as shown in Fig. 1.4(b). Two different pump and probe configurations are possible: first pump in the LP_{01} mode and the second pump and the probe in the LP_{11} mode or two pumps in the LP_{11} mode and the probe in the LP_{01} mode. We refer to these configurations as "*multiple-mode pumps configuration*" and "*same-mode pumps configuration*", respectively. In the "*same-mode pumps configuration*" we can study the effect of the relative polarizations of the two pumps on the IM-FWM. The $\Delta\beta = 0$ equation is solved and the efficiency bandwidths are calculated. The IM-FWM for the "*same-mode pumps configuration*" is then experimentally studied and the results of measurements in a 4.7 km graded-index FMF is presented. In the non-degenerate IM-FWM experiment, two pumps are injected in the same higher order spatial mode and a probe in the fundamental mode. This will generate IM-FWM effects in the fundamental mode, therefore only the port corresponding to the fundamental mode needs to be monitored in the demultiplexer. The fluctuations of IM-FWM is then investigated for a 1 nm detuning of the probe with a higher resolution of the OSA (0.01 nm resolution). The effect of polarization is also investigated by respectively scrambling the polarization of

the pumps and probe. In the following, first the theoretical analysis of IM-FWM is discussed and then the experimental setup and results are presented.

3.2 Theoretical Analysis of IM-FWM

In order to observe the FWM nonlinear effect, the energy and momentum conservation laws must be simultaneously satisfied. The latter is known as the phase-matching condition. The phase-mismatch, $\Delta\beta$, defined as the difference between the propagation constants of the idler and the three waves involved in the process, may be due to the waveguide dispersions, material dispersion, and nonlinear effects. In order to maximize FWM this phase-mismatch should be zero ($\Delta\beta = 0$) for the phase-matching condition to be fully satisfied and idlers generated at frequencies that follow their respective energy conservation laws. In SMFs, the phase-matching condition can only be satisfied if the pump wavelength is close to the zero dispersion wavelength (ZDW) and in the anomalous dispersion regime, so that the waveguide and nonlinear dispersion cancel the material dispersion [36, 43, 56]. In a FMF however, one can take advantage of the different dispersion curves of the supported spatial modes such that their respective group velocities satisfy the overall phase-matching condition for a particular FWM process [4, 17]. This provides much more flexibility and an opportunity to study different experimental conditions in which these effects can be observed, modified or eliminated. In the case of non-degenerate IM-FWM in FMFs, phase-matching conditions can be achieved by either launching both pumps in the same mode and the probe in a different mode (*same-mode pumps configuration*), or one pump and the probe in the same mode and the second pump in a different mode (*multiple-mode pumps configuration*) as shown in Fig. 3.1. Using the fact that the different modes have different group velocities and propagation constants, intermodal phase-matching can be achieved through a suitable choice of wavelengths. In each of these configurations, it is also possible to control the relative polarization of the two waves in the same mode by sending them through a coupler and polarization beam splitter (PBS) before launching them into the fiber as shown in Fig. 3.5.

As seen from Eq. 1.21, the propagation equations in FMFs are governed by the coefficients f_{ijkl} defined in Eq. 1.22 [50, 57, 58]. In order to calculate f_{ijkl}, the spatial

field distributions of the higher-order modes, LP_{11a} and LP_{11b}, can be written as a linear combination, $F_{\pm}(x,y) = F_{11a}(x,y) \pm iF_{11b}(x,y)$, because these two spatial modes linearly couple to each other as they propagate along the fiber. $F_{11a}(x,y)$ and $F_{11b}(x,y)$ are the respective spatial electric field distributions of the two orthogonal and degenerate LP_{11a} and LP_{11b} modes. It is of great importance to mention that LP modes are not the real modes of the fiber but a combination of the real vector modes all of which have a ring-shaped intensity profile. From the intensity overlap integrals, f_{ijkl}, we can determine the various possible IM-FWM processes and find the spatial distribution of the resulting idler waves [49]. For non-degenerate FWM in FMFs, based on symmetry, if the two pumps are coupled into the LP_{11a} or LP_{11b} modes and the probe into the LP_{01} mode, the overlap intensity integral, f_{ijkl}, will be nonzero only for the idler in the LP_{01} mode [49]. In the present study, both pumps are coupled in either one of the LP_{11} modes and the probe in the LP_{01} mode and the idlers are only observed in the LP_{01} mode of the Mode-DEMUX. This configuration will then help simplify the measurements by only monitoring the LP_{01} port of the Mode-DEMUX. If both pumps are coupled into the LP_{01} mode and the probe into one of the LP_{11} modes, the idlers can be observed in both LP_{11a} and LP_{11b} ports of the Mode-DEMUX shown in Fig. 2.7 because of their linear coupling along the fiber. Therefore, a simultaneous measurement of the LP_{11} ports in the demultiplexer is needed to fully characterize the IM-FWM effect in the fiber.

Based on the IM-FWM analysis in [26], three different first-order idlers should be observed corresponding to the three possible processes numbered in Fig. 3.1. These processes and the corresponding energy conservation relations with their respective phase-matching conditions are as follows:

$$\text{(proc. 1)}\ \omega_{I1} = \omega_{p1} - \omega_B + \omega_{p2}, \quad \beta^{I1} = \beta^{p1} - \beta^B + \beta^{p2}, \tag{3.1}$$

$$\text{(proc. 2)}\ \omega_{I2} = \omega_{p1} + \omega_B - \omega_{p2}, \quad \beta^{I2} = \beta^{p1} + \beta^B - \beta^{p2}, \tag{3.2}$$

$$\text{(proc. 3)}\ \omega_{I3} = -\omega_{p1} + \omega_B + \omega_{p2}, \ \beta^{I3} = -\beta^{p1} + \beta^B + \beta^{p2}. \tag{3.3}$$

The labels $p1$ and $p2$ designate the first and second pumps and B the probe, while ω_i and β^i with $i \in \{I_i, p1, p2, B\}$ are the angular frequencies and propagation constants of the respective waves. I_i with $i = \{1, 2, 3\}$ corresponds to idlers generated in processes 1 (proc.1), 2 (proc.2), and 3 (proc.3), respectively. For the measurement

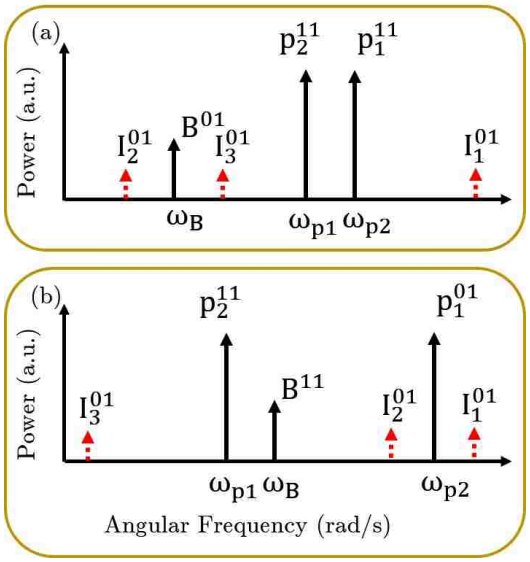

Figure 3.1: (a) *Same-mode pumps configuration* with two pumps in the LP_{11} mode and a probe in the LP_{01} mode. (b) *Multiple-mode pumps configuration* with a pump and the probe in the LP_{11} mode and the second pump in the LP_{01} mode. The three possible idlers are shown as dashed arrows and numbered (lower index) according to the IM-FWM process that generates them (see text).

performed in the *same-mode pumps configuration* as shown in Fig. 3.1(a), only processes 2 and 3, corresponding respectively to Eqs. (3.2) and (3.3) were observed [59] and for the measurement performed in the *multiple-mode pumps configuration* as in Fig. 3.1(b), only processes 1 and 2, corresponding respectively to Eqs. (3.1) and (3.2) were observed [48]. Process 1 in the *same-mode pumps configuration* and process 3 in the *multiple-mode pumps configuration* were not observed possibly because of the greater sensitivity of their phase-matching conditions to fluctuations in the fiber which will be discussed later in this section. In summary, it can be possibly explained by the Taylor expansion of the phase-matching conditions of these processes using Eq. 2.1. As will be shown later in this chapter, the Taylor expanded phase-mismatch for the missing processes in both configurations includes the first term (β_0) that makes the phase-matching conditions more sensitive to the index fluctuations in the fiber. In the following, the phase-mismatch for the one of the configurations shown in Fig. 3.1 will be theoretically calculated as an example and the efficiency of the FWM effects will be studied for different cases to find its dependency to pump and probe wavelengths.

3.2.1 Same-mode Pumps Configuration

In order to find the FWM efficiency bandwidth theoretically, it is necessary to calculate the phase-mismatch in the FMF. In this section the phase-mismatch in the FMF under study is derived theoretically for processes 1, 2 and 3. In order to find the IM-FWM bandwidth which is proportional to $\mathrm{Sinc}^2(\kappa L/2)$ as shown in Eq. 1.37, it is necessary to calculate the phase-mismatch, $\Delta\beta$, in the FMF because $\kappa = \Delta\beta - \delta k_1 - \delta k_2 + \delta k_3 + \delta k_4$. Since δk_1, Eq. 1.23, δk_2, Eq. 1.24, δk_3, Eq. 1.27, and δk_4, Eq. 1.28, are proportional to the total pump power and intensity overlap integral between the modes in the fiber, they can be ignored considering that they are the nonlinear modification of phase-mismatch. It will be shown later in this section that they don't have a significant effect on the IM-FWM bandwidth. The FWM efficiency can therefore be calculated from $\mathrm{Sinc}^2(L\Delta\beta/2)$. For all processes in Eqs. 3.1-3.3, the phase-mismatch due to dispersion can be calculated by expanding the βs in a Taylor expansion as in Eq. 2.1 around an arbitrary frequency (ω_0) truncated at the third-order term. As in Fig. 3.1(a) for the *same-mode pumps configuration*, designating ω_{p1} and ω_{p2} the frequencies of the two pumps in the LP_{11} mode group and ω_B the frequency of the probe in the LP_{01} mode, and taking into account that the idler, ω_I, is generated in the LP_{01} mode group due to symmetry as mentioned earlier in this chapter, the phase-mismatch for process 1 as defined in Eq. 3.1 can be written as:

$$\begin{aligned}
\Delta\beta_{(\text{proc. 1})} &= \beta^{I1} - \beta^{p1} + \beta^{B} - \beta^{p2} \\
&\approx \beta_0^{I1} + \beta_1^{I1}\Delta\omega_{I1} + \frac{\beta_2^{I1}}{2}\Delta\omega_{I1}^2 + \frac{\beta_3^{I1}}{6}\Delta\omega_{I1}^3 - \beta_0^{p1} - \beta_1^{p1}\Delta\omega_{p1} - \frac{\beta_2^{p1}}{2}\Delta\omega_{p1}^2 \\
&- \frac{\beta_3^{p1}}{6}\Delta\omega_{p1}^3 + \beta_0^{B} + \beta_1^{B}\Delta\omega_{B} + \frac{\beta_2^{B}}{2}\Delta\omega_{B}^2 + \frac{\beta_3^{B}}{6}\Delta\omega_{B}^3 - \beta_0^{p2} - \beta_1^{p2}\Delta\omega_{p2} \\
&- \frac{\beta_2^{p2}}{2}\Delta\omega_{p2}^2 - \frac{\beta_3^{p2}}{6}\Delta\omega_{p2}^3.
\end{aligned} \tag{3.4}$$

where $\Delta\omega_i = \omega_i - \omega_0$ with $i \in \{I, p1, p2, B\}$, and $\beta_k^j(\omega_0) = d^k\beta^j/d\omega^k$ evaluated at ω_0 with $k = \{1, 2, 3\}$ and $j \in \{11, 01\}$ in the Taylor expansion defined in Eqs. 2.2-2.4. ω_0 is an arbitrary frequency chosen for the Taylor expansion of the propagation constants of the waves. Since the pumps are in the same LP_{11} mode, and the probe and idler in the LP_{01} mode in our experiments, we can write $\beta_0^{I1}(\omega_0) = \beta_0^{B}(\omega_0) = \beta_0^{01}$

and $\beta_0^{p1}(\omega_0) = \beta_0^{p2}(\omega_0) = \beta_0^{11}$. The same equations apply to $\beta_1^{01/11}$,$\beta_2^{01/11}$, and $\beta_3^{01/11}$. Therefore, the phase-mismatch for process 1 can be written as

$$\begin{aligned}\Delta\beta_{(\text{proc. 1})} \approx 2\beta_0^{01} + \beta_1^{01}(\Delta\omega_{I1} + \Delta\omega_B) + \frac{\beta_2^{01}}{2}(\Delta\omega_{I1}^2 + \Delta\omega_B^2) + \frac{\beta_3^{01}}{6}(\Delta\omega_{I1}^3 + \Delta\omega_B^3) \\ - 2\beta_0^{11} - \beta_1^{11}(\Delta\omega_{p1} + \Delta\omega_{p2}) - \frac{\beta_2^{11}}{2}(\Delta\omega_{p1}^2 + \Delta\omega_{p2}^2) - \frac{\beta_3^{11}}{6}(\Delta\omega_{p1}^3 + \Delta\omega_{p2}^3).\end{aligned} \tag{3.5}$$

The phase-mismatch equations can similarly be calculated for processes 2 and 3 that are observed in the experiments (see Sec. 3.3). For processes 2 and 3, the phase-mismatches $\Delta\beta_{(\text{proc.2})}$ and $\Delta\beta_{(\text{proc.3})}$ are written as:

$$\begin{aligned}\Delta\beta_{(\text{proc. 2})} \approx \beta_1^{01}(\Delta\omega_{I2} - \Delta\omega_B) + \frac{\beta_2^{01}}{2}(\Delta\omega_{I2}^2 - \Delta\omega_B^2) + \frac{\beta_3^{01}}{6}(\Delta\omega_{I2}^3 - \Delta\omega_B^3) \\ - \beta_1^{11}(\Delta\omega_{p1} - \Delta\omega_{p2}) - \frac{\beta_2^{11}}{2}(\Delta\omega_{p1}^2 - \Delta\omega_{p2}^2) - \frac{\beta_3^{11}}{6}(\Delta\omega_{p1}^3 - \Delta\omega_{p2}^3),\end{aligned} \tag{3.6}$$

$$\begin{aligned}\Delta\beta_{(\text{proc. 3})} \approx \beta_1^{01}(\Delta\omega_{I2} - \Delta\omega_B) + \frac{\beta_2^{01}}{2}(\Delta\omega_{I2}^2 - \Delta\omega_B^2) + \frac{\beta_3^{01}}{6}(\Delta\omega_{I2}^3 - \Delta\omega_B^3) \\ + \beta_1^{11}(\Delta\omega_{p1} - \Delta\omega_{p2}) + \frac{\beta_2^{11}}{2}(\Delta\omega_{p1}^2 - \Delta\omega_{p2}^2) + \frac{\beta_3^{11}}{6}(\Delta\omega_{p1}^3 - \Delta\omega_{p2}^3).\end{aligned} \tag{3.7}$$

Because the signs for ω_{p1} and ω_{p2} are inverted in processes 2 and 3, therefore in process 3, ω_{p1} is phase conjugate while in process 2, ω_{p3} is phase conjugate. At the perfect phase-matching condition $\Delta\beta$ should be zero for these processes. Eqs. 3.6 and 3.7 will later be used to calculate and plot the FWM efficiency for different pump and probe wavelengths. In the following, two different cases are discussed to find the FWM efficiency. In one case the wavelength of the two pumps are fixed and the wavelength of the Probe is changing (probe detuning) and in another case the wavelengths of one pump and probe are fixed and the wavelength of the second pump is changing (pump detuning).

Probe Detuning

As seen earlier in this section, $\Delta\beta_{(\text{proc.1})}$ in Eq. 3.5 depends on β_0^{01} and β_0^{11} which are the first terms in the Taylor expansion of the propagation constants of the waves involved in the process. As mentioned earlier, process 1 is not observed in

the experiments for the *same-mode pumps configuration* possibly due to its phase-matching condition dependency on the β_0^{01} and β_0^{11}, making it more sensitive to fiber birefringence. From Eqs. 3.6 and 3.7 we can calculate the FWM efficiencies for processes 2 and 3, respectively using $Sinc^2(L\kappa/2)$ or $Sinc^2(L\Delta\beta/2)$ equation. If we choose a configuration for process 2 where $\omega_{p1} = 1541$ nm, $\omega_{p2} = 1542$ nm and we choose $\omega_0 = 1550$ nm, Eq. 3.6 will take the form shown below in Eq. 3.8:

$$\begin{aligned}\Delta\beta_{(\text{proc.2})} \approx (&\beta_2^{01}\omega_{p1} - \beta_3^{01}\omega_{p1}\omega_0 + \frac{1}{2}\beta_3^{01}\omega_{p1}^2 - \beta_2^{01}\omega_{p2} + \beta_3^{01}\omega_0\omega_{p2} - \beta_3^{01}\omega_{p1}\omega_{p2} \\ &+ \frac{1}{2}\beta_3^{01}\omega_{p2}^2)\omega_B + (\frac{1}{2}\beta_3^{01}\omega_{p1} - \frac{1}{2}\beta_3^{01}\omega_{p2})\omega_B^2,\end{aligned} \tag{3.8}$$

which is a second order polynomial in terms of ω_B, resulting in two different probe frequencies that can satisfy the $\Delta\beta_{(proc.2)} = 0$ equation with only one solution in the C-band at 1557.6 nm. The FWM efficiency of process 2 is plotted in Fig. 3.2(a) as a function of probe frequency, ω_B, yielding a full width at half maximum (FWHM) of $\sim$0.06 nm. The solid line refers to the $Sinc^2(L\Delta\beta_{(proc.2)}/2)$ and the dashed line refers to the $Sinc^2(L\kappa/2)$. If we choose the same configuration for process 3 as for process 2 with pumps at 1541 nm and 1542 nm, Eq. 3.7 results in Eq. 3.9 shown below:

$$\begin{aligned}\Delta\beta_{(\text{proc.3})} \approx (&-\beta_2^{01}\omega_{p1} + \beta_3^{01}\omega_{p1}\omega_0 + \frac{1}{2}\beta_3^{01}\omega_{p1}^2 + \beta_2^{01}\omega_{p2} - \beta_3^{01}\omega_0\omega_{p2} - \beta_3^{01}\omega_{p1}\omega_{p2} \\ &+ \frac{1}{2}\beta_3^{01}\omega_{p2}^2)\omega_B + (-\frac{1}{2}\beta_3^{01}\omega_{p1} + \frac{1}{2}\beta_3^{01}\omega_{p2})\omega_B^2,\end{aligned} \tag{3.9}$$

which is a quadratic polynomial with respect to ω_B and has two solutions for the perfect phase-matching equation $\Delta\beta_{(proc.3)} = 0$ with one in the C-band at 1556.64 nm. The FWM efficiency for process 3 is plotted in Fig. 3.2(b) as a function of probe frequency, yielding a FWHM of $\sim$0.06 nm for the probe frequency detuning in the C-band. If we keep one of the pumps at 1542 nm and change the wavelength of the first pump to 1540 nm to have a pumps separation of 2 nm, perfect phase matching condition happens at 1557.69 nm for process 2 and 1555.64 nm for process 3. Similarly, for 4 nm of pump separation with the first pump at 1538 nm, process 2 will have perfect phase matching at 1557.74 nm and process 3 at 1553.65 nm. For a pumps separation of 8 nm with the first pump at 1534 nm, the perfect phase

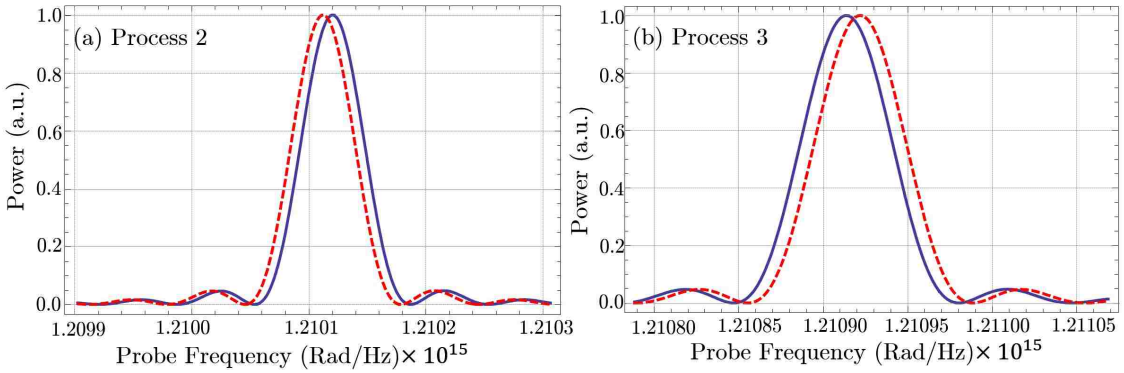

Figure 3.2: The FWM efficiency, $Sinc^2(L\kappa/2)$ (dashed line) and $Sinc^2(L\Delta\beta_{(proc.2)}/2)$ (solid line) as a function of probe frequency, ω_B, for (a) process 2 and (b) process 3, resulting in a FWHM of ∼0.06nm centered at 1557.6 nm for process 2 and a FWHM of ∼0.06nm centered at 1556.64 nm for process 3.

matching condition is satisfied at 1557.84 nm for process 2 and 1549.68 nm for process 3. For a pump separation of 32 nm with first pump at 1532 nm and the second pump at 1564 nm, process 2 and 3 will have their peak power at 1579.88 and 1547.23 nm. As the separation of the two pumps increases, the FWHM of the FWM efficiency is decreased.

Pump Detuning

If we choose a configuration for process 2 where $\omega_{p1} = 1540$ nm, $\omega_B = 1556$ nm and $\omega_0 = 1550$ nm, then Eq. 3.6 will lead to a third order polynomial equation in terms of ω_{p2} as shown below in Eq. 3.10:

$$\begin{aligned}\Delta\beta_{(\text{proc. 2})} \approx Const. + \Big[&\Big(\frac{1}{v_g^{11}} - \frac{1}{v_g^{01}}\Big) + (\beta_2^{01} - \beta_2^{11})\omega_0 + \frac{1}{2}(-\beta_3^{01} + \beta_3^{11})\omega_0^2 \\ &+ (-\beta_2^{01} + \beta_3^{01}\omega_0 + \frac{1}{2}\beta_3^{01}\omega_{p1})\omega_{p1} + (-\beta_2^{01} + \beta_3^{01}\omega_0 - \beta_3^{01}\omega_{p1} - \frac{1}{2}\beta_3^{01}\omega_B)\omega_B\Big] \\ &\times \omega_{p2} + \frac{1}{2}\big(\beta_2^{01} + \beta_2^{11} - \beta_3^{01}\omega_0 - \beta_3^{11}\omega_0 + \beta_3^{01}\omega_{p1} + \beta_3^{01}\omega_B\big)\omega_{p2}^2 \\ &+ \frac{1}{6}(\beta_3^{11} - \beta_3^{01})\omega_{p2}^3,\end{aligned} \tag{3.10}$$

which has three solutions for the perfect phase-matching condition, $\Delta\beta_{(proc.2)} = 0$, with two of them in the C-band, 1540 nm and 1540.3 nm. The corresponding FWM

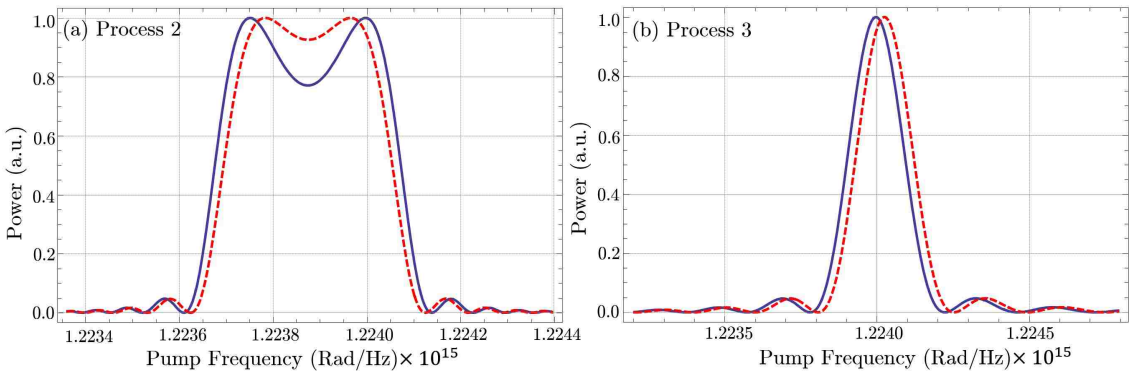

Figure 3.3: The FWM efficiency, $Sinc^2(L\kappa/2)$ (dashed line) and $Sinc^2(L\Delta\beta_{(proc.2)}/2)$ (solid line) as a function of pump frequency, ω_{p2}, for (a) process 2 and (b) process 3, yielding a FWHM of ∼0.5nm for process 2 and ∼0.2nm for process 3.

efficiency for process 2 is plotted in Fig. 3.3(a) as a function of pump frequency, ω_{p2}, yielding a FWHM of ∼0.5 nm. The solid line refers to the $Sinc^2(L\Delta\beta_{(proc.3)}/2)$ and the dashed line refers to the $Sinc^2(L\kappa/2)$ which includes the nonlinear modification to the phase-mismatch. If we choose the same configuration for process 3 as for process 2 where $\omega_{p1} = 1540$ nm, $\omega_B = 1556$ nm with $\omega_0 = 1550$ nm, then Eq. 3.7 is a cubic polynomial in terms of ω_{p2}:

$$\begin{aligned}\Delta\beta_{(\text{proc. 3})} \approx Const. + \Bigg[&- \Big(\frac{1}{v_g^{11}} - \frac{1}{v_g^{01}}\Big) + (-\beta_2^{01} + \beta_2^{11})\omega_0 + \frac{1}{2}(\beta_3^{01} - \beta_3^{11})\omega_0^2 \\ &+ (-\beta_2^{01} + \beta_3^{01}\omega_0 + \frac{1}{2}\beta_3^{01}\omega_{p1})\omega_{p1} + (\beta_2^{01} - \beta_3^{01}\omega_0 - \beta_3^{01}\omega_{p1} + \frac{1}{2}\beta_3^{01}\omega_B)\omega_B\Bigg] \\ &\times \omega_{p2} + \frac{1}{2}\big(\beta_2^{01} - \beta_2^{11} - \beta_3^{01}\omega_0 + \beta_3^{11}\omega_0 - \beta_3^{01}\omega_{p1} + \beta_3^{01}\omega_B\big)\omega_{p2}^2 \\ &+ \frac{1}{6}(\beta_3^{01} - \beta_3^{11})\omega_{p2}^3.\end{aligned} \tag{3.11}$$

From Eq. 3.11, the perfect phase-matching ($\Delta\beta = 0$) for this specific case happens at two different frequencies/wavelengths in the C-band which are 1540 nm and 1531.58 nm, as shown in Fig. 3.3(b) yielding a FWHM of ∼0.2 nm for pump (P_2) detuning at both wavelengths.

3.3 IM-FWM Bandwidth Measurement

3.3.1 Experiment Description

The pump-probe spectral configurations and the experimental setup are shown in Figs. 3.1 (a) and 3.5, respectively. The two pumps go through a 50:50 coupler and their relative polarizations are set to be co-polarized using a polarization beam splitter (PBS) and two polarization controllers (PC-1 and PC-2) as shown in Fig. 3.5. The pump beams are sent through a Waveshaper (WS) which is a programmable optical band pass filter (OBPF) to reduce the background noise and increase the extinction ratio, and the probe beam through a programmable Wavelength Selective Switch (WSS) also used as a programable and tunable filter. The WSS is programmed to tune the filter as the probe wavelength sweeps in the C-band, therefore always moving along with the probe and keeping the background noise low enough for the experiment. The spectra of one pump and the signal with and without filtering are shown in Fig. 3.4. The background noise levels are reduced by 4-6 dB for the pumps and the probe. A phase modulator connected to three Voltage-Controlled Oscillators (VCOs) at 60 MHz, 120 MHz, and 240 MHz are used to suppress stimulated Brillouin scattering (SBS) of the pump beams. The phase modulator adds new frequencies around the central frequency of each pump, resulting in spectral broadening due to a cascaded effect. This also leads to a 3 dB reduction in the maximum pump power as shown in Fig. 3.6 (a). The threshold for SBS is presented in Fig. 3.6 (b) for the LP_{11} mode group. An Erbium-doped fiber amplifier (EDFA) then amplifies the pumps power before launching them into the fiber. The fiber is a FMF supporting three spatial modes: LP_{01}, LP_{11a} and LP_{11b}. The Mode-MUX and Mode-DEMUX are free-space phase-plate-based multiplexers in this setup as shown in Fig. 2.7 [53]. The chromatic dispersions (CDs) of the LP_{01} and LP_{11} modes range from 17 to 22 ps/(nm-km) as a function of wavelength and have similar slopes in the C-band as shown in Fig. 2.4. The $1/v_g$ curve of the LP_{01} mode is shifted to longer wavelengths by $\sim$16 nm relative to that of the LP_{11} mode group. More detailed information on the fiber is provided in chapter 2 as well as references [26] and [49]. The total pump power coupled into the fiber is measured to be 21 dBm and the launched power of the probe 0 dBm. The devices were connected to a general purpose interface bus (GPIB) and a computer and were controlled through

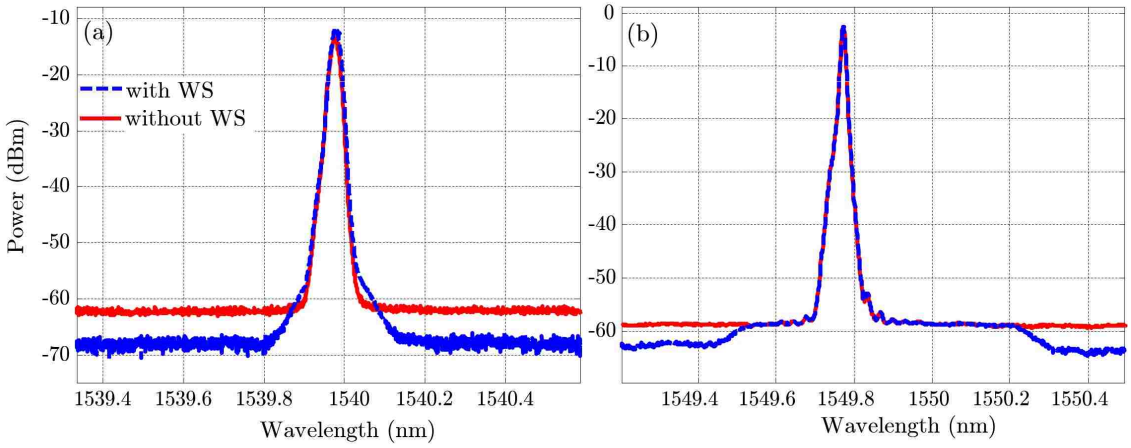

Figure 3.4: (a) Spectrum of one pump and (b) the spectrum of the probe with (blue) and without (red) filtering using Waveshaper (WS) and Wavelength Selective Switch (WSS), respectively.

a MATLAB program which automatized the data acquisition for the experiment. The IM-FWM effect is observed in the fiber when the two pumps with parallel polarizations (co-polarized) are coupled into the LP_{11} mode and the probe is coupled into the LP_{01} mode. Figure 3.7 shows the output spectra from the LP_{01} port of the Mode-DEMUX, measured using an OSA for four different pump separations of 1 nm, 2 nm, 4 nm, and 8 nm. Figure 3.8 shows the spectra for pump separations of 16 nm and 32 nm. In all cases, the pumps are launched into the LP_{11} mode group of the fiber and the pump peaks observed in the LP_{01} output port of the Mode-DEMUX are leakage due to crosstalk between the two modes of the fiber. Processes 2 and 3 are observed simultaneously in the spectrum of Fig. 3.7, but only one process is observed in Fig. 3.8 due to the high background noise outside of the C-band. Process 1 was not observed, presumably because its phase-matching condition in Eq. 3.5 depends on the zeroth order propagation constant, β_0, of the Taylor expansion which makes it more sensitive to fluctuations due to fiber imperfections.

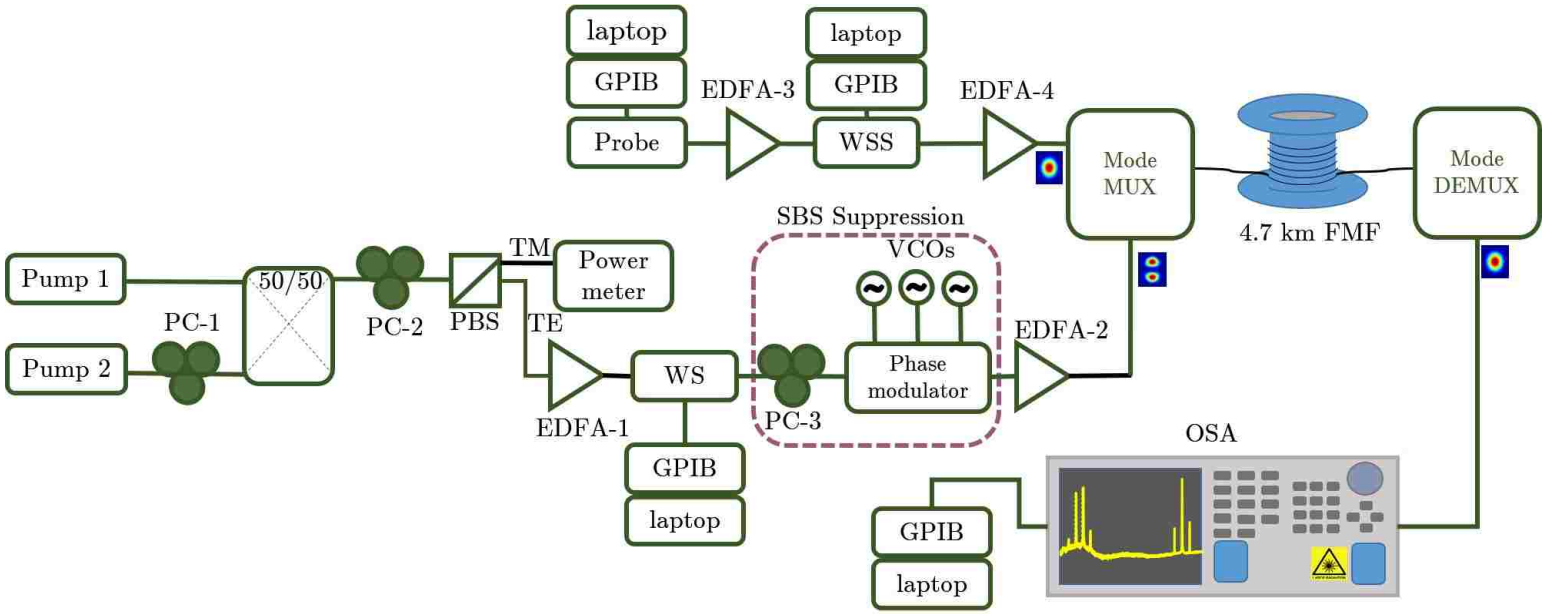

Figure 3.5: Experimental setup used to observe IM-FWM in a graded index FMF supporting the LP_{01} and LP_{11} modes.

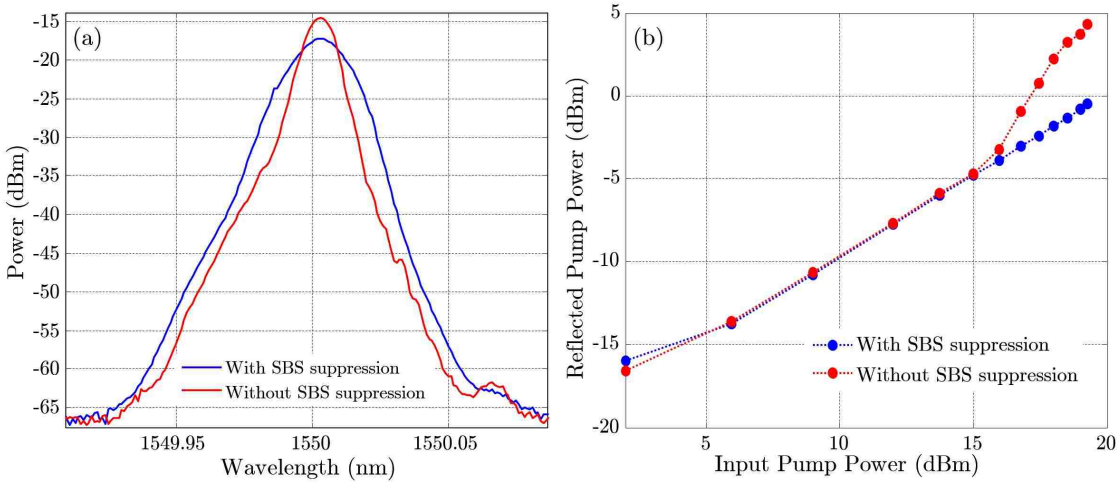

Figure 3.6: (a) The spectrum of a pump with and without SBS suppression and (b) the power of the back-scattered light for the LP_{11} modes in the FMF versus the input power with (blue) and without (red) SBS suppression.

3.3.2 Probe Detuning

Figures 3.9(a) and 3.9(b) show the results of the full bandwidth measurements for processes 2 and 3 as a function of probe wavelength. The two LP_{11} pumps have fixed wavelengths of 1541 nm and 1542 nm respectively (1 nm separation). The red line shows the $Sinc^2(L\Delta\beta/2)$ fit function of the experimental data that is plotted with dots. The probe wavelength was swept over ∼12 nm around the optimal phase-matched IM-FWM conditions ($\Delta\beta = 0$) for both processes. The pumps interact equally with the probe, maintaining near-phase-matching conditions over a large bandwidth for these processes. As expected from the respective modal dispersions, the maximum idler power is obtained when the average wavelength of the two LP_{11} pumps is ∼16 nm shorter than the average wavelength of the LP_{01} probe and generated idler [26]. As it is shown in Figs. 3.2(a) and 3.2(b), the perfect phase-matching condition is calculated to happen at probe wavelength of 1557.6 nm for process 2 and 1556.64 nm for process 3 and both efficiencies are expected to have a FWHM of 0.06 nm. However, in the experimental data the $Sinc^2(L\Delta\beta/2)$ fits have a FWHM of ∼1.8 nm for both processes. In other measurements, the pump wavelengths are fixed at 2 nm, 4 nm, and 32 nm apart, and the probe wavelength is swept about the optimal FWM condition. The FWM efficiencies for 2 nm pumps

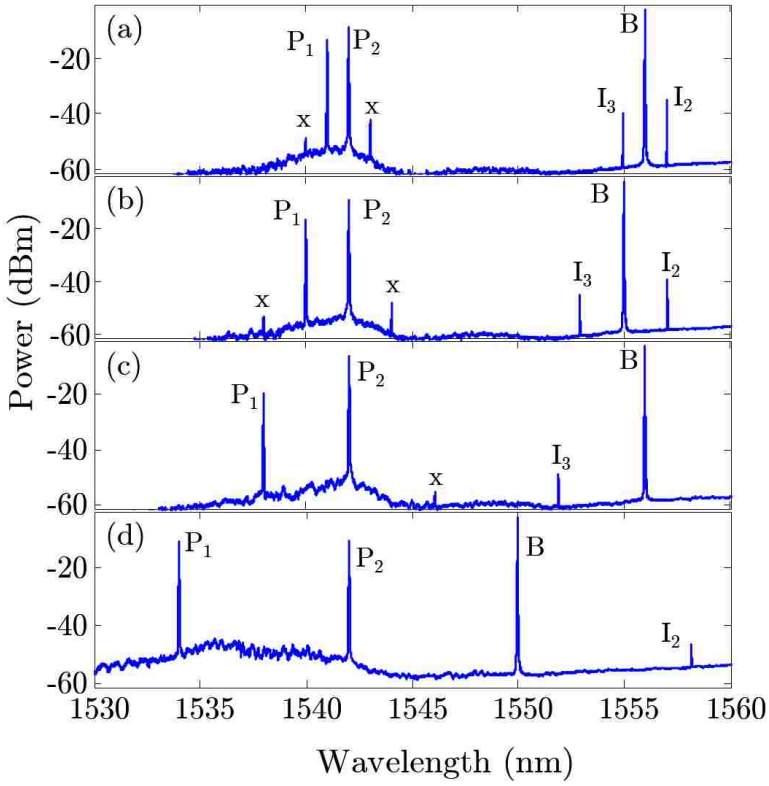

Figure 3.7: Power spectra of the fiber output from the LP_{01} port of Mode-DEMUX, with the second pump (P_2) fixed at 1542 nm wavelength and for a pump separation of (a) 1 nm with the first pump (P_1) at 1541 nm; (b) 2 nm with P_1 at 1540 nm; (c) 4 nm with P_1 at 1538 nm, and (d) 8 nm with P_1 at 1534 nm. Peaks marked as "x" are the idlers generated due to intra-modal FWM effect between two pumps in the same mode (LP_{11} mode group. B designated the probe and I_2 and I_3 designate processes 2 and 3, respectively.

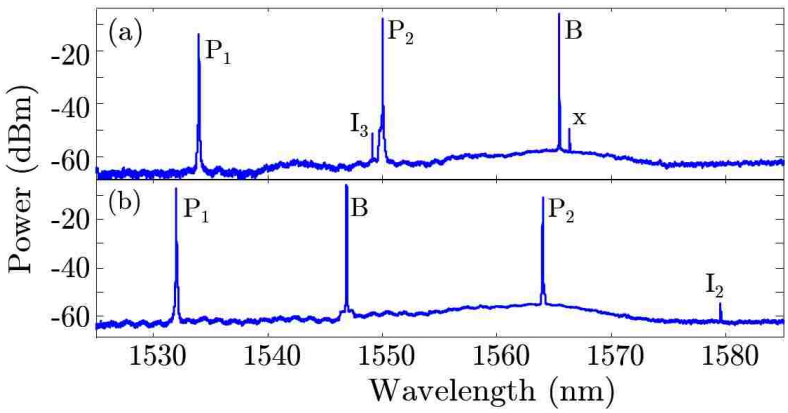

Figure 3.8: Power spectra of the fiber output from the LP_{01} port of Mode-DEMUX for a pump separation of (a) 16 nm with the first pump (P_1) at 1534 nm and the second pump (P_2) at 1550 nm; (b) 32 nm with P_1 at 1532 nm and P_2 at 1564 nm. Peaks marked as "x" are the idlers generated due to intra-modal FWM effect between two pumps in the same mode. B designated the probe and I_2 and I_3 designate processes 2 and 3, respectively.

separation are shown in Fig. 3.10, for 4 nm pumps separation in Fig. 3.11 and for 32 nm pumps separation in Fig. 3.12. The FWM efficiency bandwidth is ∼1.8 nm for all three pumps separations. The maximum observed power of the idlers is reduced by about 20 dB when increasing the wavelength separation of the two pumps from 1 nm to 32 nm. The reason for equal bandwidth for both processes is that the idlers generated from the two processes shift in the same direction and by the same amount when sweeping the probe wavelength. For processes 2 and 3 with the two pumps fixed at a specific frequency/wavelenth, a small detuning of the probe to $\omega_B - \delta\omega$ will change the idlers to $\omega_{I2} - \delta\omega$ and $\omega_{I3} - \delta\omega$, respectively. The two pumps, remaining at fixed wavelengths, interact equally with the probe. The relative sign of the phase contributions of the two pumps is therefore central to the FWM process. Thus phase-matching is maintained over an almost equal bandwidth for both processes as in the experimental results of Fig. 3.9, 3.10 and 3.11. The difference between the theoretical and experimental efficiency bandwidth of the two processes may be explained by the dispersion of the fiber. Measurements of dispersion on several segments coming from the same fiber draw indicates that the wavelength separation where waves of different spatial modes have the same

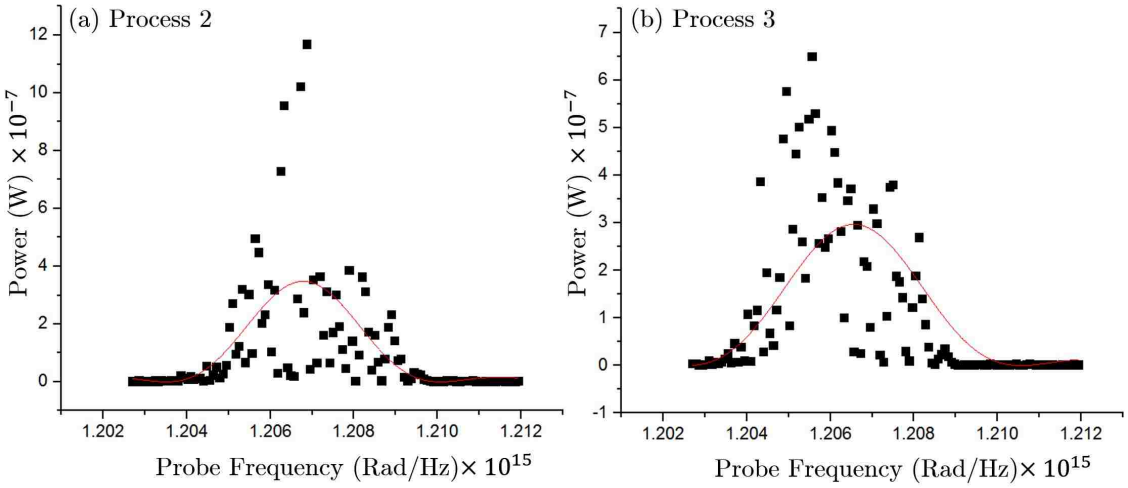

Figure 3.9: The full bandwidth measurement for processes (a) 2 and (b) 3, when the pumps separation is 1 nm (with pump wavelengths of 1541 and 1542 nm).

dispersion can vary by many nanometers. This suggests that such variations are present within each fiber segment and that the dispersion measurements are an average over the fiber length. Also, it may indicate that the Inter-modal effects are not as simple as intra-modal effects and there require more work to identify the possible effects that cause larger bandwidths for IM-FWM effects in FMFs.

In all these measurements, we observe strong fluctuations of the idler powers for both processes as a function of probe wavelength. This appears as "noise" in Fig. 3.9, 3.10, 3.11 and 3.12. However, these large and relatively regular fluctuations are not observed when the three waves (two pumps and one probe) are all in the LP_{01} mode and co-polarized as discussed in Sec. 3.4.1.

3.3.3 Pump Detuning

When the probe (B) and one pump (P_1) are fixed at 1556 nm and 1540 nm, respectively, and the second pump (P_2) is swept from 1530 nm to 1550 nm, the observed processes display a bandwidth of $sim1.2$ nm for process 2 and $sim0.6$ nm for process 3, as shown in Figs. 3.13(a) and 3.13(b). The solid red lines are the $Sinc^2(L\Delta\beta/2)$ fit function of the experimental data that is plotted with dots. The theoretical values for the FWHM of the FWM efficiency for these processes as shown in Fig.

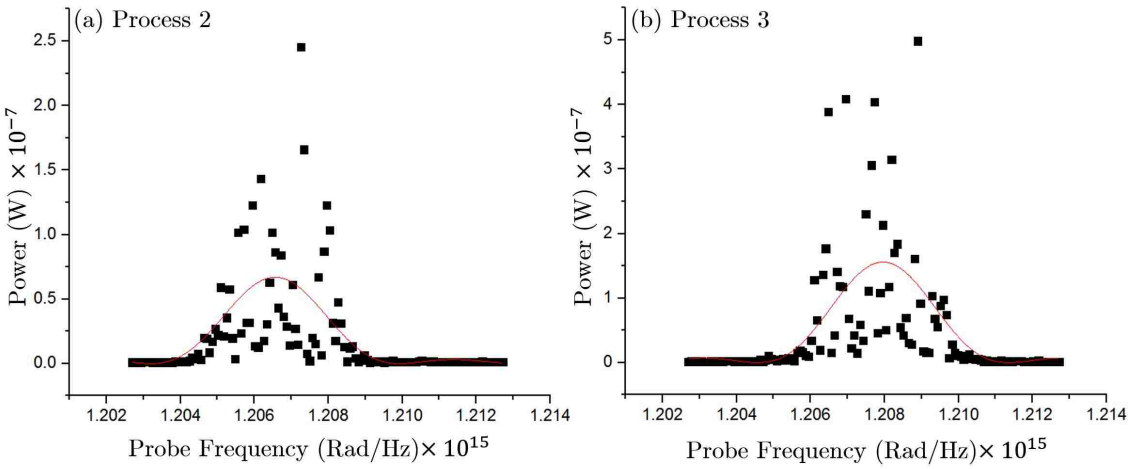

Figure 3.10: The full bandwidth measurement for processes (a) 2 and (b) 3, when the pumps separation is 1 nm (with pump wavelengths of 1540 and 1542 nm).

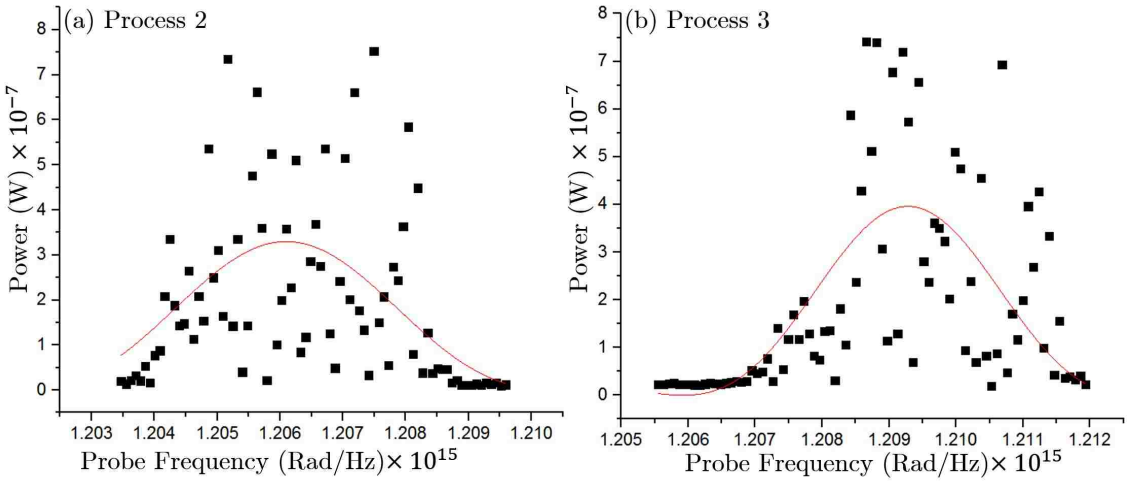

Figure 3.11: The full bandwidth measurement for processes (a) 2 and (b) 3, when the pumps separation is 1 nm (with pump wavelengths of 1538 and 1542 nm).

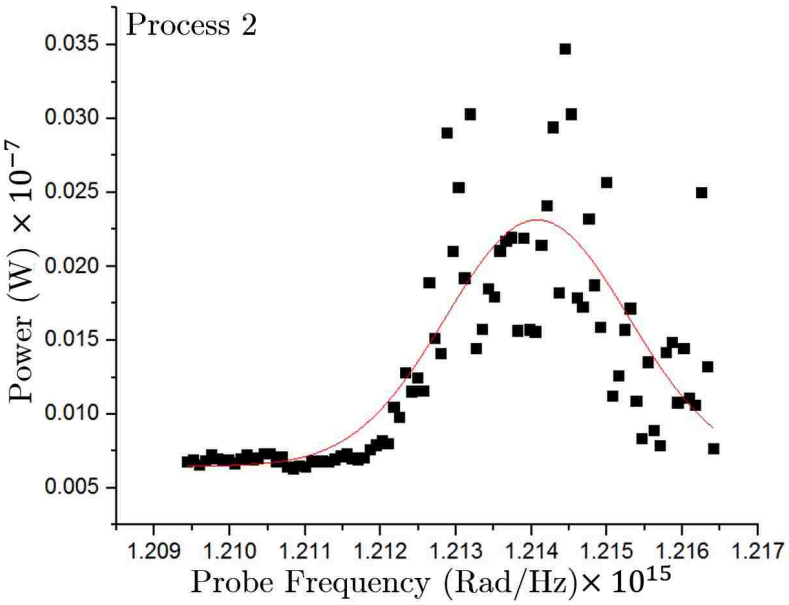

Figure 3.12: The full bandwidth measurement for process 2 when the pumps separation is 32 nm.

3.3(a) and 3.3(b) are 0.5 nm and 0.2 nm for processes 2 and 3, respectively. In addition to the detailed Taylor expansion of the phase-mismatch, the difference of the bandwidth of the two processes can be explained by how the two processes are changing in the frequency domain. When the pump frequency is varied to $\omega_{P2} - \delta\omega$, the idler frequency shifts as $\omega_{I2} - \delta\omega$ for process 2 and to $\omega_{I3} + \delta\omega$, for process 3. Therefore, the phase contributions tends to cancel out for process 2, which is therefore maintaining phase-matching for a larger frequency detuning than for process 3. In conclusion, we have shown that the efficiency bandwidths for these processes can be different due to different phase-matching relations for different conditions.

3.4 IM-FWM Fluctuations

This section is based on the conference paper [59] presented at ECOC2015. In this section, we report high-resolution measurements of IM-FWM for the *same-mode pumps configuration* as before, in which both pumps are coupled into one of the LP_{11} higher-order modes while the probe is launched into the fundamental LP_{01} mode. Strong variations of the idler power are observed when tuning the probe wavelength and for various relative polarizations of the pumps and signal.

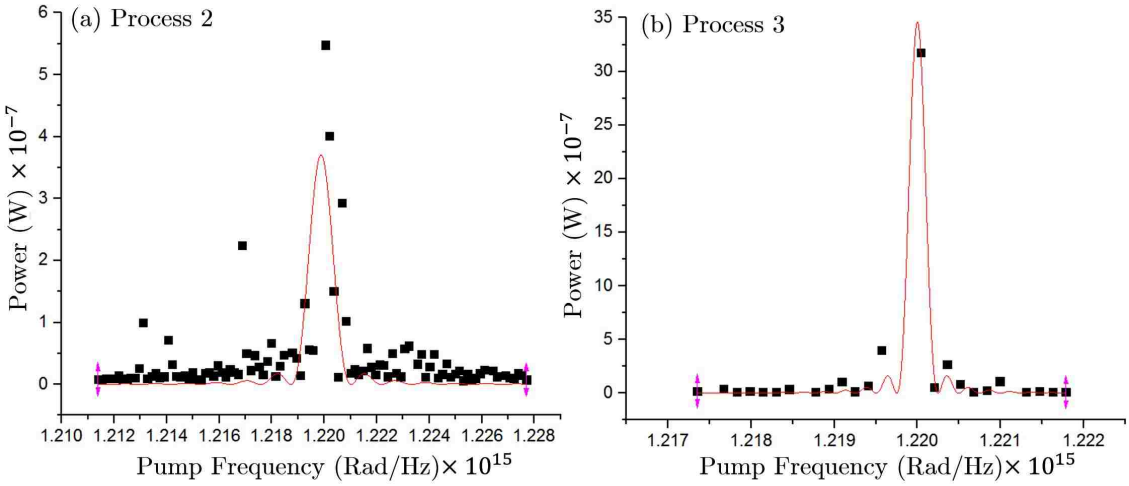

Figure 3.13: Powers of (a) process 2 and (b) process 3 when pump P_1 is fixed at 1540 nm, the probe fixed near 1556 nm and pump P_2 is swept about 20 nm around 1540 nm.

These large variations are found to persist in time but do not occur when all waves are injected in the fundamental mode LP_{01}. We study the stability of the idler amplitude for various experimental conditions and compare with intra-modal FWM in the LP_{01} mode. The results are compared with the results of amplitude and phase frequency-resolved measurements obtained using a swept-wavelength interferometry technique [2] presented in Sec. 2.5, which help provide an understanding of the observed fluctuations in IM-FWM. Possible implications for future SDM systems are discussed.

3.4.1 Observation of the Intramodal-FWM

In order to understand the behaviour of the FMF when used as a single mode fiber (SMF), we first couple both pumps and the probe into the LP_{01} mode of the fiber, and measure intra-modal FWM. The experimental setup for the FWM experiment is shown below in Fig. 3.14. Two high power continuous wave (CW) pumps and a low power CW probe are coupled into the same mode after they all are combined first using two couplers, a 50:50 coupler to couple the two pumps together and then a 10:90 coupler to couple the pumps (90%) with the probe (10%). The total power of the pumps is 22 dBm and the power of the probe is 6 dBm. As mentioned

before, FWM is a polarization dependent effect. The power of the generated new frequencies depends on the relative polarizations of the different waves and if all parallel, the maximum idler power is expected. Therefore, using the polarization beam splitter (PBS), the polarizations of the two pumps and probe are set to be parallel to each other in order to maximize the FWM nonlinear effect. The SBS suppression raises the SBS power threshold for the LP_{01} mode as well as for the LP_{11} modes. The three coupled waves are then launched into the fiber using the LP_{01} port of the mode multiplexer. To measure the bandwidth of the generated idlers (process 2 and 3), the wavelengths of the two pumps are fixed at 1550 nm and 1551 nm, and the probe is swept over a wide range of wavelengths.

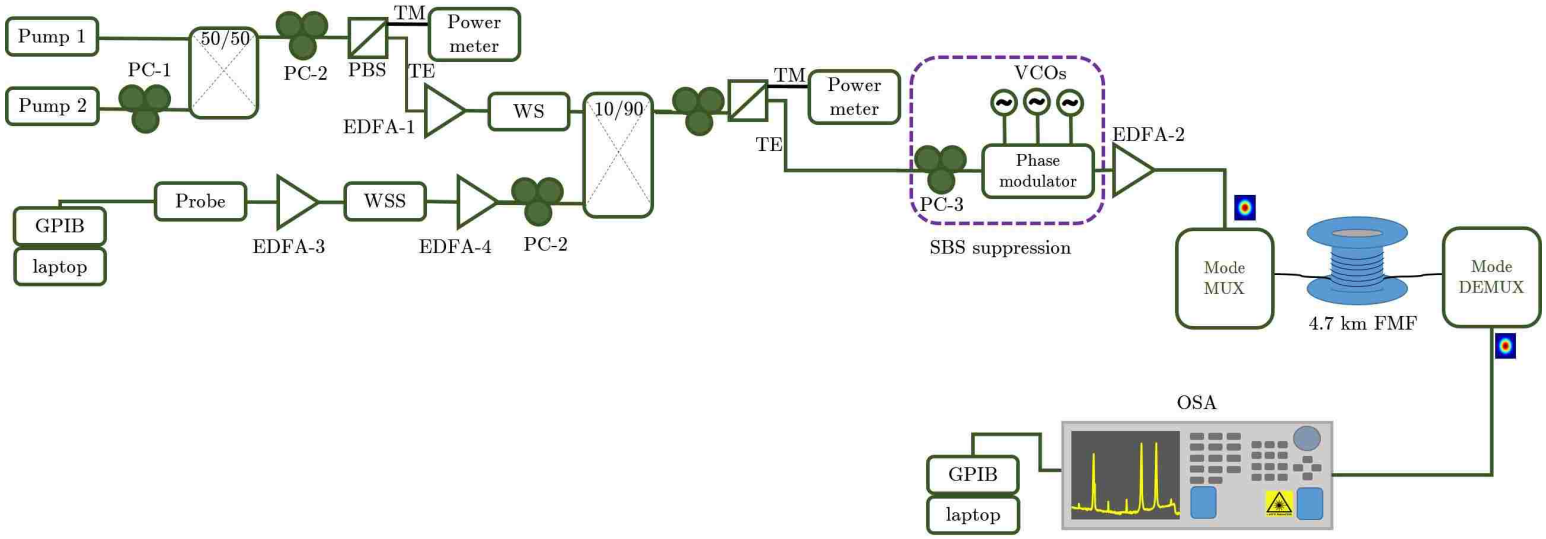

Figure 3.14: Experimental setup for measuring the intera-modal FWM in the FMF.

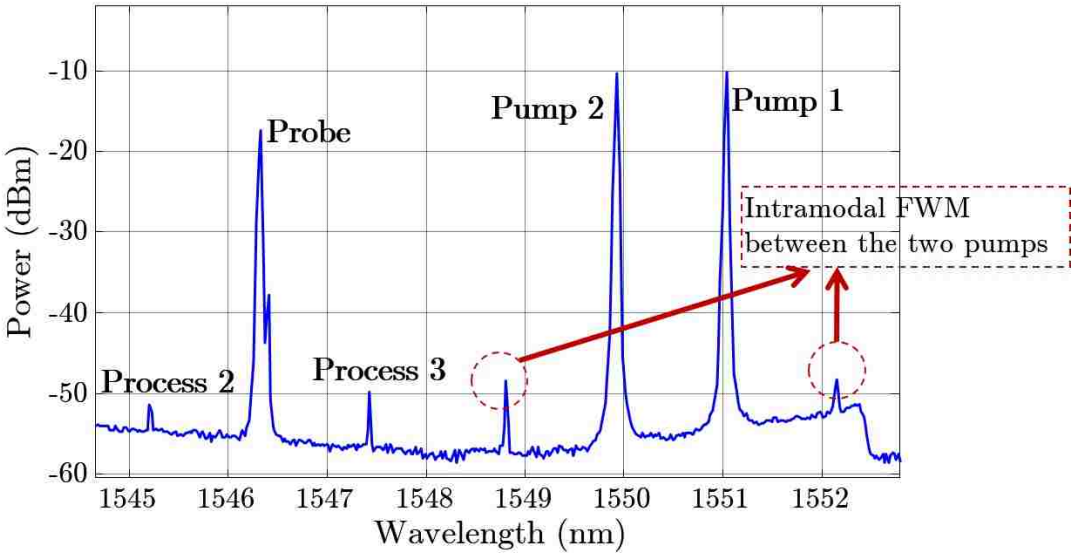

Figure 3.15: The spectrum of the LP_{01} port of the Mode-DEMUX for the probe at 1546.4 nm. The small peak next to the probe corresponds to the wavelength generated through SBS process because of the high power probe.

Fig. 3.15 shows the spectrum of the LP_{01} port of the Mode-DEMUX for the probe at 1546.4 nm. Processes 2 and 3 give rise to very small peaks over the background noise. Two peaks are also observed next to each pump, which are due to the FWM effect between the two pumps. Figs. 3.16 and 3.17 show the bandwidth of the processes 2 and 3 for a probe sweep from 1541 nm to 1549 nm.

3.4.2 High-Resolution Measurements of IM-FWM

In a second experiment, a more detailed measurement of IM-FWM efficiency was performed with the two co-polarized LP_{11} pump wavelengths fixed at 1540 nm and 1541 nm and the independently polarized probe, swept from 1555.15 nm to 1556.15 nm in 0.01 nm steps. This wavelength range was selected so as to achieve near-phase-matching conditions. First, we notice strong variations in the idler power with wavelength for both processes. Wavelength fluctuations as large as 15 dB are observed for a probe detuning as small as $\lesssim$0.1 nm. To determine the temporal variations of the idler powers, we performed several measurements over time. Figure 3.18(a) shows the different frequency patterns observed for process 2,

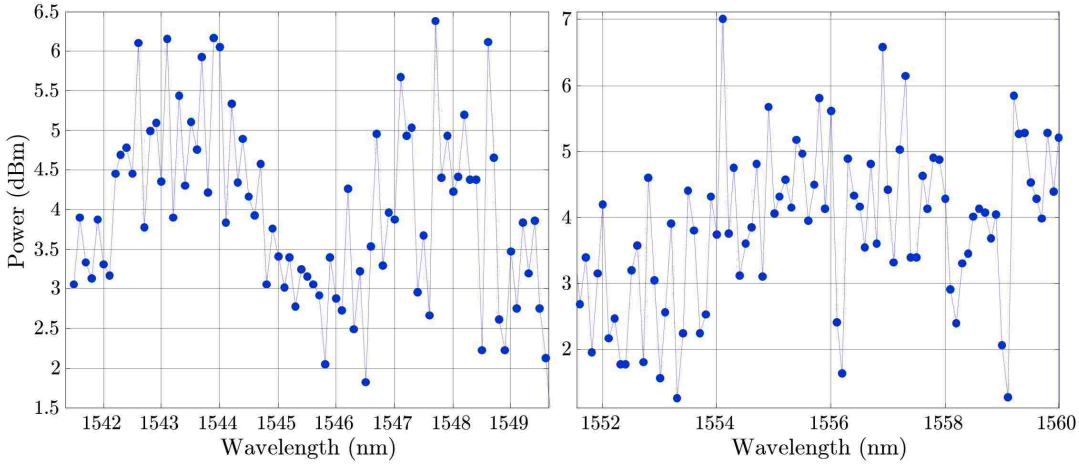

Figure 3.16: The bandwidth of the process 2 for a probe sweep from 1541 nm to 1550 nm.

and Fig. 3.18(b) for process 3. During these measurements, we avoided disturbing the FMF. The second measurement was performed 20 minutes after the first measurement and the third one much later (a few hours). As seen in Figs. 3.18(a) and 3.18(b), the wavelength patterns of the idler are highly correlated between the first and second measurements for both processes. The third measurement shows a few differences with the first two measurements but the overall pattern has not changed significantly. Additional measurements (not shown) performed after moving the FMF or heating it (by placing a soldering iron next to the fiber) changed the frequency pattern significantly but remained regular as seen in the high-resolution sweep of the probe. To verify that our experimental apparatus allowed reliable measurements of the wavelength dependence, we injected all three waves in the LP_{01} mode to observe intra-modal FWM. The fluctuations of the idler were dramatically reduced to $\sim$2 dB. This shows that IM-FWM processes result in a substantially different behavior than that intra-modal FWM processes in real telecommunication-length SDM fibers. This high-resolution measurement was repeated several times and the same fluctuations were observed to persist for several tens of minutes if the experimental setup was left undisturbed. However, touching or heating the fiber completely changed the pattern observed in Fig. 3.18, which is known to occur in randomly birefringent fibers.

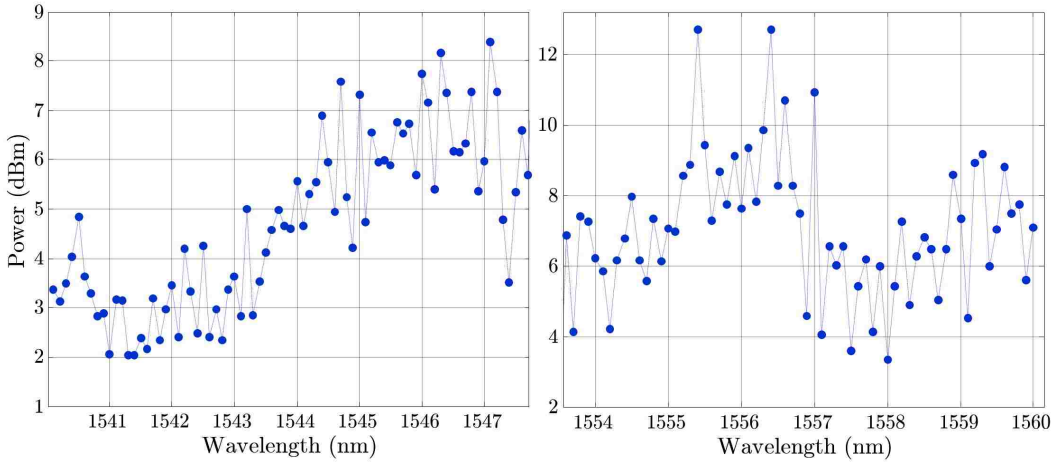

Figure 3.17: The bandwidth of the process 3 for a probe sweep from 1541 nm to 1550 nm.

In a separate experiment designed to characterize the effect of polarization, IM-FWM was measured in the same fiber but with a polarization scrambler added right after EDFA-2 in the pump path shown in Fig. 3.5 to scramble the polarization of the pumps. The wavelength of the probe was again swept over the same 1 nm interval in 0.01 nm increments. The IM-FWM spectra for the two cases, scrambled versus unscrambled polarizations, are shown in Fig. 3.19. Scrambling the polarization of the two pumps is seen to reduce the fluctuations in the idler power for both processes 2 and 3. This is an indication that polarization plays an important role in the generation of the high noise observed previously in Figs. 3.9, 3.10, 3.11 and 3.12. However, adding a polarization scrambler into the probe path did not reduce the fluctuations in the idler power in Fig. 3.20 when the LP_{01} probe wavelength was swept over 1 nm in 0.01 nm increments. This is understandable since there is little or no correlation between the polarization evolution of the pumps and the signal in the experiment.

3.5 Conclusion

In conclusion, we have performed detailed measurements of the wavelength and polarization dependence of IM-FWM in a 6 mode FMF. The FWM efficiency has been

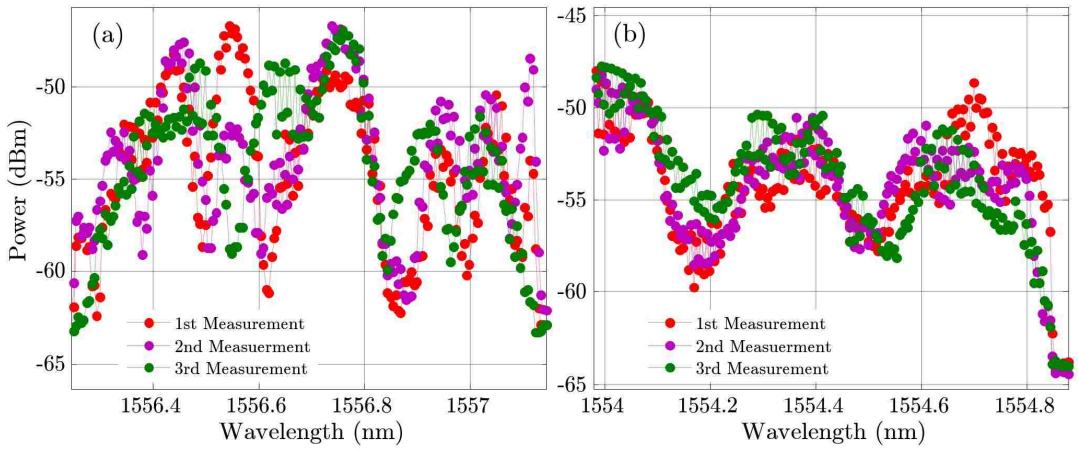

Figure 3.18: Idler amplitudes when the probe is tuned from 1555.15 nm to 1556.15 nm by steps of 0.01 nm (101 measurements superposed) for (a) process 2 and (b) process 3 for three sets of measurements separated by 20 minutes and a few hours.

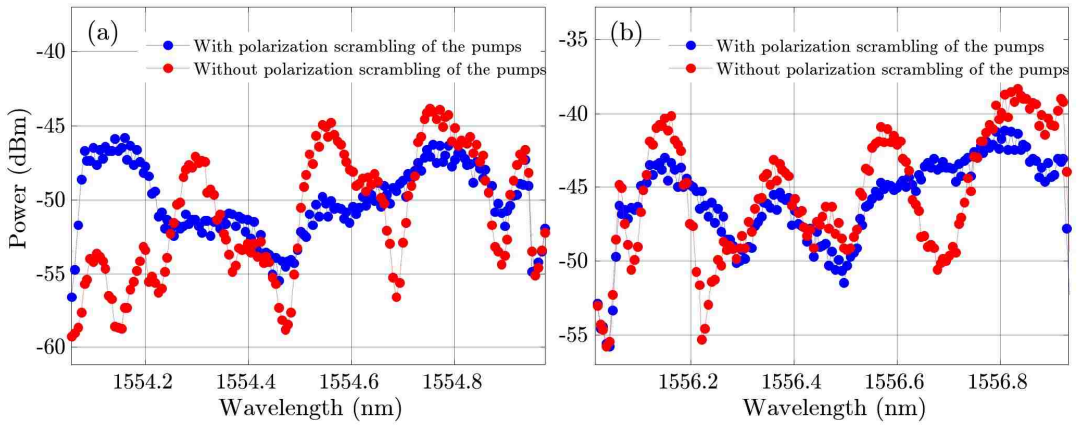

Figure 3.19: (a) Probe and the two idlers generated by processes 2 and 3 when the probe is tuned from 1555.15 nm to 1556.15 nm by steps of 0.01 nm (101 measurements superposed) with (blue) and without (red) polarization scrambling of the pumps.

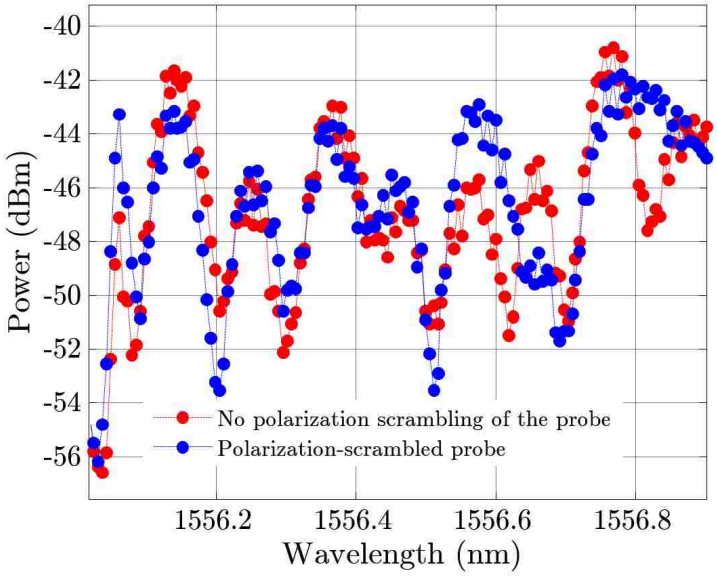

Figure 3.20: Idlers generated by process 2 when probe is tuned from 1555.15 nm to 1556.15 nm by steps of 0.01 nm with (blue) and without (red) polarization scrambling of the probe.

measured for different wavelength separations of the pumps, 1 nm, 2 nm, 4 nm, and 8 nm. A strong wavelength dependence of the idler powers is observed in both cases. To understand the origin of the power fluctuations, the linear behavior of the FMF as well as the effect of the relative polarization of pumps and probe have been studied. The IM-FWM wavelength pattern observed is found to be relatively stable and lasting several minutes if the fiber is left undisturbed, but it changes dramatically with small mechanical or thermal disturbances. Of particular significance, the IM-FWM is shown to be strongly dependent on the relative polarization of the pumps in the LP_{11} mode group. This is demonstrated by the reduced noise observed in IM-FWM efficiency upon scrambling the polarization of the pumps. However, scrambling the polarization of the LP_{01} probe does not affect the idler powers. This is further supported by the observation of the absence of such noise in intra-modal FWM observed in the same fiber in LP_{01} mode. These fluctuations are the result of the beating between the real modes of the fiber, when LP_{11} modes are launched into the fiber a superposition of real modes of the fiber including TE_{01}, TM_{01}, and HE_{21} which are non-degenerate is generated. The beating between these real modes of the fiber and the modal birefringence due to fiber imperfections are

the origins of the fluctuations observed in IM-FWM.

Chapter 4

Intermodal Distributed Raman Amplification in Few-Mode Fibers

4.1 Introduction

This chapter and the subsequent Appendix A are based on the conference paper and its subsequent Journal paper [60] and [61]. Raman scattering was first observed in [62], stimulated Raman scattering (SRS) was first demonstrated in [63], and since then the SRS effect has been extensively studied in optical waveguide and fibers [9, 64, 65, 66, 67]. In silica fibers, Raman scattering can be stimulated by having a pump and a signal in the fiber at the appropriate wavelengths. Maximum gain is observed when the signal is at an approximately 90 nm longer wavelength than the pump [8, 45]. Therefore, pump and signal are coupled to each other through the Raman process and the signal will be amplified by the Raman pump. Note that SRS is a polarization dependent effect and the Raman gain depends on the relative polarization between the pump and the signal. Raman amplification in FMFs has been experimentally demonstrated in a backward pumping configuration with an unpolarized pump, mostly to overcome the loss of the free-space phase-plate-based mode multiplexers [14]. The theory of Raman amplification in FMFs is developed in [13] and [46], which predicts that, for both step-index and graded-index FMFs with 3 spatial modes, the same modal gain for all the modes could be achieved if the pump was injected into the higher-order mode, the LP_{11a} and LP_{11b} modes in the present case. The LP_{11} modes offer two degenerate spatial modes, each having two

polarization states, in which to inject the Raman pumps. Because the LP_{11} modes are degenerate, perturbation of the index profile is expected to cause a strong linear coupling between them, or more precisely, between the underlying vector modes which are TE_{01}, TM_{01}, and the degenerate HE_{21} modes. The superposition of the real modes that generated the LP_{01} and LP_{11} modes are shown in Fig. 2.1.

In this chapter and the subsequent Appendix A we provide the first experimental demonstration of distributed Raman amplification in FMFs supporting 3 spatial modes, LP_{01}, LP_{11a}, and LP_{11b}, with more than 0 dB net gain for forward, backward and bi-directional pumping schemes, using low-loss (less than 2 dB) mode-selective photonic lanterns (MS-PLs) as mode multiplexers [68, 69, 70]. These MS-PLs have replaced the free-space Mode-MUX and Mode-DEMUX used in the FWM experiments in Chapter 3. They are fiber concertized at one end and spliced to the FMF at the other end. 0 dB net gain corresponds to absolute gain that exactly compensates for the loss of the fiber, so the fiber becomes "transparent". Modal gain equalization is obtained by selectively coupling the Raman pump lasers into the LP_{11} modes of the FMF [13, 46]. We demonstrate an absolute gain of 20 dB for the LP_{01}, LP_{11a}, and LP_{11b} modes, for a pump power of 2 W and a differential mode-dependent gain (DMDG) of 1.5-2 dB. We also perform optical transmission over 1050 km in a recirculating loop made of a 70-km fiber span made by splicing multiple fiber segments to compensate the differential-group-delay (DGD). A transmission experiment that is explained in Appendix A is then performed where We achieve a net gain of 0 dB for a combined wavelength-division and spatial-division multiplexed (WDM/SDM) signal with 60 wavelengths spaced 33.33 GHz apart, and 6 spatial and polarization modes modulated at 30 Gbaud with quaternary-phase-shift keying (QPSK) signals. The total transmitted capacity is 18 Tb/s and the spectral efficiency (SE) which is the information rate transmitted over a given bandwidth is 9 bit/s/Hz.

4.2 Raman Amplification Experiment

The 70-km-long graded-index FMF used in our experiments had effective areas of 59.6 μm^2 for the LP_{01} mode and 120.2 μm^2 for the LP_{11} modes as shown in Tab. 2.1 and 2.2. The absorption coefficients were measured using the optical time-domain reflectometer (OTDR) shown in Fig. 4.1. We obtained losses of 0.238 dB/km and

0.224 dB/km at a wavelength of 1550 nm for the LP_{01} and LP_{11} modes respectively, and 0.317 dB/km at a wavelength of 1455 nm for the LP_{11} modes. It results in a span loss of ∼16 dB at the signal wavelength in the C-band. The 70 km DGD-compensated fiber span was built by splicing four fiber spools with lengths of 12.5 km, 25 km, 12.5 km and 20 km and DGDs of -2 ns, 1.64 ns, -1.17 ns and 1.52 ns, respectively. It resulted in a total DGD of <200 ps, which was verified with a time-of-flight measurement using a 100 ps test pulse. The transmitted 100 ps pulse through this fiber spool and MS-PLs is shown in Fig. 4.2. It also shows the coupling between the LP_{11a} and LP_{11b} modes. When LP_{01} is launched into the fiber, the LP_{11} modes are not excited and when LP_{11} modes are launched into the fiber using the MS-PLs, LP_{01} mode is not excited. Two MS-PLs were used as mode multiplexers and directly spliced to the FMF, resulting in a small coupling loss of 1 dB for the LP_{01} mode and 1.7 dB for each one of the LP_{11} modes. The photonic lantern-based mode multiplexers were fabricated by tapering three dissimilar SMFs, one with a slightly different core diameter than the other two to ensure mode-selectivity, inside a low-refractive-index capillary that acted as the cladding of the adiabatically tapered lantern [69]. The light coupled into the SMF with larger core diameter, SMF-1 in Fig. 4.4, at the input of the MS-PL converts into the LP_{01} and the light coupled into each one of the two similar SMFs, SMF-2 and SMF-3 in Fig. 4.4, converts to LP_{11a} or LP_{11b} modes selectively. Therefore, each SMF at the MS-PL corresponds to generating one of the three spatial modes before coupling into the fiber. This can be understood by looking at the modal analysis of a similar three SMF multiplexer (or photonics lantern) using the coupled mode theory as in a three core MCF with one dissimilar core. During the tapering process the cores get closer to each other along the fiber and therefore the modes convert along the fiber [68]. Figure 4.3 shows the simulation of the mode conversion during the tapering process of the three SMF in a capillary using COMSOL Multiphysics software. The dissimilar SMF ensures the mode selectivity of the photonic lantern and Fig. 4.4 shows the captured mode profiles of the lanterns used in our experimental setup with an infrared (IR) camera.

Two Raman pumps were available for the experiment: the first pump had a central wavelength at 1545 nm, was unpolarized and had a maximum output power of 33 dBm. The second pump had a central wavelength at 1545.5 nm, was polarized

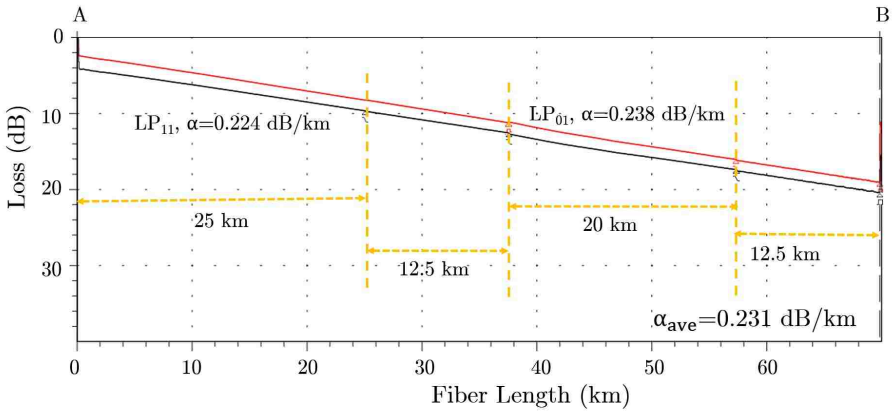

Figure 4.1: The OTDR trace of the 70 km FMF spool for both LP_{01} and LP_{11} modes at 1550 nm.

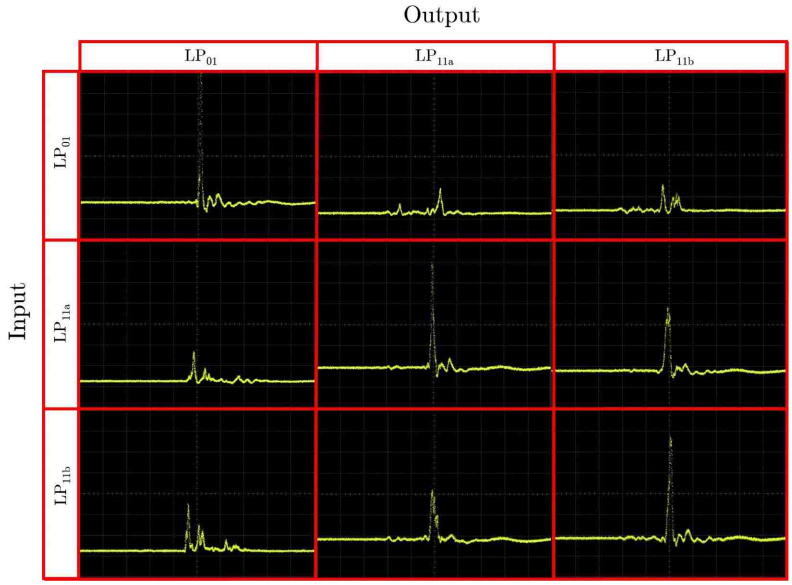

Figure 4.2: The transmitted 100 ps pulse through 70 km FMF spool and the MS-PLs for different input/output ports of the photonic lantern-based Mode-MUX and Mode-DEMUX.

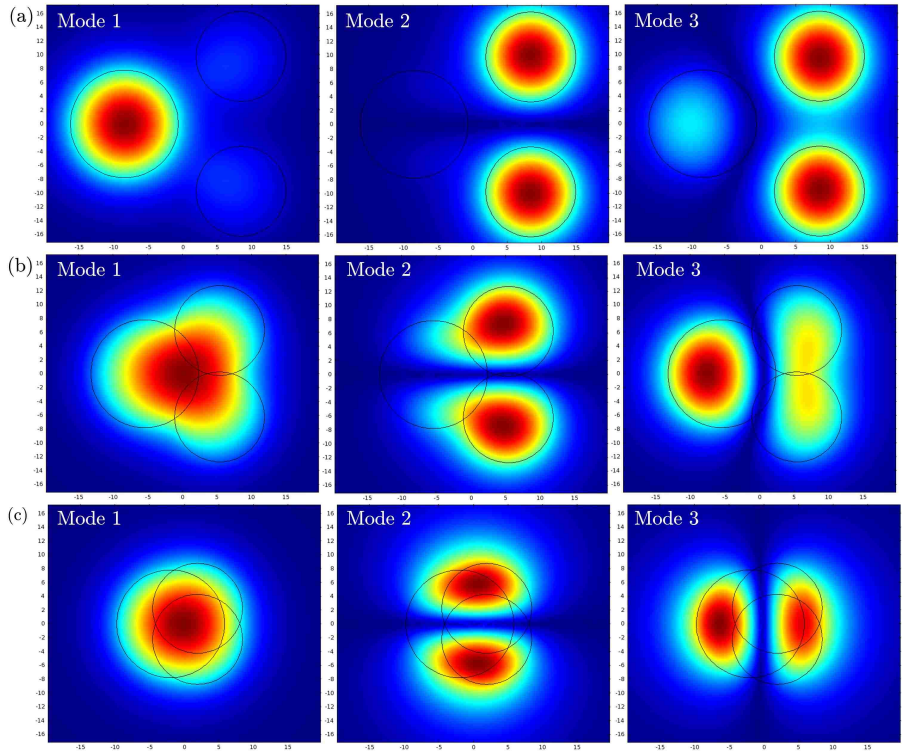

Figure 4.3: Modal analysis of a tapered three core multiplexer which includes three SMF in a capillary. There are three spatial modes (or supermodes) for this configuration, these modes are the solutions to the wave equation. This modal analysis is similar to the modal analysis of a three-core MCF that has three spatial modes. Each row represents the mode profile of the three fiber system for different distances or pitches between the fibers (or the cores in a MCF). The pitch is 19.5 μm in (a), 10.5 μm in (b) and 6.5 μm in (c). It shows the mode conversion along a tapered three fiber system.

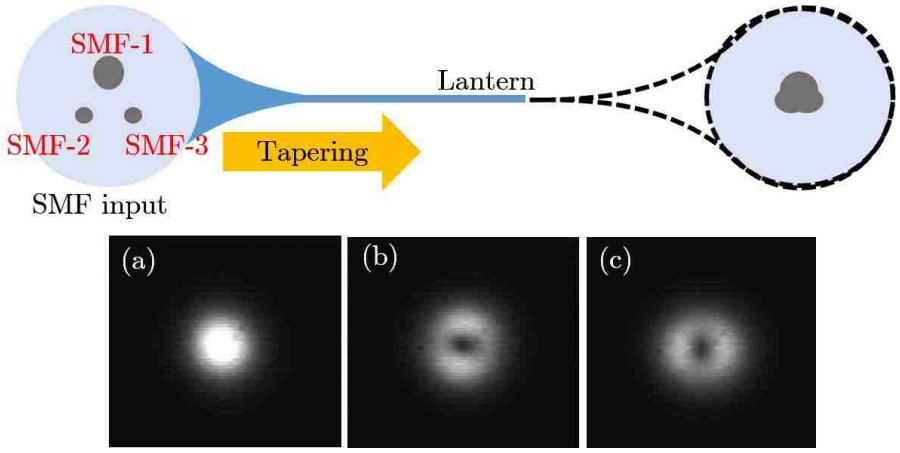

Figure 4.4: Output mode profiles of a three core/mode photonic lantern for inputs in (a) SMF-1 with a larger core diameter than SMF-1 and SMF-2 (b) SMF-2 and (c) SMF-3.

and had a maximum output power of 37 dBm. Both pumps had a wavelength of 1455 nm providing gain in the 1545 nm to 1566 nm wavelength range of the C-band. A wider wavelength range and flat spectral gain can be obtained by combining multiple pumps at different pump wavelengths. In order to reduce the polarization dependence of the signal gain, the polarized pump is used in the backward direction in the bi-directional pumping scheme shown in Fig. 4.5. As discussed in Sec. 1.2.2, in order to achieve equal amplification for all the modes in a Raman fiber amplifier [13] providing 3 spatial modes, the pumps are launched into the LP_{11} modes. In Eq. 1.47, it is shown that the signal depends on the overlap integral f_{ij} of the signal and pump modes. Since the FMF under test has three spatial modes, the signal gain in LP_{01} and LP_{11} modes will be equal if the pumps are coupled into LP_{11} modes only. This can be understood from the overlap integrals of Tab. 2.2 that shows almost equal values for pumps in LP_{11} modes and signal in LP_{01} and LP_{11} modes. As shown in the experimental setup shown in Fig. 4.5, using 50:50 couplers, the Raman pump power is split between two arms, each coupled to the corresponding LP_{11} mode of the MS-PLs through a dichroic combiner. An additional advantage of using MS-PLs in the set up is that they can withstand the higher power of the Raman pump laser, avoiding the problem of handling high power beams in free space. In this experiment, we compare forward, backward, and bi-directional Raman pumping schemes. In the

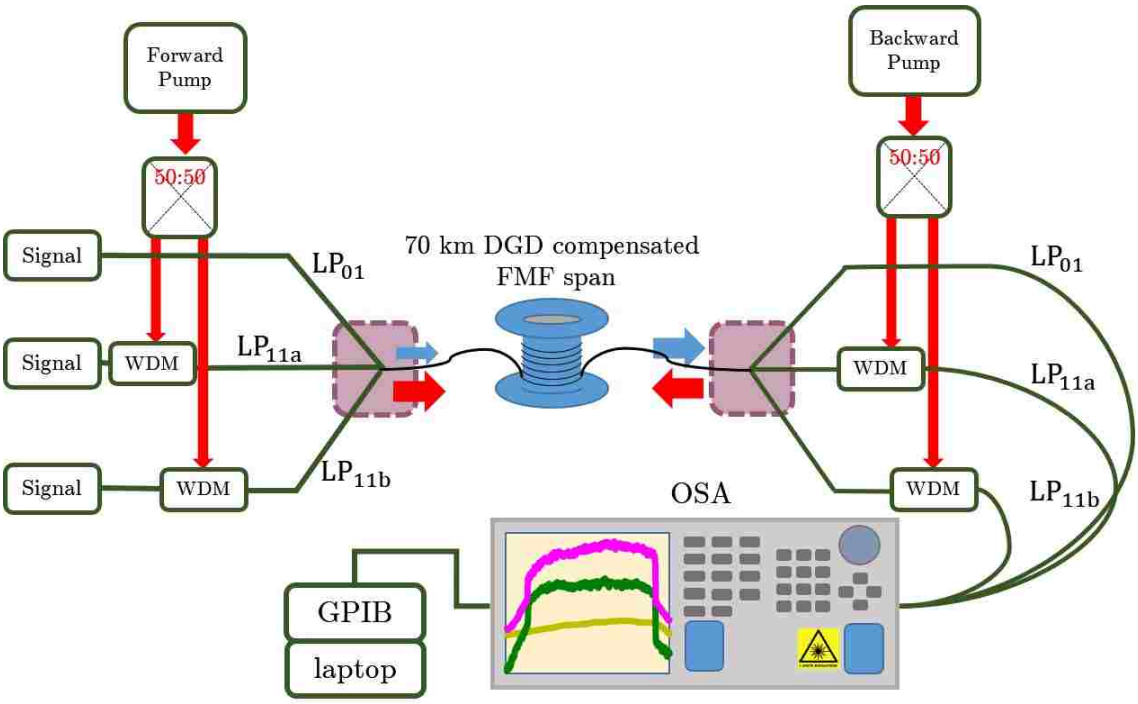

Figure 4.5: Experimental setup for Raman amplification in a FMF with three spatial modes using two MS-PLs as mode- multiplexer and de-multiplexer. The dashed boxes show where the MS-PLs are spliced to the fiber spool. The blue and red arrows represent the Signal and the pumps direction in the fiber.

forward and backward pump configurations, the total pump power is coupled in one direction and for the bi-directional pump configuration, the pump powers are adjusted to produce near optimum performance as described in [71] 30% of the total pump power is coupled in the forward and 70% is coupled in the backward direction. The total pump power is 2 W for all three configurations of the pumps, resulting in almost the same gain in all three cases, with a maximum of 22 dB gain for signal in the LP_{01} mode and 20 dB gain for signal in either one of the LP_{11} modes. There is a 2 dB DMDG in the fiber as measured.

4.3 Experimental Results

The Raman gain of the 70 km FMF span is measured with broadband light covering the C-band as the test signal. The broadband signal is generated by amplified

spontaneous emission (ASE) of an EDFA and its spectrum is flattened by a Waveshaper (WS) between 1545 nm and 1566 nm as shown in Fig. 4.6. The signal is coupled into each mode successively and the output of the corresponding mode captured on an OSA. The resulting on-off gain, $G_{\text{on-off}}$, defined in Eq. 1.45 is plotted in Figs. 4.7(d), 4.7(e), and 4.7(f) for all three modes, and all three pump configurations. As described in [13] and [46], the gain in all three modes is expected to be the same if the pumps are coupled into the LP_{11} modes, but the measurements reported in Figs. 4.7(d), 4.7(e), and 4.7(f) show ∼1.5-2 dB higher gain for LP_{01} mode than for the LP_{11} modes. In a FMF with negligible linear mode coupling and assuming the small signal approximation, the signal power in a particular mode i will grow exponentially with pump power. As shown in Eq. 1.47 for the $G_{\text{on-off}}$, the signal gain depends on the overlap integral of the three modes of the FMF. Therefore, to understand the origin of this mode dependent gain, we look at the overlap integrals of the fiber and calculate the fraction of the pump power that needs to be coupled in the LP_{01} mode to generate the ∼1.5-2 dB observed higher gain. The f_{ij} is calculated for a graded-index FMF with 3 spatial modes as in this experiment assuming a fixed wavelength of 1550 nm for both the signal and the pump transverse electric fields. This is because the exact refractive index profile as a function of wavelength was not available and also the shape of the transverse modes is expected to change only weakly in the wavelength range from 1455 to 1560 nm. The results are shown in Tab. 2.2 [5]. The inverse of the intensity overlap integral $1/f_{ii}$ corresponds to the effective area A_i^{eff} of the ith mode. For the degenerate LP_{11} mode, we use the complex notation $LP_{11\pm}$. This notation results in a ring shaped intensity profile that is very closely matched to the intensity profiles of the real vector modes TE_{01} and TM_{01} but also of the degenerate HE_{21} modes if the appropriate linear combination is used. In the situation where all modes composing the LP_{11} mode are excited with the same amount of power and assuming decorrelation between all modes caused either by modal dispersion or fiber imperfections, the resulting intensity profiles will be ring shaped and unpolarized, and therefore provide uniform gain to both LP_{01} and LP_{11} modes. A formal and more rigorous treatment can be found in [12]. The assumption that all modes composing the LP_{11} mode group are decorrelated is expected to be practically fulfilled in distributed Raman amplification, where amplification occurs over multiple-kilometer-long distances.

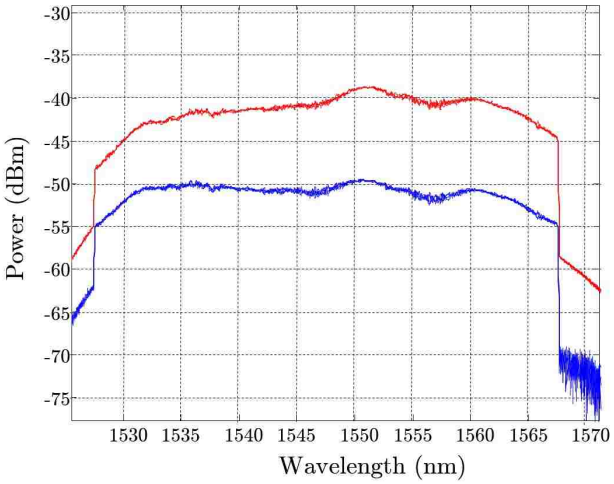

Figure 4.6: Broadband signal that is the ASE of an EDFA and flattened by a WS in the LP_{01} mode after the fiber with (Red) and without (Blue) Raman pumping in LP_{11} mode.

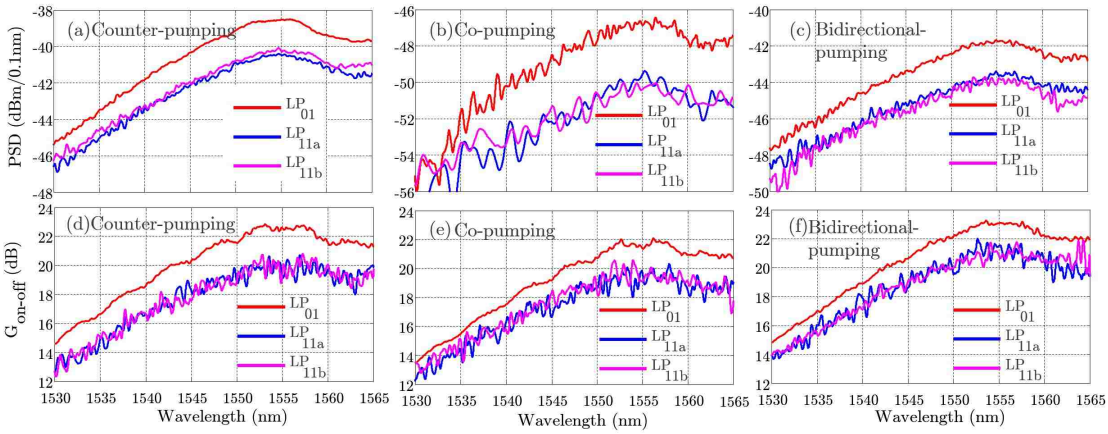

Figure 4.7: Raman ASE, power spectral density (PSD), and Raman gain ($G_{\text{on-off}}$) measurement as function of the wavelength and plotted for each spatial mode, reported for (a) and (d) counter-pumping, (b) and (e) co-pumping, and (c) and (f) bi-directional pumping configurations.

The signal power in every mode is observed to grow exponentially. Although the high power Raman pump is fully coupled into the LP_{11} modes initially, a fraction of this power eventually leaks into the LP_{01} mode due to coupling between the LP_{01} and LP_{11} modes after 70-km long fiber and the crosstalk of the MS-PLs spliced at both ends of the fiber spool. This fraction can be calculated from the data in Tab. 2.2:

$$\begin{aligned}\text{Gain}^{11}_{\text{on-off}} &= \text{Gain}^{01}_{\text{on-off}}\left(\frac{Pf_{21}+(1-P)f_{22}}{Pf_{11}+(1-P)f_{12}}\right)\\ &= 22\text{ dB}\times\left(\frac{0.10\times 0.8319+0.90\times 0.8354}{0.10\times 1.677+0.90\times 0.8319}\right)=20\text{ dB},\end{aligned}$$

where P is the fraction of pump power in LP_{01} mode and f_{ij} are shown in Tab. 2.2. There are signal waves in both LP_{01} and LP_{11} modes. When the signal gain in the LP_{11} modes reaches a value of 20 dB and the signal gain of the LP_{01} mode reaches a value of 22 dB, 10% of the pump power is found coupled into LP_{01} mode, resulting in the ∼1.5-2 dB higher LP_{01} signal gain. The 10% of the pump that appears in the LP_{01} mode is the result of a 10.8 dB crosstalk due to the mode coupling present in the FMF as well as the splice between the MS-PL multiplexer and the FMF. The total measured crosstalk including the 70-km FMF and the MS-PL is 9.8 dB, which is consistent with the observed gain difference between LP_{01} and LP_{11} modes. Figures 4.7(a), 4.7(b), and 4.7(c) show the measured amplified spontaneous emission (ASE) in each mode for the above-mentioned configurations. For the counter- and the bi-directional pump configuration, the difference in ASE follows the gain measurement, resulting in around 2 dB higher ASE for the LP_{01} mode compared to the LP_{11} modes. In the co-pumping configuration, the ASE for the LP_{01} mode is 3 dB higher than for the LP_{11} modes, which is approximately 1 dB larger than the corresponding modal gain difference.

As mentioned above, homogeneous amplification within the LP_{11} mode group is expected when all modes of the mode group are excited with the same power. In our experiment, this is clearly fulfilled by using an unpolarized pump, split in two non path-length matched paths and subsequently coupled into both LP_{11} ports of the mode multiplexer. This is because we inject four uncorrelated pumps (two from polarization and two uncorrelated by path-length difference). In order to check the

importance of exciting all modes of the group, we measured the Raman gain for the worst case scenario where only one polarized pump is co-propagating with a polarized signal injected into exactly the same LP_{11} mode. We modified our setup accordingly by connecting the polarized pump to a polarization controller that was then connected to the WDM combiner attached to one of the LP_{11} mode ports of the MS-PL, therefore bypassing the 50:50 coupler used in the previous experiments. Subsequently, the co-propagating signal power consisting of a polarized laser line at 1556 nm wavelength, was monitored for different polarization states of the pump for a pump power of 1 W. The maximum gain was measured to be 9 dB with a maximum variation in power of 1 dB. This represents a 11% variation in exponential gain which is a small but non-negligible effect. Note that the use of an unpolarized pump or the use of the 50:50 coupler to excite both LP_{11} ports can easily suppress the effect.

4.4 Conclusion

In conclusion, a net Raman gain exceeding transparency has been demonstrated in a few-mode fiber for all spatial modes using three different pump configurations. The maximum gain variation between modes is found to be <2 dB for a maximum gain of 22 dB, caused by crosstalk in the fiber span. A transmission experiment including the Raman pumped FMF is performed and explained more in Appendix A.

Chapter 5

Conclusion and Outlook

In this final chapter, we state the conclusion of the study presented in this dissertation as well as the outlook and future work that can further this investigation. The measurements that are presented in this work contribute detailed information on the IM-FWM effect and the distributed Raman amplification in FMFs and MMFs. For the first time, we have fully characterized the IM-FWM and SRS effects in a FMF with three spatial modes. We have shown that the IM-FWM in FMFs and MMFs can happen at any wavelength range and one does not need to be only around the zero dispersion wavelength to satisfy phase-matching condition like in SMFs. In Chapter 3, the phase-matching condition for the non-degenerate IM-FWM is studied theoretically and the efficiency of the IM-FWM effect is calculated correspondingly. On the other hand, the efficiency of the IM-FWM effect is measured for probe and pump detuning and the results are discussed. It is shown also that the IM-FWM is a polarization dependent effect and therefore the efficiency of the FWM effect is related to the relative polarization of the pumps and the probe. The effect of the polarization on IM-FWM is studied experimentally and the results are discussed. In Chapter 4, the distributed Raman amplification is experimentally characterized in a FMF with three spatial modes but a relatively longer length (70 km) than the fiber used in the FWM experiment (4.7 km). The two fibers have the same properties including the number of the modes, their refractive index and modes effective areas, A_{eff}. We have demonstrated equal gain for the distributed Raman amplification in the 70-km FMF with three spatial modes. The Raman pumps are solely coupled into the higher order mode, LP_{11} mode group, to ensure the equal gain in all modes

because the on-off Raman gain is related to the pump power and the overlap integral of the modes that the pump and signal are coupled into. The circumstances in which all modes in the FMF under study will be amplified by the same gain are discussed in detail in Chapter 4 and it is shown that if the pumps in this case are fully coupled into the higher order mode, the signals in all the modes are amplified by the same gain. The small differential mode-dependent gain of 1.5-2 dB is also explained by 10% pump that eventually ends up in the LP_{11} mode after 70 km fiber.

It is clear that much additional work on FMFs, MMFs, and MCFs is required to fully characterize the nonlinear effects in these fibers that are candidates for SDM. Measuring the efficiency bandwidth for the *multiple-mode pumps configuration* will help fully characterize the IM-FWM in the FMF and understand the differences between pump and probe detuning. A very detailed polarization study of the IM-FWM in a FMF can be performed using the MS-PLs in the FWM experiment instead of the free-space setup where the exact polarization state of all the waves in all the modes can be determined easily by a Polarization State Analyzer. This will help fully understand and characterize the polarization related fluctuations in the FWM efficiency presented in Chapter 3. Also, studying the equalized gain in Raman amplification of a MMF with more than 3 spatial modes will help expand and discuss the ways to achieve equal gain in all the modes in different fibers with different number of the modes and different refractive indices because the Raman gain is directly related to the overlap integral of the modes which is determined by the index profile of the fiber. On the other hand, the nonlinear effects can be studied in the pulsed lasers in these fibers where an autocorrelation setup as well as a FROG setup can be used to determine the pulse propagation. The FROG and autocorrelation systems are commercially available and they can also be setup in the laboratory. In MCFs using the pulsed laser will ensure enough power in all the cores specially if the MCF has strongly coupled cores.

Appendix A

Transmission Experiment with Raman Gain

The transmission performance of the Raman-pumped FMF span discussed in Chapter 4 is investigated by transmitting a signal to study the transmission for distances exceeding 1000 km by circulating the light through a single 70-km-long FMF span. The setup for the transmission experiment is shown in Fig. A.1. The signal is made by twenty distributed feedback lasers spaced 100 GHz apart and covering a wavelength range from 1546.92 nm to 1562.23 nm in the C-band. The signal is then sent through a $LiNbO_3$ MZM driven to generate a 33.33 GHz sinusoidal tone. The signal that now is a broadband signal including 60 wavelengths, 33.33 GHz apart from each other, is then polarization multiplexed. It is first sent though a 50:50 splitter and the splitted signals are recombined as orthogonal polarizations by a PBS. We adjusted the Raman pump powers to obtain a total gain of 16 dB, with 6 dB supplied by the forward pump and 10 dB by the backward pump, providing near optimum transmission performance according to [71]. Note that the Raman amplified fiber span is now optically transparent. Other amplifiers (EDFAs) in addition to the Raman amplifier are used as the loop amplifiers which are only used to overcome the loss due to the loop components.

The impulse response of the recirculating loop and the broadband signal is also investigated [72]. The impulse response is the transmission of the signal through the fiber in different modes resulting in 36 different measurements related to 6 different modes of the fiber similar to the transmission matrix measurement presented in

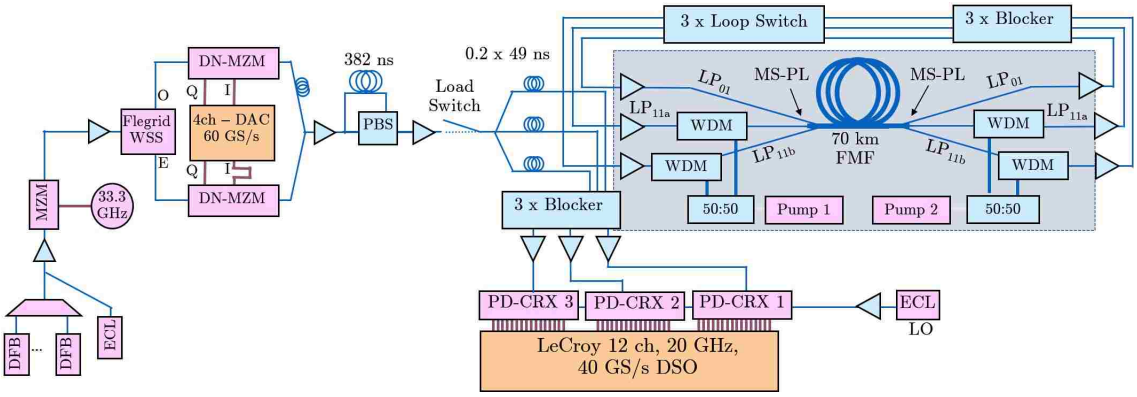

Figure A.1: Schematic setup for mode-multiplexed transmission experiment over 70-km bidirectionally pumped Raman-amplified few-mode fiber. The arrangement of the Raman pumps is highlighted by the dashed box [3].

Chapter 2. The impulse response shown in Fig. A.2 for transmission distances of 210, 350, 700, and 1400 km is obtained by averaging over the intensities of all 36 individual impulse responses. A strong ∼5 nsec central peak with a surrounding ∼5 ns plateau is clearly visible at the center of the impulse response for the 70-km distance. The peak gradually disappears for longer distances and the impulse response becomes more bell shaped. Based on the cascaded impulse response in Fig. A.2, good performance is expected up to 1400 km and all the transmitted data should thus be successfully recovered.

The transmission performance is further assessed by the quality factor known as Q-factor as a function of the input power reported in Fig. A.3(b). Q-factor is a measure of the bit error rate (BER) and represents the quality of the eye diagram. It is the ratio of the difference in mean values of the signal levels (0 and 1) in the eye diagram and the sum of the noise levels. The larger the difference in the signal level mean values are, the larger the Q-factor, therefor the lower the noise overlap and better BER will be. For this experiment, the optimum launch power per wavelength and spatial channel was found to be -7 dBm, and the Q-factors for all 60 WDM channels at optimum launch power are reported in Fig. A.3(a) for distances of 1050 km and 1400 km. A $Q > 7$ dB is observed for all the WDM channels for a distance up to 1050 km and all the transmitted data should thus be successfully recovered if forward-error correction (FEC) is applied. In conclusion, the performance of the Raman amplified few-mode fiber span studied in Chapter 4 has been

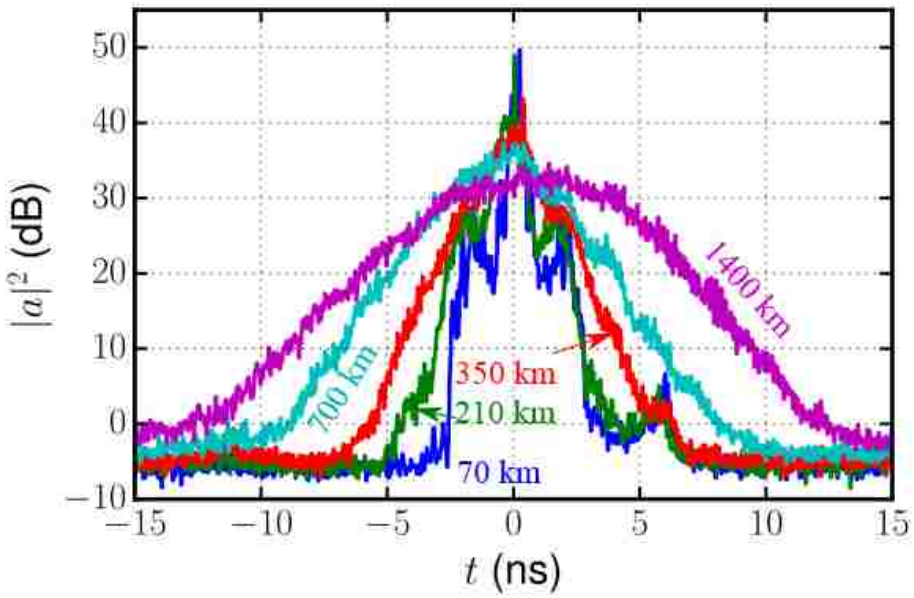

Figure A.2: Average-intensity impulse response ($|a|^2$) of a 70-km DGD compensated FMF span, after 70, 210, 350, 700, and 1400 km, respectively.

confirmed by a combined wavelength-division / space-division multiplexed transmission experiment in a recirculating loop, where a transmission distance of 1050 km has been achieved for a polarization-division multiplexed signal. The experiments demonstrate a single-wavelength channel capacity of 300 Gbit/s, a spectral efficiency of 9 bit/s/Hz for a transmission distance of 1050 km. This is the first reported transmission experiment that uses bidirectionally pumped distributed Raman amplification in a FMF and a spectral-efficiency-distance product of 9450 bit/s/Hz-km, which is the second largest demonstrated in FMFs to date.

Acknowledgements

This work was partly supported by the IT R&D program of MSIP/IITP, Korea, (10043383, Research of mode-division-multiplexing optical transmission technology over 10 km multi-mode fiber).

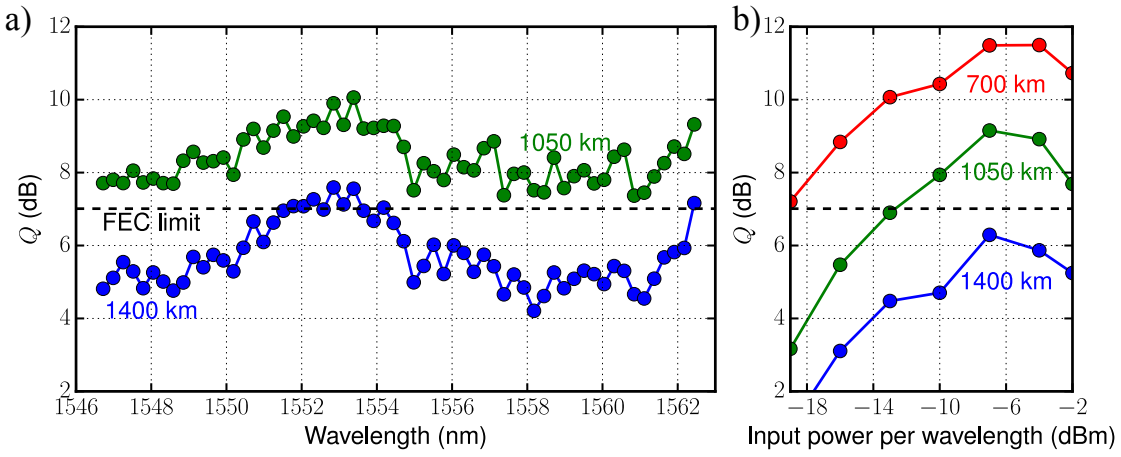

Figure A.3: Q-factor as function of the (a) wavelengths for all the 60 different channels and (b) input power per wavelength.

Bibliography

[1] Pollock, C. R. & Lipson, M. *Integrated photonics*, vol. 20 (Springer, 2003).

[2] Fontaine, N. *et al.* Characterization of space-division multiplexing systems using a swept-wavelength interferometer. In *Optical Fiber Communication Conference and Exposition and the National Fiber Optic Engineers Conference (OFC/NFOEC), 2013*, 1–3 (2013).

[3] Ryf, R. *et al.* Distributed Raman amplification based transmissionover 1050-km few-mode fiber. Tu.3.2.3 (2015).

[4] Okamoto, K. *Fundamentals of optical waveguides* (Academic press, 2010).

[5] Essiambre, R.-J. *et al.* Experimental observation of inter-modal cross-phase modulation in few-mode fibers. *Photonics Technology Letters, IEEE* **25**, 535–538 (2013).

[6] Essiambre, R.-J. & Tkach, R. Capacity trends and limits of optical communication networks. *Proceedings of the IEEE* **100**, 1035–1055 (2012).

[7] Tomkos, I., Miyamoto, Y., Wellbrock, G. & Winzer, P. Guest editorial: Spatially and spectrally flexible elastic optical networking. *Communications Magazine, IEEE* **53**, 20–22 (2015).

[8] Bromage, J. Raman amplification for fiber communications systems. *J. Lightwave Technol.* **22**, 79 (2004).

[9] Stolen, R. H., Lee, C. & Jain, R. K. Development of the stimulated Raman spectrum in single-mode silica fibers. *J. Opt. Soc. Am. B* **1**, 652–657 (1984).

[10] Polley, A. & Ralph, S. Raman amplification in multimode fiber. *Photonics Technology Letters, IEEE* **19**, 218–220 (2007).

[11] Chiang, K. S. Stimulated raman scattering in a multimode optical fiber: evolution of modes in stokes waves. *Opt. Lett.* **17**, 352–354 (1992).

[12] Antonelli, C., Mecozzi, A. & Shtaif, M. Raman amplification in multimode fibers with random mode coupling. *Opt. Lett.* **38**, 1188–1190 (2013).

[13] Ryf, R., Essiambre, R.-J., von Hoyningen-Huene, J. & Winzer, P. Analysis of mode-dependent gain in Raman amplified few-mode fiber. In *Optical Fiber Communication Conference*, OW1D.2 (Optical Society of America, 2012).

[14] Ryf, R. *et al.* Mode-equalized distributed Raman amplification in 137-km few-mode fiber. In *37th European Conference and Exposition on Optical Communications*, Th.13.K.5 (Optical Society of America, 2011).

[15] Maeda, M. *et al.* The effect of four-wave mixing in fibers on optical frequency-division multiplexed systems. *Lightwave Technology, Journal of* **8**, 1402–1408 (1990).

[16] Stolen, R. H. Nonlinearity in fiber transmission. *Proceedings of the IEEE* **68**, 1232–1236 (1980).

[17] Stolen, R. H. Phase-matched-stimulated four-photon mixing in silica-fiber waveguides. *Quantum Electronics, IEEE Journal of* **11**, 100–103 (1975).

[18] Cappellini, G. & Trillo, S. Third-order three-wave mixing in single-mode fibers: exact solutions and spatial instability effects. *J. Opt. Soc. Am. B* **8**, 824–838 (1991).

[19] Stolen, R. H., Bjorkholm, J. E. & Ashkin, A. Phase-matched three wave mixing in silica fiber optical waveguides. *Applied Physics Letters* **24**, 308–310 (1974).

[20] Coen, S. *et al.* Supercontinuum generation by stimulated raman scattering and parametric four-wave mixing in photonic crystal fibers. *J. Opt. Soc. Am. B* **19**, 753–764 (2002).

[21] Akimov, D. A. *et al.* Efficient anti-stokes generation through phase-matched four-wave mixing in higher-order modes of a microstructure fiber. *Opt. Lett.* **28**, 1948–1950 (2003).

[22] Wadsworth, W. *et al.* Supercontinuum and four-wave mixing with Q-switched pulses in endlessly single-mode photonic crystal fibres. *Opt. Express* **12**, 299–309 (2004).

[23] Dupriez, P. *et al.* Efficient white light generation in secondary cores of holey fibers. *Opt. Express* **15**, 3729–3736 (2007).

[24] Demas, J. *et al.* Intermodal nonlinear mixing with bessel beams in optical fiber. *Optica* **2**, 14–17 (2015).

[25] Poletti, F. & Horak, P. Dynamics of femtosecond supercontinuum generation in multimode fibers. *Opt. Express* **17**, 6134–6147 (2009).

[26] Essiambre, R.-J. *et al.* Experimental investigation of inter-modal four-wave mixing in few-mode fibers. *Photonics Technology Letters, IEEE* **25**, 539 – 542 (2013).

[27] Mac Suibhne, N., Ellis, A., Gunning, F. & Sygletos, S. Experimental verification of four wave mixing efficiency characteristics in a few mode fibre. In *Optical Communication (ECOC 2013), 39th European Conference and Exhibition on*, 1–3 (2013).

[28] Xiao, Y. *et al.* Theory of intermodal four-wave mixing with random linear mode coupling in few-mode fibers. *Opt. Express* **22**, 32039–32059 (2014).

[29] Keiser, G. *Optical fiber communications* (Wiley Online Library, 2003).

[30] Gloge, D. Weakly guiding fibers. *Applied Optics* **10**, 2252–2258 (1971).

[31] Snyder, A. W. Asymptotic expressions for eigenfunctions and eigenvalues of a dielectric or optical waveguide. *Microwave Theory and Techniques, IEEE Transactions on* **17**, 1130–1138 (1969).

[32] Ghatak, A. & Thyagarajan, K. *An introduction to fiber optics* (Cambridge university press, 1998).

[33] Agrawal, G. P. *Nonlinear fiber optics* (Springer, 2000).

[34] Black, R. & Gagnon, L. *Optical waveguide modes: polarization, coupling, and symmetry* (McGraw-Hill, 2010).

[35] Hellwarth, R. Third-order optical susceptibilities of liquids and solids. *Progress in Quantum Electronics* **5**, 1 – 68 (1977).

[36] Inoue, K. Four-wave mixing in an optical fiber in the zero-dispersion wavelength region. *Lightwave Technology, Journal of* **10**, 1553 –1561 (1992).

[37] Hill, K. O., Johnson, D. C., Kawasaki, B. S. & MacDonald, R. I. cw three wave mixing in single mode optical fibers. *Journal of Applied Physics* **49**, 5098–5106 (1978).

[38] Shibata, N., Braun, R. & Waarts, R. Phase-mismatch dependence of efficiency of wave generation through four-wave mixing in a single-mode optical fiber. *Quantum Electronics, IEEE Journal of* **23**, 1205 – 1210 (1987).

[39] Stolen, R. H., Lee, C. & Jain, R. K. Development of the stimulated Raman spectrum in single-mode silica fibers. *J. Opt. Soc. Am. B* **1**, 652–657 (1984).

[40] Stolen, R. H. & Lin, C. Self-phase-modulation in silica optical fibers. *Phys. Rev. A* **17**, 1448–1453 (1978).

[41] Stolen, R. H. & Bjorkholm, J. E. Parametric amplification and frequency conversion in optical fibers. *Quantum Electronics, IEEE Journal of* **18**, 1062–1072 (1982).

[42] Agrawal, G. *Nonlinear Fiber Optics* (Academic Press, 2012).

[43] Toulouse, J. Optical nonlinearities in fibers: review, recent examples, and systems applications. *Journal of Lightwave Technology* **23**, 3625–3641 (2005).

[44] Headley, C. & Agrawal, G. P. Unified description of ultrafast stimulated raman scattering in optical fibers. *JOSA B* **13**, 2170–2177 (1996).

[45] Headley, C. & Agrawal, G. *Raman amplification in fiber optical communication systems* (Academic Press, 2005).

[46] Antonelli, C., Mecozzi, A. & Shtaif, M. Modeling Raman amplification in multimode and multicore fibers. In *Optical Fiber Communication Conference*, W3E.1 (Optical Society of America, 2014).

[47] Polley, A. & Ralph, S. E. Raman amplification in multi-mode fiber: Reduction of inter-symbol interference via mode selective gain. *Optical Amplifiers and Their Applications/Coherent Optical Technologies and Applications* OWC2 (2006).

[48] Essiambre, R.-J. *et al.* Experimental investigation of inter-modal four-wave mixing in few-mode fibers. *Photonics Technology Letters, IEEE* **25**, 539–542 (2013).

[49] Essiambre, R.-J., Tkach, R. W. & Ryf, R. Fiber nonlinearity and capacity: Single-mode and multimode fibers. In Kaminow, I., Li, T. & E.Willner, A. (eds.) *Optical Fiber Telecommunications VI B*, chap. 1, 1 – 37 (Academic Press, 2013).

[50] Mumtaz, S., Essiambre, R. & Agrawal, G. Nonlinear propagation in multimode and multicore fibers: Generalization of the manakov equations. *Journal of Lightwave Technology* **31**, 398–406 (2013).

[51] Shemirani, M. B., Mao, W., Panicker, R. A. & Kahn, J. Principal modes in graded-index multimode fiber in presence of spatial- and polarization-mode coupling. *J. Lightwave Technol.* **27**, 1248–1261 (2009).

[52] Brüning, R., Zhang, Y., McLaren, M., Duparré, M. & Forbes, A. Overlap relation between free-space laguerre gaussian modes and step-index fiber modes. *J. Opt. Soc. Am. A* **32**, 1678–1682 (2015).

[53] Ryf, R. *et al.* Mode-division multiplexing over 96 km of few-mode fiber using coherent 6 × 6 mimo processing. *J. Lightwave Technol.* **30**, 521–531 (2012).

[54] Gifford, D. K., Soller, B. J., Wolfe, M. S. & Froggatt, M. E. Optical vector network analyzer for single-scan measurements of loss, group delay, and polarization mode dispersion. *Appl. Opt.* **44**, 7282–7286 (2005).

[55] VanWiggeren, G., Motamedi, A. & Barley, D. Single-scan interferometric component analyzer. *Photonics Technology Letters, IEEE* **15**, 263–265 (2003).

[56] Aso, O., Tadakuma, M. & Namiki, S. Four-wave mixing in optical fibers and its applications. *dEp* **1**, 2 (1999).

[57] Poletti, F. & Horak, P. Description of ultrashort pulse propagation in multimode optical fibers. *J. Opt. Soc. Am. B* **25**, 1645–1654 (2008).

[58] Mecozzi, A., Antonelli, C. & Shtaif, M. Nonlinear propagation in multi-mode fibers in the strong coupling regime. *Opt. Express* **20**, 11673–11678 (2012).

[59] Esmaeelpour, M., Essiambre, R.-J., Fontaine, N. K., Ryf, R. & Toulouse, J. Measurements of frequency instabilities and slow random evolution of intermodal four-wave mixing in few-mode fibers. In *41st European Conference and Exposition on Optical Communications*, WE.2.4.5 (Optical Society of America, 2015).

[60] Ryf, R. *et al.* Distributed Raman amplification based transmission over 1050-km few-mode fiber. In *41st European Conference and Exposition on Optical Communications*, Tu.3.2.3 (Optical Society of America, 2015).

[61] Esmaeelpour, M. *et al.* Transmission over 1050-km few-mode fiber based on bidirectional distributed raman amplification. *J. Lightwave Technol.* **34**, 1864–1871 (2016).

[62] Raman, C. V. & Krishnan, K. S. A new type of secondary radiation. *Nature* **121**, 501–502 (1928).

[63] Hellwarth, R. W. Theory of stimulated raman scattering. *Phys. Rev.* **130**, 1850–1852 (1963).

[64] Stolen, R. H., Gordon, J. P., Tomlinson, W. J. & Haus, H. A. Raman response function of silica-core fibers. *J. Opt. Soc. Am. B* **6**, 1159–1166 (1989).

[65] Stolen, R. & Ippen, E. Raman gain in glass optical waveguides. *Applied Physics Letters* **22**, 276–278 (1973).

[66] Stolen, R. H., Ippen, E. & Tynes, A. Raman oscillation in glass optical waveguide. *Applied Physics Letters* **20**, 62–64 (1972).

[67] Stolen, R. H. Polarization effects in fiber raman and brillouin lasers. *IEEE Journal of Quantum Electronics* **15**, 1157–1160 (1979).

[68] Fontaine, N. K. *et al.* Mode-selective dissimilar fiber photonic-lantern spatial multiplexers for few-mode fiber. In *Proceedings of European Conference on Optical Communication* (2013).

[69] Huang, B. *et al.* All-fiber mode-group-selective photonic lantern using graded-index multimode fibers. *Opt. Express* **23**, 224–234 (2015).

[70] Leon-Saval, S. G. *et al.* Mode-selective photonic lanterns for space-division multiplexing. *Opt. Express* **22**, 1036–1044 (2014).

[71] Essiambre, R., Winzer, P., Bromage, J. & Kim, C. H. Design of bidirectionally pumped fiber amplifiers generating double rayleigh backscattering. *Photonics Technology Letters, IEEE* **14**, 914–916 (2002).

[72] Ryf, R. *et al.* Space-division multiplexed transmission over 4200-km 3-core microstructured fiber. In *Optical Fiber Communication Conference and Exposition (OFC/NFOEC), 2012 and the National Fiber Optic Engineers Conference*, 1 –3 (2012).

Vita

Mina Esmaeelpour was born in Tabriz, South Azerbaijan, Iran. In 2007, she graduated with the degree of Bachelor of Science and in 2010 with the degree of Master of Science in Physics from the University of Tabriz. She she started her further education in 2010 at Lehigh University in Bethlehem, PA, USA. During her PhD, she has also been an intern at Bell laboratories in Holmdel, NJ, in Summer 2011 and from Summer 2013 till 2015. At Lehigh, she founded the Lehigh University Student Chapter of the Optical Society of America (LUSCOSA) and the Lehigh University Optics and Photonics Society (LUOPS).

Journal Publications

- **M. Esmaeelpour**, R.-J. Essiambre, N. K. Fontaine, R. Ryf, J. Toulouse, Y. Sun, R. Lingle, "Power Fluctuations of Inter-Modal Four Wave Mixing in Few-Mode Fibers", submitted.

- **M. Esmaeelpour**, R. Ryf, N. K. Fontaine, H. Chen, A. H. Gnauk, R.-J. Essiambre, J. Toulouse, Y. Sun, R. Lingle, "Transmission over 1050-km Few-Mode Fiber based on a Bidirectional Distributed Raman Amplification", Journal of Lightwave Technology (2016).

- D. M. Marom, J. Dunayevsky, D. Sinefeld, M. Blau, R. Ryf, N. K. Fontaine, M. Montoliu, S. Randel, C. Liu, B. Ercan, **M. Esmaeelpour**, S. Chandrasekhar, A. H. Gnauck, S. G. Leon-Saval, J. Bland-Hawthorn, J. R. Salazar-Gil, Y. Sun, L. Grner-Nielsen, R. Lingle, "Wavelength-selective switch with direct few mode fiber integration", Optics Express (2015).

- R. Ryf, N. K. Fontaine, H. Chen, B. Guan, B. Huang, **M. Esmaeelpour**, A. H. Gnauck, S. Randel, S. J. B. Yoo, A. M. J. Koonen, R. Shubochkin, Y. Sun, R. Lingle, "Mode-multiplexed transmission over conventional graded-index multimode fibers", Optics Express (2015).

- R. Ryf, S. Randel, A. H. Gnauck, C. Bolle, A. Sierra, S. Mumtaz, **M. Esmaeelpour**, E. C. Burrows, R.–J. Essiambre, P. J. Winzer, D. W. Peckham, A. H. McCurdy, R. Lingle, "Mode-Division Multiplexing Over 96-km of Few-Mode Fiber Using Coherent 6 x 6 MIMO Processing", Journal of Lightwave Technology (2012).

Conference Presentations

- **M. Esmaeelpour**, R.–J. Essiambre, N. K. Fontaine, R. Ryf, and J. Toulouse, "Measurements of Frequency Instabilities and Slow Random Evolution of Inter-Modal Four-Wave Mixing in Few-Mode Fibers", European Conference on Optical Communication (2015).

- R. Ryf, **M. Esmaeelpour**, N. K. Fontaine, H. Chen, A. H. Gnauck, R.–J. Essiambre, J. Toulouse, Y. Sun, and R. Lingle, Jr., "Distributed Raman Amplification based Transmission over 1050 km Few-Mode Fiber", European Conference on Optical Communication (2015).

- R. Ryf, N. K. Fontaine, B. Guan, B. Huang, **M. Esmaeelpour**, S. Randel, A. H. Gnauck, S. Chandrasekhar, A. Adamiecki, G. Raybon, R. W. Tkach, R. Shubochkin, Y. Sun, R. Lingle, "305-km combined wavelength and mode-multiplexed transmission over conventional graded-index multimode fibre", European Conference on Optical Communication (2014).

- R. Ryf, N. K. Fontaine, J. Dunayevsky, D. Sinefeld, M. Blau, M. Montoliu, S. Randel, Chang Liu, B. Ercan, **M. Esmaeelpour**, S. Chandrasekhar, A. H. Gnauck, S. Leon-Saval, J. Bland-Hawthorn, J. Salazar-Gil, Y. Sun, L. Grner-Nielsen, R. Lingle, D. Marom, "Wavelength-Selective Switch for Few-Mode Fiber Transmission", European Conference on Optical Communication (2013).

- R. Ryf, A. Sierra, R.–J. Essiambre, S. Randel, A. Gnauck, C. A. Bolle, **M. Esmaeelpour**, P. J. Winzer, R. Delbue, P. Pupalaikis, A. Sureka, D. Peckham, A. McCurdy, R. Lingle, "Mode-Equalized Distributed Raman Amplification in 137-km Few-Mode Fiber", European Conference on Optical Communications (2011).

- R. Ryf, A. Sierra, R.–J. Essiambre, A. H. Gnauck, S. Randel, **M. Esmaeelpour**, S. Mumtaz, P. J. Winzer, R. Delbue, P. Pupalaikis, A. Sureka, T. Hayashi, T. Taru, T. Sasaki, "Coherent 1200-km 6x6 MIMO mode-multiplexed transmission over 3-core microstructured fiber", European Conference on Optical Communication (2011).